# Best
# Available
# Copy

AD-780 191

FAILURE ANALYSIS OF MICROFLAWED
DUCTILE MATRIX MATERIALS

Ronald E. Frishmuth

Illinois University

Prepared for:

Advanced Research Projects Agency

April 1974

T.&A.M. REPORT NO. 364

UILU-ENG 74-600

# FAILURE ANALYSIS OF MICROFLAWED
# DUCTILE MATRIX MATERIALS

by

Ronald E. Fritzmuth

The views and conclusions contained in this document are
those of the authors and should not be interpreted as neces-
sarily representing the official policies, either expressed
or implied of the Advanced Research Projects Agency or
the U.S. Government.

DEPARTMENT OF THEORETICAL AND APPLIED MECHANICS
UNIVERSITY OF ILLINOIS
URBANA, ILLINOIS

T. & A. M. Report No. 384

# FAILURE ANALYSIS OF MICROFLAWED DUCTILE MATRIX MATERIALS

by

Ronald E. Frishmuth

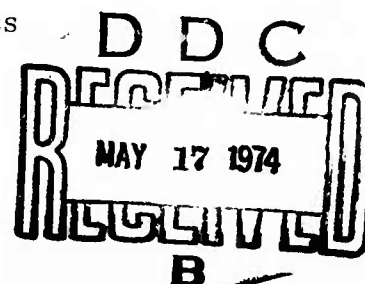Department of Theoretical and Applied Mechanics
University of Illinois
Urbana, Illinois
April, 1974

DDC
RECEIVED
MAY 17 1974
RECEIVED
B

# FOREWORD

Recent requirements for increased strength and service life of machines and structures have been met by the use of higher strength materials and new fabrication and joining methods. Simultaneously, failures due to fracture have increased relative to those resulting from excessive deformation. Frequently service conditions are such that low temperature brittle fracture, fatigue fracture, and high temperature creep rupture must be considered in a single system. National concern with increased safety, reliability, and cost has focused attention upon these problems.

Methods are now available to predict both fatigue crack initiation life and crack propagation life. Paradoxically the materials properties required for long fatigue crack initiation life are incompatible with the requirements of high fracture toughness. Thus, the conflicting design approaches and requirements placed on the material are confusing and often impossible to satisfy.

Numerous publications dealing with a variety of fracture problems have led to many new and useful developments. However, the synthesis of the concepts into methods for design, testing and inspection has lagged.

This program of study is intended to contribute to the integration, correlation, and organization of mechanics and materials concepts and research information into a form that will permit enlightened decisions to be made regarding fracture control. Reports are in preparation in three categories:

1. Research reports designed to explore, study and integrate isolated and/or conflicting concepts and methods dealing with life prediction,

2. Reports to introduce and summarize the state-of-the-art concepts and methods in particular areas, and

3. Example problems and solutions intended to illustrate the use of these concepts in decision making.

H. T. Corten
Principal Investigator

# ABSTRACT

It is shown in this study that linear elastic fracture mechanics techniques do not provide a consistent geometry-independent means of predicting failure in micro-flawed ductile matrix materials. Several aspects of microflawed material behavior during fracture testing suggest that considerable plastic behavior occurs on the micro-scale in microflawed materials. It is suggested that limit analysis techniques applied first on the microscale then extended to the macroscale may provide a consistent means of failure prediction.

Three-dimensional limit surfaces are developed for several types of micro-flawed materials. Comparison of these limit criteria with currently available the-ories and experimental data on microflawed materials in the absence of macroscale notches shows that the proposed theory is valid for smooth material failure predictions.

Subsequent extension of the microscale limit surfaces to continuum macroscale structural analysis shows that the proposed theory will provide an upper bound failure prediction. It is also shown that linear elastic fracture mechanics methods will pro-vide a lower bound failure prediction.

## ACKNOWLEDGMENT

iv

## TABLE OF CONTENTS

## LIST OF TABLES

## LIST OF FIGURES

## LIST OF SYMBOLS

| | |
|---|---|
| a | Crack length |
| $A_m$ | Area of an RVE face minus the projected area of all flaws within an RVE onto the RVE face |
| $A_{Tot}$ | Area of an RVE which is unity |
| B | Depth of a notched beam at the notch |
| C | Remaining ligament length of a macroscale notched bar |
| D | Diameter |
| D' | Diameter at the notch in a notched circular specimen |
| $\dot{c}$ | Strain rate |
| $\dot{\epsilon}_1,\ \dot{\epsilon}_2,\ \dot{\epsilon}_3$ | Principal strain rates |
| i, j | Standard index notation with a range of three |
| K | Stress intensity factor |
| $K_c$ | Critical stress intensity |
| $K_{Ic}$ | Plane strain fracture toughness |
| $K_Q$ | Conditional $K_{Ic}$ |
| $\ell$ | Length of longest slit in RVE model of cast iron |
| M | Moment |
| P | Load |
| $P_Q$ | Secant corrected load from P-v record |
| $P_1,\ P_2,\ P_3$ | Loads in the principal RVE axis directions |
| $P_{LB}$ | Lower bound limit load |
| $P_{UB}$ | Upper bound limit load |
| r | Radius of spherical microflaw |
| r' | Radial distance from crack tip |
| $r_y$ | Plastic zone correction factor |

| | |
|---|---|
| R | Ratio of tensile to compression stresses in a microflawed material |
| S | Span length in a bend test |
| t | Thickness |
| $\dot{u}, \dot{v}, \dot{w}$ | Displacement rates in the x, y, z directions respectively on the RVE faces |
| v | Crack mouth opening displacement |
| $V_m$ | Volume of matrix material in a representative volume element |
| W | Width |
| x, y, z | Coordinate axes |
| $\sigma_x, \sigma_y, \sigma_z$ | Stresses in the x, y, and z directions |
| $\sigma_g$ | Gross stress applied to a notched part |
| $\sigma_c$ | Critical gross stress |
| $\sigma_{Comp}$ | Compressive failure stress |
| $\sigma_1, \sigma_2, \sigma_3$ | Principal stresses within an RVE |
| $\bar{\sigma}_1, \bar{\sigma}_2, \bar{\sigma}_3$ | Principal stresses averaged over the face of an RVE |
| $\sigma_{my}$ | Yield strength of matrix material in a composite structure |
| $\sigma_{oc}$ | Tensile limit stress of a microflawed material |
| $\delta_C$ | Maximum displacement at a specified point |
| $\delta$ | Additional crack length necessary to have macroscale limit analysis match experimental data |
| $\Delta$ | Deflection of a beam at the centerline |
| $\alpha$ | Geometry factor |
| $\nu$ | Poisson's ratio |
| $\theta$ | Angle measured from the plane of a crack |

# 1. INTRODUCTION

In the past, engineering design utilizing microflawed materials, of which cast iron is a prime example, has been based on elastic strength of materials concepts. This amounts to neglecting all ductility and plastic behavior of the material and usually results in an overdesigned structure. This standard design procedure for these materials has come about because of the different properties of microflawed materials in tension and compression and because of an inability to accurately predict the bending behavior of these materials.

Typically, microflawed materials have different moduli of elasticity in tension and compression. This leads to a noncentroidal neutral axis and non-linear stress distributions in bending situations (1)*. This fact manifests itself when extreme fiber failure stresses from bending tests, calculated using elastic formulas, are compared with elastically calculated failure stresses from tensile tests. Typically, the elastically calculated bending failure stress is 30 to 50 percent higher than the tensile failure stress. In this study "failure" is defined as the inability to support load without unlimited deformation or fracture. Failure load or stress is defined as the maximum load or stress which can be supported by a part without unlimited deformation or fracture.

The increased load carrying capacity of microflawed materials in bending situations is usually neglected in design. Standard procedure is to simply use the tensile yield strength as the limiting extreme fiber stress in bending. This conservative approach is taken in design because of an inability to accurately predict bending failure stresses.

---

*Numbers in parenthesis refer to list of references.

The problem of failure load or failure stress prediction in microflawed materials is compounded if macroscale holes or notches are present. This problem has not been satisfactorily approached and prediction of failure stress or load in microflawed materials under various loading conditions when macroscale notches are present is the subject of this study. For purposes of the following discussion, a microflawed material is defined as a material which has flaws, either holes or inclusions, with the smallest dimension not smaller than 10 microns. This definition excludes such microscale discontinuities as dislocations but includes graphite particles in cast iron and porosity in cast metals. Further, discussion will be limited to those microflawed materials which have a ductile matrix capable of plastic deformation. This rules out materials such as ceramics in which plastic behavior is negligible or non-existent.

Over the past 10 to 15 years, the theoretical tool known as linear elastic fracture mechanics (LEFM) has become a highly developed and utilized method for predicting failure loads in materials which behave in a brittle fashion when a notch or crack is present. The plane strain fracture toughness, $K_{Ic}$ is the major parameter used to characterize fracture in this method. $K_{Ic}$ is thought to be geometry independent. Hence, if $K_{Ic}$ is known, LEFM techniques can, in principle, be used to predict failure loads of a notched part with any shape macroscale notch under any loading condition. This tool seems to be ideally suited to the current problem and is the obvious method to apply. Several investigators (2, 3, 4, 5, 6) have attempted to use this method in studying failure of cast irons and cast steels. The combined results of these studies are somewhat inconsistent as will be discussed in Chapter 2. In an effort to clear up some of these inconsistencies, an investigation using various geometries of fracture toughness specimens made of gray cast iron was undertaken. The conclusion of this LEFM investigation in gray cast iron was disappointing in that accurate failure stress in bending situations could not be predicted from information

obtained in tensile tests and vice versa. At this point, two choices were available. Either a modification of existing linear elastic fracture mechanics could be developed or a different theoretical tool could be applied. During the fracture toughness testing of the current study, considerable plasticity on the microscale was noticed. Because of this, the latter tack was taken and the theory of plastic limit analysis was applied to the problem.

The theory of limit analysis was first developed for a continuum by Drucker, Prager, and Greenberg (7). Subsequently, various investigators applied this technique to such things as plates with holes (8, 9, 10), soil failure (11, 12), reinforced concrete beams (13), and fibrous composite materials (14, 15). In this latter work on composite materials McLaughlin and Batterman (14, 15) first developed limit criteria for small, representative elements of larger structures. Since these limit conditions were set up for representative elements, they can, under certain circumstances, be used in continuum structural analysis. The conditions under which the representative element limit conditions can be used on the continuum structure depend on the constraints imposed on the structure and the size of the representative element when compared with the total structure (16).

In the current work, this concept of developing limit criteria for representative volume elements (RVE's) on the microscale and then extending these criteria to macroscale structures will be employed. Chapter 3 includes a development of the various limit conditions for two types of RVE's as well as a comparison of the proposed limit criteria with other failure criteria and with data available in the literature on smooth specimen tests. In Chapter 4, these RVE limit criteria will be used in macroscale limit analysis of bars in tension and beams in bending.

The theoretical results of this study are valid for any microflawed material which has a microscale structure similar to the RVE's to be studied and having a

ductile matrix. However, since a good example of these types of materials are the cast irons, the comparisons of experimental and theoretical results discussed herein will be for cast irons. The proposed theory adequately predicts the failure stress for smooth bar situations under various loading conditions. Further, the microscale limit surface can be extended to the macroscale in order to provide a failure prediction technique for several of the notched specimens used in the current study. It will be shown that the result of this macroscale extension of microscale limit criteria to cases involving macroscale notches is to provide an upper bound to failure load prediction. On the other hand, it will be shown that the linear elastic fracture mechanics method provides a lower bound to actual failure loads.

## 2. LINEAR ELASTIC FRACTURE MECHANICS APPLIED TO A TYPICAL MICROFLAWED MATERIAL

### 2.1 Introduction

In this chapter, currently available literature, in which linear elastic fracture mechanics techniques have been utilized in analysis of typical microflawed material failure, will be reviewed. The materials studied in this literature have been gray and nodular cast iron. Also to be presented in this chapter are linear elastic fracture mechanics data from a gray cast iron study which was undertaken for this current work. It will be shown that linear elastic fracture mechanics parameters cannot be used in predicting failure of a notched microflawed material.

In the interest of brevity and clarity, discussion of the meaning of the fracture mechanics terminology and details of fracture mechanics testing have been put into Appendix A and B respectively, rather than in the body of Chapter 2. Hence, in what follows it will be assumed that the reader is familiar with the contents of Appendix A and B.

### 2.2 Literature on Linear Elastic Fracture Mechanics Applied to Typical Microflawed Materials

In 1969, Glover and Pollard (3) presented data in which the plane strain fracture toughness, $K_{Ic}$ of a gray cast iron approximating the specifications of the American Society for Testing and Materials (ASTM) for Class 30 cast iron were reported. The reported $K_{Ic}$ for as-cast material with normal flake size and 100% pearlite matrix was 17.5 ksi $\sqrt{in.}$ as measured in a four point bend test. In the work from which the Glover and Pollard publication was derived, Glover (2) showed that the "apparent $K_{Ic}$" did not vary with specimen thickness down to 0.0984 inches. The Glover (2) and Glover and Pollard (3) "apparent $K_{Ic}$" is taken to mean the conditional $K_{Ic}$ or $K_Q$ obtained from experimental load-displacement P-v records (Appendix B). $K_Q$ is

equal to $K_{Ic}$ only if the P-v record meets certain criteria on linearity. These criteria are set up to operationally define the load at 2% crack extension.

Brandt (4) conducted an investigation which included the determination of plane strain fracture toughness values for ductile iron, gray iron and .25% cast steel. Table 1 lists Brandt's results for ductile and gray cast iron. Brandt first tested notched three point bend bars at -50°F which were 5 inches deep, 20.5 inches long and 2.5 inches thick. At this temperature, Brandt found that the P-v records of all three materials studied were non-linear and the ASTM criteria for valid $K_{Ic}$ testing could not be met. Several tests were then conducted at -320°F where more linear P-v records were observed and the ASTM criteria were valid. Brandt concluded that the materials tested had a good deal more toughness than would be expected from strict application of the ASTM size criteria for valid $K_{lc}$ testing (see Appendix B).

Lazaridis, et al. (5, 6) conducted an investigation on several types of ductile cast iron. For purposes of comparison of fracture resistance of the various types of iron, the fracture toughness of single edge notch tension specimens (3/4 inch thick) was used. One of the ductile irons studied is approximately equal in yield strength, tensile strength and elongation to the ductile iron tested by Brandt (4). Table 2 lists the results of Lazaridis et al. for this ductile iron at -40°F. The average value is higher than Brandt's $K_Q$ listed in Table 1 for three point bend tests at -50°F. However, at -50°F, Brandt found three point bend tests were not valid whereas Lazaridis et al. obtained valid tests at -40°F on single edge notch specimens.

Thus, tests at approximately the same temperature but for different geometries give conflicting results in terms of $K_Q$ and validity criterion. It is also interesting to note that if the thickness for valid toughness testing (Appendix B) is applied to these tests, then Brandt's tests on 2.5 inch thick bars should be valid whereas the tests of Lazaridis et al. on 3/4 inch thick plates should not have been valid. Further, in both

cases, the secant corrected loads, $P_Q$ used operationally to define crack extension and hence $K_Q$, are considerably below the final fracture load. Thus, if $K_{Ic}$ can be found, LEFM techniques could still not be used to predict failure since only the load for crack extension would be defined.

It appears from the sketchy data available, that $K_{Ic}$ may not be geometry independent in cast iron. Further, the non-linear behavior of cast iron may mean that $K_{Ic}$ can be used to predict crack advance but it may not be useful in predicting failure loads for notched parts. In order to investigate these points further, an investigation using fracture toughness specimens of different geometries was undertaken.

## 2.3 Current Investigation of Linear Elastic Fracture Mechanics Techniques Applied to Gray Cast Iron

In the current study, several geometries of fracture toughness specimens were utilized. The material used was ASTM Class 60 pearlitic matrix gray cast iron with type A-1 graphite. Figure 1 is a typical engineering stress-strain record for the material in tension and compression (17). Table 3 lists the chemical composition of the material. The fracture toughness specimens were taken from portions of a twelve foot diameter cylinder with a 3.22 inch wall thickness. Table 4 lists the variation in proportional limit stress, .2% yield stress and ultimate stress at the inner third, middle third and outer third of the 3.22 inch thickness.

A series of three point bend (3PB) fracture toughness specimens were tested at various temperatures in both the fatigue precracked and not fatigue precracked condition. The specimen dimensions are shown in Fig. 2. The curvature shown in the figure is exaggerated and comes about due to the six foot radius of the cast cylinder. This curvature will not alter the test results since it is small in the actual specimen. The maximum load $P_{max}$, was recorded for each test and the stress intensity based on $P_{max}$, called $K_{max}$ values were calculated. Table 5 lists the results of the test for all cases. In these tests, as with the others in this study, the stress intensity

equations were obtained from Ref. 18. No appreciable difference was noticed in the $K_{max}$ values between the machined notch and the machined notch plus fatigue crack cases with approximately the same crack length. For this reason, all further testing was conducted on machined notched specimens only. The three point bend tests also revealed that the maximum load and $K_{max}$ did not change significantly with increased temperature up to 400°F. Therefore, all further testing was conducted at room temperature.

Several tests were conducted on a compact (CT) specimen geometry with dimensions as shown in Fig. 3A. These specimens were cut from segments of the cylinder as shown in Fig. 3B. The maximum load and corresponding $K_{max}$ values for these tests are shown in Table 6. Three additional compact specimens were tested and the load versus crack mouth displacement records were taken. These records are shown in Fig. 4 along with a table showing the secant corrected load, $P_Q$, the maximum load, $P_{max}$, the $K_Q$ value and a comment on whether or not the ASTM criteria for P-v records has been met.

Circumferential notched tensile (CNT) specimens and double edge crack (DEC) specimens were also tested in the current study. Figure 5 and 6 show the geometries tested. Table 7 lists the pertinent specimen dimensions, fracture load and $K_{max}$ values for the circumferential notch tension test. Table 8 lists the same information for the double edge crack plate specimens.

In terms of $K_{max}$ values, the circumferential notch tensile data from three different size specimens have much lower toughness than the three point bend data. Table 9 summarizes pertinent test data for the four specimen geometries tested. As the component of load attributable to bending decreases from the three point bend to the compact tension to the double edge crack plate and finally to the circumferential notch tension, the maximum load and $K_{max}$ are continually decreasing. Further, it is seen from Table 9 that the valid secant corrected data from the compact specimens agree with the $K_{max}$ values from the two types of notched tension tests.

Several pertinent observations were made during the current study. First, catastrophic failure did not occur suddenly in the three point bend or compact specimen testing. Instead, the cracks extended gradually below maximum load and as the load was increased, the cracks grew. There was no "big bang" characteristic of fracture toughness testing except in the direct tension tests. Also, microscopic observations at the crack tip in the compact testing revealed plastic action at the tips of graphite flakes. This was evidenced by dimpling of the matrix areas ahead of the flakes. Another investigator has noticed this (19) and Fig. 7 is a photograph of this effect. Finally, application of the ASTM criteria on required thickness of fracture toughness specimens indicated that all tests should have been valid. Using $K_{Ic}$ = 18.8 from the valid CT test and a yield stress for the middle of the casting of 45 ksi a thickness of 0.435 inches is required for valid tests. Since all specimens were tested in 1 inch thickness, they all should have yielded valid $K_{Ic}$.

## 2.4 Conclusions of Linear Elastic Fracture Mechanics Testing and Microflawed Materials

Two things are apparent from the available literature and the current testing program. First, all information indicates that standard ASTM procedures do not provide satisfactory results when used in fracture toughness testing in cast irons. Secondly and more importantly, it is not possible, using LEFM techniques, to obtain geometry independent parameters with which to characterize failure in cast irons. This can be demonstrated by a simple example. In the current study, the $K_{Ic}$ from the compact tests is 18.8 ksi$\sqrt{in}$. This value can be used as the critical stress intensity in an analysis of a three point bend test. As an example, the specimen dimensions of 3PB-1 listed in Table 5 and the stress intensity solution for this geometry given in Ref. 18 will be used. Solution of the stress intensity equation for the load P gives $P_{max}$ = 7.55 kips. Comparison of this calculated maximum load from the tensile fracture toughness with the actual fracture load of the specimen, which is 18.8 kips from Table 5, shows a considerable discrepancy.

One reason that linear elastic fracture mechanics does not yield a good prediction of failure in bending is due to the different elastic moduli in tension versus compression in microflawed materials. The formulas of linear elastic fracture mechanics for bending situations have been derived assuming a material with equal moduli in tension and compression. This is evidenced by the use of the elastic bending formula, $\sigma = Mc/I$ in the various bending stress intensity derivations. In a microflawed material such as cast iron, the modulus of elasticity in tension and compression are not equal as shown in Fig. 1. This means the neutral axis of a beam is not at the centroid. Further, Draffin and Collins (20) have shown that the neutral axis shifts during loading. Thus, even if the technology of linear elastic fracture mechanics could be modified to account for the off-center neutral axis, some method of accounting for shifting of the neutral axis would have to be developed if the failure load is to be predicted accurately.

This shifting of the neutral axis in microflawed materials is most likely why $P_{max}$ and $K_{max}$ values of the current study show a decrease from three point bend to compact to direct tension. As the component of load due to bending decreases, the amount of material subject to compression decreased, the neutral axis location becomes less important, and the fracture load decreases because of the lower strength of the material in tension versus compression.

Two alternatives are apparent for the accurate failure prediction of microflawed materials with macroscale notches. First, the concepts of linear elastic fracture mechanics can be modified to account for the neutral axis shifting. Some of the currently available non-linear fracture mechanics techniques such as the J-integral or R-curve methods could be useful in this regard. However, these techniques have been developed with the aim of determining fracture toughness on specimens smaller than required according to ASTM criteria. Indications from the literature and current study indicate that the bend specimens tested more than met the size requirements

of ASTM. Further, even if a $J_{Ic}$ and hence a $K_{Ic}$ could be determined from the P-v record of a bend test, failure loads could still not be predicted. The same problem of using $K_{Ic}$ to predict results, discussed earlier, also arises here: namely, $K_{Ic}$ can predict crack extension but not failure.

The other alternative, and the tack to be taken in the remainder of this work, is to investigate the apparent microscale plasticity in cast iron failures and attempt to employ plasticity theory on the microscale. Two important factors indicate that considerable plastic behavior is exhibited in the matrix material of cast irons. The first is the fact that considerable non-linearity is noted in both stress-strain records of tensile tests and P-v records from fracture toughness tests. The other factor is that microscale plastic action has been observed at the tips of graphite flakes in both the current investigation and others. For these reasons then, it appears that a study of plasticity as applied to microflawed ductile matrix materials may lead to a useful technique for failure prediction.

## 3. FAILURE SURFACES FOR MICROFLAWED MATERIALS BY LIMIT ANALYSIS TECHNIQUES

### 3.1 Introduction

Because of microplastic action between flaws which has been observed in micro-flawed materials, it is hypothesized that failure of such materials does not occur until the plastic limit load of small elements of material is reached. Therefore, limit analysis of representative volume elements will be performed, and the resulting limit loads, expressed as a surface in principal stress space, will be in effect equivalent to a continuum failure surface for the material.

The steps to be followed in the subsequent analysis are illustrated in Fig. 8. The first step is to develop a model consistent with the real material. This model must be representative of the real material and macroscale structures must be made up by stacking the representative elements in various arrangements. The model will be called the representative volume element or RVE. If a failure or limit surface can be developed for the RVE, this surface, with certain restrictions, will be a valid limit criterion for use in the limit analysis of any notched or unnotched macroscale structure. It is the purpose of this chapter to propose and develop a failure theory for microflawed materials based on limit analysis applied on the microscale. Later, these microscale limit conditions will be applied to the macroscale. The reasons for using this approach are to reflect observed microscale plasticity and provide a theory which would involve few material dependent properties and would be based on micro-scale features such as flaw size and spacing.

The theory of limit analysis was first developed for a continuum by Drucker, Prager and Greenburg (7). The two major theorems of limit analysis were concisely stated by Drucker (21) as follows:

<u>Lower Bound Theorem</u> The body will not collapse, or will be just at the point of collapse, if an equilibrium distribution of stress can be found which balances the applied load and is everywhere below yield or at yield.

<u>Upper Bound Theorem</u> The body will collapse if there is any compatible pattern of plastic deformation for which the rate at which the external forces do work equals or exceeds the rate of internal dissipation.

The major points of these theorems are:

1. The statically admissible stress field of the lower bound need not be the actual one in the structure.

2. The kinematically admissible velocity field of the upper bound need not be related to the actual velocity field in the structure.

3. There is no required relation between the stress field of the lower bound and the velocity field of the upper bound.

These limit theorems have been used by many investigators to obtain failure load prediction in such things as plates with holes (8, 9, 10), soils (11, 12), and recently, composite materials (14, 15). It is proposed here that some of the techniques used in these analyses be used in obtaining failure load predictions for micro-flawed materials.

McLaughlin and Batterman (14) and McLaughlin (15), have used limit analysis of representative microscale elements of two dimensional structures to obtain limit loads for macroscale structures. The materials these investigators studied were fibrous composites. Majumdar and McLaughlin (16) have shown that under certain conditions, limit criteria obtained for general three-dimensional microscale elements, called representative volume elements (RVE), could be used as limit criteria for continuum analysis of macroscale structures.

The requirements necessary for extension of microscale limit criteria to macroscale limit analysis as set up by Majumdar and McLaughlin (16) are twofold. First, the microscale element analyzed must be small compared to the larger structure. Secondly, the constraints and type of loading on the large structure must be such that no constraints on displacement or stress distributions are placed on the RVE's in critical areas of the structure. For the RVE's and notched structures to be considered in this work, both conditions are met and the micro to macroscale extensions of RVE limit surfaces are valid.

Limit conditions for two types of RVE will now be developed; one type is a model of a microflawed material containing spherical voids while the other is a model of a material containing multi-directional slits. This latter case is an attempt to model cast iron. In all cases, the matrix material is assumed to be highly ductile and follow the von Mises criterion with equal limit strengths, $\sigma_{my}$ in tension and compression. All RVE's are three dimensional cubes.

The analyses to follow are for periodic arrays of the RVE. Hence, strictly speaking, the materials studied should be anisotropic in normal stress space. However, it will be assumed that the equations developed are valid for statistically isotropic materials with a random distribution of flaws under principal stress. Therefore, throughout the remainder of this work normal and principal stress on the RVE will be used interchangeably. Further, stress states which are other than principal stresses can be obtained from the equations developed here by using the standard transformation procedures.

One important aspect of the application of limit analysis techniques in studying the problem at hand must be pointed out at the outset. This is that limit analysis was originally derived assuming an elastic-perfectly plastic material behavior with unlimited ductility. McLaughlin (22) has recently shown that the techniques of limit analysis

are still valid in work hardening situations but the requirements of unlimited ductility still remains. In some of the cases to be studied here, this requirement may not permit the strict application of limit analysis. In cases where unlimited ductility does not exist, McLaughlin (22) has shown that the application of limit analysis still provides an upper bound to the failure load. These facts will be utilized in Chapter 4.

### 3.2 Limit Analysis Applied to RVE of Structure with a Periodic Array of Holes

Figure 9 is a sketch of the RVE model for the case of a periodic or macroscopically homogeneous array of holes. The RVE is simply a cube with side dimensions of unity and 1/8 spheres at all eight corners. The spheres are merely holes; hence, they have no yield surface and zero strength in tension and compression. This model would be useful for a highly porous metal such as bad casting or certain portions of a sintered powder product.

The lower bound analysis of the hole case is straightforward. Assume that structural members extend through the structure from one face to its opposite face in all three directions as shown in Fig. 10. For the assumed normal stress field, there are seven limit conditions. In those parts of the structure where uniaxial stresses only occur, these conditions are

$$\sigma_1 = \sigma_{my} \tag{1}$$

$$\sigma_2 = \sigma_{my} \tag{2}$$

$$\sigma_3 = \sigma_{my} \tag{3}$$

where the subscripts 1, 2, and 3 indicate the principal stresses in the x, y, and z directions of the cube. For those parts of the assumed structure where biaxial stresses occur, the limit conditions are

$$(\sigma_1^2 - \sigma_1 \sigma_2 + \sigma_2^2)^{1/2} = \sigma_{my} \tag{4}$$

$$(\sigma_2{}^2 - \sigma_2 \sigma_3 + \sigma_3{}^2)^{1/2} = \sigma_{my} \tag{5}$$

and

$$(\sigma_3{}^2 - \sigma_3 \sigma_1 + \sigma_1{}^2)^{1/2} = \sigma_{my} \tag{6}$$

Finally, in those areas where all three stresses occur, the limit condition is

$$\left\{ \frac{1}{2} \left[ (\sigma_1 - \sigma_2)^2 + (\sigma_2 - \sigma_3)^2 + (\sigma_3 - \sigma_1)^2 \right] \right\}^{1/2} = \sigma_{my} \tag{7}$$

The limit conditions in Eqs. 1-7 are in terms of actual stress on the microscale. In order to get the equations in terms of average macroscale RVE stresses, it is noted that

$$\sigma_1 = \frac{P_1}{A_m}; \quad \sigma_2 = \frac{P_2}{A_m}; \quad \sigma_3 = \frac{P_3}{A_m} \tag{8}$$

where $P_1$, $P_2$, and $P_3$ are the loads in the 1, 2, and 3 directions. $A_m$ is the area of an RVE face, which is unity, minus the projected area of all flaws within or on the RVE. The average stresses are defined as

$$\bar{\sigma}_1 = \frac{P_1}{A_{Tot}}; \quad \bar{\sigma}_2 = \frac{P_2}{A_{Tot}}; \quad \bar{\sigma}_3 = \frac{P_3}{A_{Tot}} \tag{9}$$

where the bar indicates average over the RVE face and $A_{Tot}$ is the total surface area of one RVE face. The $P_1$ and $P_2$ values are equal in both cases so that

$$\bar{\sigma}_i A_{Tot} = \sigma_i A_m \tag{10}$$

or

$$\bar{\sigma}_i = \frac{A_m}{A_{Tot}} \sigma_i \tag{11}$$

$A_{Tot}$ is simply 1 since a unit cube has been considered for the model.

The seven limit conditions for the lower bound can now be rewritten in terms of average stresses on the RVE as

$$\bar{\sigma}_1 = A_m \, \sigma_{my}$$

$$\bar{\sigma}_2 = A_m \, \sigma_{my} \qquad \text{(12a)}$$

$$\bar{\sigma}_3 = A_m \, \sigma_{my}$$

$$(\bar{\sigma}_1{}^2 - \bar{\sigma}_1 \, \bar{\sigma}_2 + \bar{\sigma}_2{}^2) = (A_m \, \sigma_{my})^2$$

$$(\bar{\sigma}_2{}^2 - \bar{\sigma}_2 \, \bar{\sigma}_3 + \bar{\sigma}_3{}^2) = (A_m \, \sigma_{my})^2 \qquad \text{(12b)}$$

$$(\bar{\sigma}_3{}^2 - \bar{\sigma}_3 \, \bar{\sigma}_1 + \bar{\sigma}_1{}^2) = (A_m \, \sigma_{my})^2$$

$$\frac{1}{2} \left[ (\bar{\sigma}_1 - \bar{\sigma}_2)^2 + (\bar{\sigma}_2 - \bar{\sigma}_3)^2 + (\bar{\sigma}_3 - \bar{\sigma}_1)^2 \right] = (A_m \, \sigma_{my})^2 \qquad \text{(12c)}$$

In loading the RVE from zero load under any combination of $\bar{\sigma}_1$, $\bar{\sigma}_2$, and $\bar{\sigma}_3$ stress, whichever limit condition is reached first will govern the lower limit load failure. Thus, the lower bound three dimensional limit surface is shown in Fig. 11(a). Under a plane stress condition, with $\bar{\sigma}_3 = 0$, the plane stress limit condition for the lower bound appears as shown in Fig. 11(b).

In order to obtain an upper bound, a velocity field must be assumed for the deformation of the RVE, then the external work is set equal to the internal energy dissipated in performing the assumed deformation. For the case at hand, a homogeneous deformation of the matrix will be assumed. Hence, the internal energy dissipation is given by

$$\int_{V_m} \sigma_{ij} \, \dot{\epsilon}_{ij} \, dV_m \qquad \text{(13)}$$

where the subscripts i and j are the standard index notation with a range of three and double indices indicate summation according to the standard summation convention. $V_m$ is the volume of the matrix material only. It is noted that since the total RVE

volume is unity, $V_m$ is the volume fraction of matrix or one minus the volume fraction of voids. Since the model axes are principal axes and the displacement rates are linear functions of the strain rates, Eq. 13 becomes

$$V_m (\sigma_1 \dot{\epsilon}_1 + \sigma_2 \dot{\epsilon}_2 + \sigma_3 \dot{\epsilon}_3) \tag{14}$$

where $\sigma_1$, $\sigma_2$ and $\sigma_3$ are the stresses at the point on the matrix limit surface where the normal vector has components proportional to $\dot{\epsilon}_1$, $\dot{\epsilon}_2$ and $\dot{\epsilon}_3$ in the $\sigma_1$, $\sigma_2$ and $\sigma_3$ directions, respectively. Letting the displacement rates in each of the three principal directions of the RVE be $\dot{u}$, $\dot{v}$ and $\dot{w}$, the external work done is

$$\bar{\sigma}_1 \dot{u}\Big|_{x=\frac{1}{2}} +(-\bar{\sigma}_1 \dot{u})\Big|_{x=-\frac{1}{2}} + \bar{\sigma}_2 \dot{v}\Big|_{y=\frac{1}{2}} +(-\bar{\sigma}_2 \dot{v})\Big|_{y=-\frac{1}{2}} + \bar{\sigma}_3 \dot{w}\Big|_{z=\frac{1}{2}} +(-\bar{\sigma}_3 \dot{w})\Big|_{z=-\frac{1}{2}} \tag{15}$$

where the displacement rates are linear functions of the strain rates, that is

$$\left.\begin{aligned} \dot{u} &= x\, \dot{\epsilon}_1 \\ \dot{v} &= y\, \dot{\epsilon}_2 \\ \dot{w} &= z\, \dot{\epsilon}_3 \end{aligned}\right\} \tag{16}$$

Using Eq. 16 in Eq. 15 and evaluating the limits, the external work becomes

$$\bar{\sigma}_1 \dot{\epsilon}_1 + \bar{\sigma}_2 \dot{\epsilon}_2 + \bar{\sigma}_3 \dot{\epsilon}_3 \tag{17}$$

Setting the external work equal to the internal energy gives

$$\bar{\sigma}_1 \dot{\epsilon}_1 + \bar{\sigma}_2 \dot{\epsilon}_2 + \bar{\sigma}_3 \dot{\epsilon}_3 = V_m (\sigma_1 \dot{\epsilon}_1 + \sigma_2 \dot{\epsilon}_2 + \sigma_3 \dot{\epsilon}_3) \tag{18}$$

Since the $\dot{\epsilon}$ terms are completely arbitrary, the coefficients of the $\dot{\epsilon}$ terms can be set equal giving

$$\left.\begin{array}{l} \overline{\sigma}_1 = V_m \, \sigma_1 \\[2mm] \overline{\sigma}_2 = V_m \, \sigma_2 \\[2mm] \overline{\sigma}_3 = V_m \, \sigma_3 \end{array}\right\} \tag{19}$$

$\sigma_1$, $\sigma_2$ and $\sigma_3$ are combinations of stress which satisfy the von Mises limit condition. Hence, in terms of average stresses, the upper bound limit criteria for the RVE under the assumed deformation becomes

$$\frac{1}{2}\left[(\overline{\sigma}_1 - \overline{\sigma}_2)^2 + (\overline{\sigma}_2 - \overline{\sigma}_3)^2 + (\overline{\sigma}_3 - \overline{\sigma}_1)^2\right]^{1/2} = (V_m \, \sigma_{my})^2 \tag{20}$$

In $\overline{\sigma}_1$, $\overline{\sigma}_2$ and $\overline{\sigma}_3$ space, this is simply the von Mises cylinder.

It will be noted that the upper and lower bounds are considerably far apart in cases of triaxial tension or compression. The lower bound closes off in these octants and predicts failure under hydrostatic conditions whereas the upper bound is not closed off in these octants. In triaxial stress situations involving one principal stress which is of opposite sign to the other two, the lower and upper bound are concentric von Mises cylinders. The difference between these cylinders depends on the ratio of $V_m$ to $A_m$.

In order to close off the upper bound in triaxial tension or compression, a velocity field must be developed for the RVE which would allow deformation of opposite faces without requiring displacement of faces perpendicular to the ones displaced. This is necessary in order to obtain limit conditions giving flat plane cut off surfaces to the von Mises upper bound cylinder. This exercise was not carried out in this work, and further consideration of this RVE will be restricted to plane stress conditions.

In plane stress, Eq. 20 describes a von Mises ellipse. Comparison of the lower and upper bound surfaces in plane stress ($\overline{\sigma}_3 = 0$), Fig. 11(b) conditions shows that the ratio of lower to upper bounds in biaxial tension-compression regions is $V_m$ divided by $A_m$. Since the assumed model is for spherical holes,

$$\frac{V_m}{A_m} = \frac{1 - 4/3 \pi r^3}{1 - \pi r^2} \tag{21}$$

where r is the radius of the spherical hole. Hence, for small r, the $V_m/A_m$ ratio is close to unity and the bounds are close. Sphere radii between 0.0 and 0.25 give upper and lower bounds that are within 13%. The maximum radius that a sphere in the unit cell can have is 0.50.

For actual materials approximating the model used, upper and lower bounds can be determined by estimating the flaw size and spacing using a photomicrograph of the structure and hence determine the radius of the flaws to use in the RVE, the load carrying area, and the volume of matrix. As an example of this technique, assume that the structure of a hypothetical microflawed material is made up of randomly spaced, uniform size holes as shown in Fig. 12(a) (23). If a plane AB is passed randomly through this structure, the plane would appear as in Fig. 12(b). The principal values which must be determined to utilize the proposed analysis are the flaw radius and spacing. The chances that a given plane passed through the microstructure will cut any flaw at the equator are slim; nevertheless, the largest radius observed in the plane under study can be reasonably used as the flaw radius for the model. The center-to-center spacing of flaws in the three-dimensional structure can be determined from measurements on the random plane (23). This is accomplished by drawing random test lines on the plane and determining the number of particles intercepted per unit length of these test lines. The reciprocal of this value is the three-dimensional center-to-center spacing. For the purpose of illustration, suppose that in the hypothetical structure, the largest flaw on a plane has a radius of 0.005 inches and the center-to-center spacing has been measured as 0.050 inches. These values must now be proportioned to give the flaw size in a unit cube. The actual

center-to-center spacing is equivalent to the long diagonal of the RVE and the measured flaw radius is proportioned accordingly. The proportionality Eq. is

$$\frac{\text{(radius of RVE flaw)}}{\text{(radius of measured flaw)}} = \frac{\sqrt{3}}{\text{(measured center-to-center spacing)}} \qquad (22)$$

For the hypothetical case,

$$r, \text{ radius of RVE flaw} = \frac{\sqrt{3}}{.050}(.005)$$

or

$$r = 0.173 \qquad (23)$$

With $r$ now determined, $A_m$ and $V_m$ are easily calculated. The upper and lower bounds can be determined if the limit strength $\sigma_{my}$, of the plastic matrix is known.

There are, of course, idealizations in the above hypothetical example. In real materials, the flaws will not be of a uniform size. Instead, there will be a distribution of flaw sizes. Which statistical measure of this distribution should be used in the RVE analysis can only be determined from experiments. Several choices are the mean size, the average size or the largest size in the distribution. In any case, the plane section to be studied in a given material will appear as shown in Fig. 12(b). Further, the measurement of the representative center-to-center spacing used in the hypothetical example is valid regardless of whether or not the flaw size are uniform (23).

### 3.3   Limit Analysis Applied to RVE of a Structure with a Periodic Array of Slits

The analysis in this section is undertaken with the intent of modeling and predicting failure in cast iron materials. Before discussing the RVE model chosen for this case, it is best to discuss the solidification process which occurs in making cast iron. Figure 13 shows schematically and in somewhat simplified fashion the steps in solidification of gray cast iron (24). The first step is the formation of graphite nuclei throughout the molten metal. These nuclei then proceed to grow

arms in several directions. Next, the matrix metal between these growing arms will solidify. Eventually, the graphite arms from one nucleus approach arms from other nuclei and the matrix material between arms impinge on the matrix between arms of adjacent nuclei. The matrix and arms associated with one graphite nucleus constitute one eutectic cell. The above procedure takes place in three dimensions; hence, the eutectic cell is three-dimensional. In gray cast iron, the flakes are quite random in orientation and extend almost to the boundary of the eutectic cell. In nodular cast iron, the graphite flakes are condensed and form a spheroid in the eutectic cell.

For the purposes of analysis, the RVE chosen is an idealized eutectic cell of cast iron. The RVE is a cube of material of unit dimensions on all sides. Because the graphite flakes in cast iron are quite weak, the "flakes" in the RVE will be modeled as slits. These slits are straight and they all pass through the center of the RVE. The slits are oriented at various but undefined angles from the center of any face of the RVE as shown in Fig. 14. Figure 14 is a sketch of 1/8 of the RVE chosen to represent gray cast iron. All other segments of the RVE are symmetric as indicated by the dashed extension lines in the figure. The matrix material is assumed to be the von Mises type with tensile limit strength equal to $\sigma_{my}$. The slits are assumed to have some small but finite distance between the slit faces. Further, the faces of the slit will be assumed to be very rough. The small distance between slit faces and the rough surfaces of the slit mean that load or displacement will be completely transmitted across the slit if even a minute normal compressive load or displacement occurs across the slit. Likewise, if a zero or normal tensile component of load or displacement occurs across the slit, then no load or displacement can be transmitted across the slit. It should be noted that the sum total of all flakes in the RVE model of gray iron result in a square projection on any RVE face. For the nodular iron case, the spherical nodule has a circular projected area on any RVE face.

A simple lower bound for the RVE can be obtained in the same way that the lower bound was obtained for the hole model; that is, assume that straight structural members extend through the matrix from one face to its opposite face as indicated in Fig. 15(a). Consider a plane cut through the center of the RVE with two opposite faces subject to tensile stress as shown in Fig. 15(b). Because of the slits in the structure, the central portion of the RVE can not carry tensile load and all tensile load is carried by the matrix ligament at the side. Consideration of the total ligament area available to carry load perpendicular to any principal stress shows that the area available is just $A_m$ where $A_m$ is defined as the total RVE face area (unity) minus the projected area of all slits onto the RVE face. If the projected area of all slits onto an RVE face is a perfect square, then in triaxial tension there can be no uniaxial stressed regions in the structural members passed through the matrix. Hence, in triaxial tension there are three biaxial limit equations and one triaxial limit equation. These are the following:

$$\bar{\sigma}_1^2 - \bar{\sigma}_1 \bar{\sigma}_2 + \bar{\sigma}_2^2 = (A_m \sigma_{my})^2$$

$$\bar{\sigma}_2^2 - \bar{\sigma}_2 \bar{\sigma}_3 + \bar{\sigma}_3^2 = (A_m \sigma_{my})^2$$

$$\bar{\sigma}_3^2 - \bar{\sigma}_3 \bar{\sigma}_1 + \bar{\sigma}_1^2 = (A_m \sigma_{my})^2 \tag{24}$$

$$\frac{1}{2}\left[(\bar{\sigma}_1 - \bar{\sigma}_2)^2 + (\bar{\sigma}_2 - \bar{\sigma}_3)^2 + (\bar{\sigma}_3 - \bar{\sigma}_1)^2\right] = (A_m \sigma_{my})^2$$

The bar stresses indicate that the conversion from stresses in the structural members to stresses on the surface of the RVE, as discussed in the lower bound analysis of the hole model, has already been carried out here. In three-dimensional principal stress space, these equations give a triaxial tension limit surface with a shape as shown in Fig. 16.

In the case of a circular projection of slits onto an RVE face as in a nodular cast iron model, there will be uniaxial stressed areas in triaxial tension with the result that three additional lower bound equations arise and govern the triaxial limit surface. These equations are the following:

and

$$\left.\begin{array}{c} \overline{\sigma}_1 = A_m \, \sigma_{my} \\[2mm] \overline{\sigma}_2 = A_m \, \sigma_{my} \\[2mm] \overline{\sigma}_3 = A_m \, \sigma_{my} \end{array}\right\} \tag{25}$$

The resulting lower bound surface for triaxial tension in principal stress space is composed of three intersecting plane surfaces as shown in Fig. 17.

It is interesting to note that if the square projected shape of the gray cast iron model were slightly rounded at the corners, then uniaxial stressed regions would occur in triaxial tension and the resulting limit surface in principal stress space would be the same shape as the nodular iron surface, Fig. 17.

For the stress situation involving two positive and one negative principal stresses, the area of the RVE surface acted on by the positive stresses is still $A_m$ but the slits in the negative stress direction close and transmit load. Hence, the area available to carry load in the negative direction is the total RVE face area, $A_{Tot}$ or just unity.

The lower bound equations with $\overline{\sigma}_1$, $\overline{\sigma}_2$ assumed positive and $\overline{\sigma}_3$ assumed negative are

$$\left(\frac{\overline{\sigma}_2}{A_m}\right)^2 - \frac{\overline{\sigma}_2 \, \overline{\sigma}_3}{A_m} + \overline{\sigma}_3^{\,2} = \sigma_{my}^{\,2} \tag{26a}$$

$$\overline{\sigma}_3^{\,2} - \frac{\overline{\sigma}_3 \, \overline{\sigma}_1}{A_m} + \left(\frac{\overline{\sigma}_1}{A_m}\right)^2 = \sigma_{my}^{\,2} \tag{26b}$$

$$\frac{1}{2}\left[\left(\frac{\overline{\sigma}_1}{A_m} - \frac{\overline{\sigma}_2}{A_m}\right)^2 + \left(\frac{\overline{\sigma}_2}{A_m} - \overline{\sigma}_3\right)^2 + \left(\overline{\sigma}_3 - \frac{\overline{\sigma}_1}{A_m}\right)^2\right] = \sigma_{my}^2 \tag{26c}$$

In principal stress space with two tensile and one compressive stress, Eq. 26 appears as shown in Fig. 16 or 17.

In the case of two negative and one positive principal stresses, there are no uniaxially stressed regions in either the cube or sphere RVE. The slit oriented perpendicular to the tensile stress always opens; hence, no tensile load is transmitted through the slit area of the RVE and the area of the RVE surface carrying tensile load is $A_m$. The slits in planes parallel to the compressive stresses all transmit load; hence, the total RVE face area carries the compressive loads. For this case then, the lower bound equations become (assuming $\overline{\sigma}_1$ and $\overline{\sigma}_3$ to be the negative stresses),

$$\overline{\sigma}_1^2 - \overline{\sigma}_1 \frac{\overline{\sigma}_2}{A_m} + \left(\frac{\overline{\sigma}_2}{A_m}\right)^2 = \sigma_{my}^2 \tag{27}$$

$$\left(\frac{\overline{\sigma}_2}{A_m}\right)^2 - \frac{\overline{\sigma}_2 \, \overline{\sigma}_3}{A_m} + \overline{\sigma}_3^2 = \sigma_{my}^2 \tag{28}$$

$$\overline{\sigma}_3^2 - \overline{\sigma}_3 \, \overline{\sigma}_1 + \overline{\sigma}_1^2 = \sigma_{my}^2 \tag{29}$$

$$\frac{1}{2}\left[\left(\overline{\sigma}_1 - \frac{\overline{\sigma}_2}{A_m}\right)^2 + \left(\frac{\overline{\sigma}_2}{A_m} - \overline{\sigma}_3\right)^2 + (\overline{\sigma}_3 - \overline{\sigma}_1)^2\right] = \sigma_{my}^2 \tag{30}$$

However, consideration of the various stress regions in the assumed stress field shows that the combinations of $\overline{\sigma}_1$ and $\overline{\sigma}_2$ only and $\overline{\sigma}_2$ and $\overline{\sigma}_3$ only do not occur anywhere in the assumed structure regardless of the shape of the agglomeration of slits. Hence in both the gray iron and nodular iron models, the region of the limit surface in

which two stresses are negative and one is positive is governed by Eq. 30 for the lower bound. This equation is simply a von Mises ellipse with the center displaced from the original amount which depends on the magnitude of the stresses. This portion of the limit surface is shown in Figs. 16 and 17.

With respect to Eqs. 24 through 30, it should be noted that cyclic permutations of the indices on the stress terms give two additional sets of equations in each case. All equations thus produce the complete three-dimensional surfaces as shown in Figs. 16 and 17.

The remaining stress condition to be considered in the lower bound analysis is the case of triaxial compression. In triaxial compression, all slits in the structure close up and the area available to carry load in any of the three directions is the total area of the cube face or unity. Further, consideration of the stress state at any point in the RVE shows that all points are subject to triaxial compressive stress. Hence, the only lower bound equation in triaxial compression is

$$\frac{1}{2} \left[ (\bar{\sigma}_1 - \bar{\sigma}_2)^2 + (\bar{\sigma}_2 - \bar{\sigma}_3)^2 + (\bar{\sigma}_3 - \bar{\sigma}_1)^2 \right] = \sigma_{my}^2 \tag{31}$$

This equation is just the von Mises cylinder as shown in Figs. 16 and 17.

Equation 31 completes the lower bound analysis for the RVE chosen to represent gray and nodular cast irons. Consideration of the lower bound for the gray iron case, shown in Fig. 16, shows that there are concave regions on the surface. While it is true that Drucker (25) has shown that limit surfaces must not have concave regions, it is noted that Fig. 16 is not a true limit surface, but only a lower bound and hence may have concave regions.

Upper bounds for the proposed RVE models require that a velocity field be assumed as pointed out in (16), these velocity fields must be such that RVE faces remain compatible with one another. This restriction on any assumed velocity field is necessary because RVE's must be able to be stacked up to make a larger structure

without any gaps between them. If RVE faces were permitted to warp under deformation, gaps would occur between the warped face of one RVE and that of the next. This is not permissible in the total structure; hence, the restriction on the deformation of the RVE. For the gray iron model, one velocity field which satisfies the compatibility requirements is shown in Fig. 18(a). This velocity field is shown on a typical RVE cross-section cut parallel to the direction of an applied uniaxial displacement. The uniaxial displacement has been assumed in the 1 direction but the same velocity field is assumed for uniaxial displacement in 2 or 3 direction. Further, portions of adjacent RVE's are shown in order to indicate that compatibility requirements are met.

The velocity field assumed in one matrix ligament of one RVE is isolated in Fig. 18(b). Since the only dissipation in the assumed field occurs in the von Mises matrix, the dissipation rate is simply two times the yield in shear times the shear displacement rate times the sheared area or

$$2 \cdot \left( \frac{\sigma_{my}}{\sqrt{3}} \right) \cdot (\dot{u}\sqrt{2}) \cdot \left( \frac{\sqrt{2}}{2} \left( 1 - \frac{\ell}{\sqrt{2}} \right) t \right)$$

In this equation, t is the thickness in the plane of the paper and $\ell$ is the maximum length of a diagonal slit. For the assumed field, the external work is simply $2P_1 \dot{u}$. The subscript 1 on P indicates that the load and displacement occur in the 1 direction but results are the same for the 2 and 3 direction. Setting the external work equal to the internal dissipation gives the upper bound limit load in the 1 direction,

$$P_{UB_1} = \frac{\sigma_{my}}{\sqrt{3}} \left( 1 - \frac{\ell}{\sqrt{2}} \right) t \tag{32}$$

Figure 18(c) is a section of the RVE and the dashed line shows the length to be used for the thickness, t in Eq. 32. The total length of this line is

$$2 \left[ 1 + \frac{\ell}{\sqrt{2}} \right] \tag{33}$$

Substituting Eq. 33 into Eq. 32 for t gives

$$P_{UB_1} = \frac{2\sigma_o}{\sqrt{3}} \left(1 - \frac{\ell}{\sqrt{2}}\right) \left(1 + \frac{\ell}{\sqrt{2}}\right) \tag{34}$$

but

$$P_{UB_1} = \overline{\sigma}_{UB}$$

and

$$A_m = 1 - \left(\frac{\ell}{\sqrt{2}}\right)^2$$

therefore,

$$\overline{\sigma}_{UB_1} = \frac{2\sigma_o}{\sqrt{3}} A_m \tag{35}$$

It is noted that a discrepancy arises in the assumed plane strain velocity field where the field of one side ligament intersects that of another side ligament at the RVE edge. This discrepancy will alter the total internal dissipation somewhat but as long as $\ell/\sqrt{2}$ is close to unity, the discrepancy should be small and can be neglected.

For the extension of the proposed upper bound, Eq. 35, to general three-dimensional stress states involving at least one tensile stress, it will be assumed that the preceding velocity field occurs due to the tensile stress regardless of the magnitude of any compressive principal stress. Hence, Eq. 35 is a plane. Since the same analysis holds for the 2 and 3 directions as for the 1 direction, Eq. 35 and permutations thereof leads to three intersecting planes as shown in Fig. 19.

In order to obtain a smaller upper bound in triaxial compression and in compression-compression-tension, it will be assumed that the slits in the structure close and a linear velocity field giving uniform strains $\dot{\epsilon}_1$, $\dot{\epsilon}_2$ and $\dot{\epsilon}_3$ throughout the RVE will occur. The dissipation then becomes

$$\sigma_1 \dot{\epsilon}_1 + \sigma_2 \dot{\epsilon}_2 + \sigma_3 \dot{\epsilon}_3 \tag{36}$$

where $\sigma_1$, $\sigma_2$ and $\sigma_3$ are stresses on the von Mises limit surface where the normal vector has components proportional to $\dot{\epsilon}_1$, $\dot{\epsilon}_2$ and $\dot{\epsilon}_3$. The external work is

$$\overline{\sigma}_1 \; \dot{\epsilon}_1 + \overline{\sigma}_2 \; \dot{\epsilon}_2 + \overline{\sigma}_3 \; \dot{\epsilon}_3 \tag{27}$$

Since the strain rates are arbitrary, the coefficients of each strain rate are set equal giving

$$\overline{\sigma}_i = \sigma_i \tag{38}$$

However, $\sigma_i$ must satisfy the von Mises limit criterion; hence,

$$\frac{1}{2} \left[ (\overline{\sigma}_1 - \overline{\sigma}_2)^2 + (\overline{\sigma}_2 - \overline{\sigma}_3)^2 + (\overline{\sigma}_3 - \overline{\sigma}_1)^2 \right] = \sigma_{my}^2$$

Thus, the intersecting planes in Fig. 19 are cut off by the von Mises cylinder, Eq. 39, as shown in Fig. 19.

The upper bound shown in Fig. 19 has been derived for the case of the gray iron model where the slits define a cube within the RVE. For the nodular iron model, the slits define a sphere within the RVE. In this case the assumptions made in the gray iron upper bound analysis become questionable, particularly the assumption that the change in dissipation due to intersecting deformation fields at the RVE edges is negligible. Therefore, strictly speaking, the lower and upper bounds for gray iron have been determined but only the lower bound for nodular iron has been found. Since the major thrust of the experimental work in Chapter 2 and the subsequent discussions in Chapter 4 involve gray iron, the analysis of the nodular iron in a theoretical context will not be carried further.

Comparison of the upper and lower bound surfaces for the gray iron model, Figs. 16 and 19, reveal that in stress situations involving one or two negative stresses, the bounds are quite far apart. This situation is observed more easily if plane stress surfaces are compared as in Fig. 20. Because of experimental evidence to be presented in the next section, it is believed that the discrepancy in bounds is due to a poor velocity field in the upper bound and that the lower bound is generally closer to the true limit load. Considerable effort has been put into attempting to improve the

upper bound in negative stress situations. This work has met with little success to date and remains an area for future work.

Comparison of Figs. 16 and 19 also reveals regions of coincidence. Three points in the triaxial tension octant have identical lower and upper bounds. This occurs at

$$\overline{\sigma}_1 = \frac{2\sigma_{my}}{\sqrt{3}}, \quad \overline{\sigma}_2 = \overline{\sigma}_3 = \frac{\sigma_{my}}{2} \tag{40}$$

and permutations of this set of equations. Further, in triaxial compression, the lower and upper bounds are identical von Mises cylinders. Hence, for these stress states, the exact limit condition has been obtained.

General three-dimensional limit surfaces are somewhat cumbersome to work with in the comparison and analysis of other theories and data. Further, most microflaw material failure theories available in the literature are of a two-dimensional, plane stress nature. Therefore, in the remainder of this chapter, the plane stress limit surfaces of Fig. 20 will be used but the existence of a general stress state limit surface is an important aspect of the proposed theory.

In applying the proposed theory to actual materials, there are two possible approaches. The first technique is very much the same as previously discussed for the hole model. The hole or flaw radius of the previous discussion is replaced by half the length of the longest flake observed in a cross section of the material. Interparticle center-to-center spacing of the hole model must be replaced by some measure of the eutectic cell size in the flake model. This eutectic cell size can be obtained from proper preparation of the polished surface of the material or by assumption. With the flaw size and spacing parameters determined, the real material RVE is proportioned to the unit cube RVE by means of Eq. 22 as before. Once this is accomplished and a suitable estimate of the matrix material yield strength is made, the upper and lower bounds of the proposed theory are easily obtained.

Another and more practical method of obtaining the parameters for the RVE from an actual material is to simply conduct uniaxial tension and uniaxial compression tests on the material. This information gives two points on the composite yield surface. The compression test gives the strength of the matrix, $\sigma_{my}$ via Eqs. 26, 29 or 31. This point is the same for both upper and lower bounds. The tensile test gives an estimate of the load carrying area, $A_m$ through Eq. 25. The actual gross section failure stress in tension is between $A_m \, \sigma_{my}$ and $1.15 \, A_m \, \sigma_{my}$. Several tensile tests should be conducted and the lowest value taken as $A_m \, \sigma_{my}$. The highest value should then be less than $1.15 \, A_m \, \sigma_{my}$. Once $\sigma_{my}$ and $A_m$ are known, the upper and lower bound equations are determined.

This technique of obtaining the composite yield surface is more practical because metallurgical structures can be complicated in microflawed materials, and determining the microscale parameters via photomicrographs can be difficult.

### 3.4 Comparison of Proposed Failure Theory with Currently Available Theories

In the past, numerous theories for failure of microflawed materials have been developed. Perhaps the simplest of these failure theories was that of Fisher (26). This investigator hypothesized that plastic action occurred at the tip of graphite flakes in gray cast iron at very small loads and that fracture followed soon after. The distortion energy or von Mises criterion for yielding was thought to best characterize this plastic action and it was hypothesized that fracture could also be characterized by this criterion. Fisher further assumed that in tension, microflaws opened and caused stress concentrations in the matrix while in compression, the microflaws tended to close and transmit load. Fisher's aim was to predict the failure of gray cast iron; hence, his model was slanted toward flake type microflaws rather than spherical types. Nevertheless, the equations he developed are general and can be applied to either case.

Coffin (27) considered Fisher's theory to provide a lower bound to the fracture stress of gray cast iron and hypothesized that actual failure stresses should be higher. Therefore, Coffin developed a failure criterion based on the stress concentration at the tip of graphite flakes in gray cast iron. According to Coffin's theory, there is a residual stress at the tip of graphite flakes which arises due to the different thermal expansion characteristics of the graphite and matrix.

In general, Coffin's equations for failure are more complex than Fisher's and require more constants. Further, there seems to be little support for the magnitude of the residual stress term that is required to fit experimental data. Coffin found that a residual stress of 30 ksi was required to fit his equation to experimental data. Clough and Shank (28) later showed that this magnitude for the residual stress is very unlikely.

In a study of masonry failure, Coulomb (29) found that failure occurred when the shear stress on some particular plane reached a critical value. The particular plane of importance in his equation is a material dependent property. Paul (30) later showed that the Coulomb theory incorrectly predicted the orientation of the fracture surface in biaxial tension and in combined tension-compression. This investigator proposed that fracture will occur when either the Coulomb criteria or the maximum tensile strength of the material is reached and whichever is reached first is when failure occurs. Thus, the Coulomb theory is combined with a maximum principal stress criterion to give a fracture theory which Paul found can accurately predict the fracture plane and the stress at fracture.

Marin (31) revised the Coulomb theory by proposing a quadratic relation involving the critical shear and normal stresses on some particular plane rather than a linear relation as originally proposed by Coulomb. Marin's theory generally fits data better than Coulomb's but suffers from the fact that three separate material dependent properties are required.

Babel and Sines (32) developed a fracture criterion for a microflawed material which involves the aspect ratio of an assumed two-dimensional elliptical flaw. The basis of this criterion developed by Babel and Sines was stress concentration equation at various locations around an elliptical flaw which were developed by Inglis (33). No attempt was made in this theory to incorporate a parameter based on the spacing of the flaws. The theory of Babel and Sines predicts that for circular flaws in a brittle matrix the compressive failure stress will be three times the tensile stress while for long, thin elliptical shape flaws the compressive to tensile failure stress ratio approaches seven.

Figure 21 shows the above mentioned theories assuming a tensile stress of 33 ksi and a compressive stress of 100 ksi. All theories except that of Babel and Sines are identical in biaxial tension and agree well with experimental data. In tension-compression, Coffin and Fisher's theories are coincident while Paul's theory is higher in the tension-compression region. In biaxial compression, Fisher's theory in plane stress is just the von Mises ellipse; Coulomb and Marin's theories are straight lines. The theory of Babel and Sines does not include biaxial compression estimates, so this theory is not extended into this quadrant.

Several comments on the currently available failure theories for microflawed materials are in order. Most of the theories discussed involve numerous "material dependent properties" or constants. The theories of Babel and Sines and Fisher have the least number of constants with one. However, the Babel and Sines theory does not include biaxial compression predictions. All of the currently available theories have been developed from two-dimensional models and cannot, in general, be extended in a rigorous manner to three-dimensional stress conditions. Further, none of the theories discussed involve a flaw spacing parameter explicitly and, hence, would predict the same material behavior for all microflawed materials regardless

of flaw spacing. Finally, only the theory of Babel and Sines includes a factor involving the shape of the microflaw.

Comparison of the proposed theory for the slit model with the theories just discussed shows that the lower bound equation is identical to Fisher's theory. This supports Coffin's view that Fisher's theory is a lower bound to failure. Further comparison of the various theories can be made by reconsidering Fig. 21 with the proposed theory upper and lower bounds drawn in. In biaxial tension and combined tension-compression, all existing theories are encompassed by the proposed bounding equations. In biaxial compression, the proposed upper and lower bounds are coincident with each other and with the von Mises ellipse of the matrix material alone.

The essential differences between the proposed theory and those currently available are that the proposed theory incorporates measures of flaw size, shape and spacing whereas none of the other theories include all these factors explicitly. Further, the proposed theory involves a general three-dimensional model and has been extended in a rigorous manner to include general triaxial stress conditions.

## 3.5 Comparison of Proposed Theory with Experimental Data

Comparison of the proposed theory for the hole model with experimental data on this type of material is not practical because there are no materials available which approximate the hole model throughout a given structure in a homogeneous and statistically isotropic manner. Sintered powder metallurgy products come the closest to the model but can not be used for two reasons. First, the objective of the manufacturer of sintered powder products is to decrease the volume fraction of voids. Hence, the volume fraction of voids in commercially available material is quite small, often less than 2%. Secondly, because of the sintered powder process, surfaces of manufactured parts are very dense and porosity is concentrated in the center. The hole model of the proposed theory could be used to model the various

layers is a sintered powder product by changing the size and spacing of the RVE for various layers. However, the analysis of the total layered structure then becomes an important but solvable problem in its own right. This type of analysis is considered to be beyond the scope of the current study and further attention to the hole model is not warranted here.

For the case of the slit model, the model was set up specifically to model cast iron and, therefore, comparison of the proposed theory with experimental data on cast irons should be conducted. Two types of cast irons will be compared with the proposed theory. These are gray and nodular cast irons. Figure 22 shows experimental data on fracture of gray iron tubes under various ratios of applied stress after Cornet and Grassi (35). Also shown in this figure is the Fisher theory, the modified Coulomb-Mohr theory of Paul, and the upper and lower bound of the proposed theory. The proposed theory constants were determined from the tensile and compressive fracture stress using 25 ksi as the tensile failure stress and 90 ksi as the ultimate stress of the matrix alone. The Fisher theory gives a good estimate of the failure stress in biaxial tension but underestimates the failure in tension-compression. The modified Coulomb theory of Paul fits the data slightly better than Fisher's theory. The proposed theory gives upper and lower bounds which are 15% apart in biaxial tension but as much as 50% apart in tension-compression.

Figure 23 shows fracture data on gray cast iron from Coffin (27) along with Coffin's theoretical fracture criterion. Also shown in this figure are the Fisher theory and the upper and lower bounds of the proposed theory. Coffin and Fisher's theory are coincident in biaxial tension and in tension and compression. Fisher's theory in plane stress, and the upper and lower bounds of the proposed theory are coincident in biaxial compression. The lower bound of the proposed theory was based on a matrix ultimate strength of 110 ksi and an $A_m$ of 0.254. These values were chosen to fit the experimental data in uniaxial tension and compression. The

lower bound fits the data fairly well but not as well as the Coffin or Fisher theory. The upper bound is far from the data in tension-compression. In biaxial compression, the upper and lower bounds are coincident and they do not appear to fit the experimental data. This discrepancy is attributed to difficulty in conducting a biaxial compression test (34).

In a study involving experimental data on gray cast iron, Mair (34) found that Fisher's theory was the easiest to use and gave the best overall agreement with the data. Figure 24 shows Mair's comparison (34) in addition to the bounds of the proposed theory. Mair discussed the importance of the third principal stress in biaxial compression and Fig. 24 shows Fisher's theory in both plane stress and in triaxial stress states. The consideration of the third principal stress in Fisher's theory fits the experimental results much better than the plane stress theory. This fact points out the importance of the third stress in biaxial compression. It will again be noted that the upper bound of the proposed theory overestimates the actual failure in the tension-compression quadrant.

Figure 25 shows experimental results of Clough and Shank (28) along with Fisher's theory and the bounds of the proposed theory. In developing Fisher's theory and the proposed theory for this data a value of 140 ksi was used for uniaxial compression and 40 ksi for uniaxial tension failure. Again, Fisher's theory fits the data fairly well, and the upper bound of the proposed theory overestimates the tension-compression failure.

Although the proposed theory gives a rigorous lower bound but no upper bound for the nodular iron model, comparison of the lower bound with experimental data can provide interesting information.

Figure 26 shows experimental results of Cornet and Grassi (36) for nodular iron along with the bound of the proposed theory. The matrix ultimate strength was taken as 75 ksi and the load carrying area was taken as 0.748 square inches. These

values were chosen to fit the experimental data. The lower bound of the proposed theory fit the data well.

Figure 26 also shows experimental data from Clough and Shank (37) for nodular iron. Again, the constants for the lower bound of the proposed solution were chosen to fit the experimental data. The lower bound for the proposed theory again fit the data well.

All of the examples used for comparison thus far have involved fitting the proposed theory to experimental data by using the macroscale uniaxial tension and compression data. This is because the proposed theory requires an accurate determination of the matrix strength as well as the spacing and size of flaws in the matrix. In the investigations previously cited, one or more of these parameters could not be accurately determined. However, in a recent study on nodular cast iron, Testin (38) measured the strength of the matrix material as well as giving photomicrographs of the structure of three nodular cast irons. The matrix strength of the irons was 171 ksi. Three different nodule sizes were studied. The largest nodule size and average center-to-center spacing, as measured from the photomicrographs of Testin, are shown in Table 10. The nodule size and spacing is proportioned to a unit cell size for the model as discussed in an earlier section. The equivalent diameter of the nodule in the unit cell is listed in Table 10 along with the load carrying area. The lower bound is the matrix ultimate stress multiplied by $A_m$. The measured failure stresses for each of the nodule sizes tested are listed in Table 10. The actual failure stress is quite close to the lower bound prediction for the small and medium nodule sizes, but the actual stress is much higher than the lower bound for the large nodule size. This discrepancy in the last case is partially attributable to the fact that the photomicrograph from which the nodule size and spacing were measured contained very few nodules. Hence, it was not possible to determine a statistically significant nodule spacing.

The above correlations of the proposed theory with experimental data indicate that the lower bound is certainly a valid criteria to use for predicting lower bounds on failure stress under various biaxial stress conditions in cases where external notches are not present. In the gray iron model, the upper bound generally overestimates the failure stress, especially in the biaxial tension-compression case. Some currently available theories predict failure stresses better than the proposed theory, but these theories do not permit prediction of failure stresses from microscale quantities alone as does the proposed theory. This ability of the proposed theory was illustrated in the comparison with Testin's data on nodular iron.

Comparison of the proposed theory with investigations aimed at determining the effect of casting variables on failure is also of interest. For example, the theory developed here predicts that the strength of cast iron depends on the size of the graphite flakes in relation to the eutectic cell. If this relation remains the same, the strength of the iron is constant regardless of the absolute size of the graphite. However, experimental evidence (39) shows that cast iron strength increases as graphite absolute size decreases. This apparent anomaly can be explained by considering more carefully the solidification process in production of fine graphite. Fine graphite is produced by cooling molten iron very quickly. However, this process leads to large austenite dendrites. Solidification of the fine graphite occurs after those dendrites are formed and between the dendrite arms. Hence, the theory developed herein is not applicable to the total structure in this case but only to the fine graphite area. The theory developed must then be restricted to usage in cases where graphite is large, completely random in spacing and the austenite dendrites are small. This implies use only in cases of slowly cooled cast iron.

The existence of von Mises behavior in cast iron under triaxial compression loading is predicted by the proposed theory and has been studied to some extent by Brandes (40). This investigator subjected nodular cast iron to a hydrostatic com-

pressive stress of $-136$ kg/mm$^2$ then applied tensile stress to one axis until failure occurred. Application of the three-dimensional form of the von Mises theory with $\sigma_1$ and $\sigma_2$ equal to $-136$ kg/mm$^2$ and the materials tensile strength equal to Brandes' uniaxial tensile strength (48.4 kg/mm$^2$) gives

or

$$\left.\begin{array}{c} (48.4)^2 = \frac{1}{2}\left[(-136 - \sigma_3)^2 + (\sigma_3 + 136)^2\right] \\[2mm] \sigma_3 = -87 \text{ kg/mm}^2 \end{array}\right\} \qquad (46)$$

Brandes found that the $\sigma_3$ stress was $-84$ kg/mm$^2$ for failure. Although this is only one test, it does indicate that the predicted behavior from the proposed model in triaxial compression is reasonable.

Now that the limit surface for the microflawed material without macroscale notches has been obtained and its validity verified with experimental results, the case of macroscale notches can be studied. This extension of the proposed theory comprises Chapter 4.

## 4. MACROSCALE LIMIT ANALYSIS OF A MICROFLAWED MATERIAL

### 4.1 Introduction

Now that the limit behavior of a microscale representative element has been obtained, the limit surface can be used in macroscale analyses. As previously stated, since the modeled element is representative, any structure can be built up by stacking elements; hence, the RVE limit surface can be applied directly to the macroscale problem. The macroscale limit analysis is conducted by using the microscale RVE limit condition developed herein as the material continuum limit condition. This extension is valid under the conditions set by Majumdar and McLaughlin (16) and discussed in Chapter 3.

Three types of notched specimens will be studied. These are the double edge cracked plate, the circumferential notched bar, and the notched three point bend bar. The analyses will employ the RVE limit surfaces of the flake model obtained in Chapter 3. Specifically, the limit surfaces of the gray iron model, Fig. 16 and 19 will be used. In order to reduce the number of calculations in this section, only an estimated single limit surface will be used here. This estimated surface is shown in Fig. 27 and represents a limit surface between the established lower and upper bounds of Chapter 3.

The results of the macroscale analyses of the various specimens will be compared with the experimental data from the current study presented in Chapter 2.

### 4.2 Macroscale Analysis of a Double Edge Cracked Plate in Tension

The configuration of the specimen to be studied here is shown in Fig. 6. The plate width is W, the thickness is t, and the crack depth is "a" from each side of the plate. A simple lower bound is obtained by considering a structural member to extend through the center of the plate as shown in Fig. 28. The lower limit load of the structure is the limit load of this member or

$$P_{LB} = \sigma_{oc} (W - 2a) t \tag{42}$$

where $P_{LB}$ is the lower bound limit load, and $\sigma_{oc}$ is the limit stress of the micro-flawed material in uniaxial tension. An upper bound for the limit load can be obtained by considering a normal displacement velocity field as shown in Fig. 28. This assumed field requires no strain in the other two directions of the plate. Referring to Fig. 27, the uniaxial strain assumed implies rate vector is normal to point L. Hence, the internal energy dissipated by the assumed displacement is

$$\int_V \sigma_{ij} \, \dot{\epsilon}_{ij} \, dV = 1.15 \, \sigma_{oc} \, \dot{u} \, t(W - 2a) \tag{43}$$

The external work is the external load, $P_{UB}$, multiplied by the external displacement or

$$P_{UB} \, \dot{u} \tag{44}$$

Setting the external work equal to the internal work gives

$$P_{UB} = 1.15 \, \sigma_{oc} \, t(W - 2a) \tag{45}$$

In this case, the upper and lower bounds are within 15% of each other.

In this expression developed, $\sigma_{oc}$ is the limit stress of the RVE in uniaxial tension. Using a $\sigma_{oc}$ of 42.5 ksi, which is the ultimate stress of test P-M-2 from Table 4, and the specimen dimensions of DEC 3 and 4 from Table 8, the two bounds are

$$P_{LB} = 42.5 \, (1) \, (1.12) = 47.6 \text{ kips} \tag{46}$$

and

$$P_{UB} = 1.15 \, (P_{LB}) = 54.76 \text{ kips} \tag{47}$$

From Table 8, the fracture loads for these two specimens were 43.9 and 47 kips. Thus, the actual failure loads lie below, but close to, the predicted bounds of limit analysis.

Returning to the linear elastic fracture mechanics techniques and using $K_{lc}$ = 18.8 ksi$\sqrt{in.}$, a failure load prediction of 25.3 kips is obtained. This value under-estimates the failure load of the DEC specimens. Thus, it appears that gray cast iron with macroscale notches may be too ductile to utilize LEFM techniques but not ductile enough to enable the use of limit analysis. Nevertheless, LEFM provides a lower bound to failure while limit analysis gives an upper bound.

## 4.3 Macroscale Analysis of a Circumferential Notched Round Bar

The analysis for this case is almost the same as for the double edge cracked plate; hence, the analysis will not be repeated. The comparison with the data of the current study can be accomplished with one minor change in the previous equation. Instead of $B(W - 2a)$ in the bound equation, the expression $\pi/D'^2$ where D' is the diameter at the notch must be substituted in the double edge cracked plate equation. From Table 7, the three diameters tested were 0.354, 0.707 and 1.59 inches. Figure 29 is a plot of the specimen area at the notch versus the failure load. The data points are for the specimens tested, the solid lines are on LEFM methods. In the low load, small cross sectional area region of the plot, the data and the two theoretical techniques are quite close together but as specimen size increases, the LEFM technique provides a lower bound to failure and the proposed limit analysis approach gives an upper bound. It is noted that the actual failure loads follow the general trend of the fracture mechanics prediction rather than the limit analysis prediction. Thus, for tensile loading of notched bars of gray cast iron, LEFM techniques provide a close but conservative estimate of failure loads.

## 4.4 Macroscale Analysis of a Notched Three Point Bend Bar

In conducting the lower bound analysis of three point bend bars, the 3PB configuration can be replaced by a pure bending configuration with moment, M equal to PS/4 where P is the load from 3PB bar and S is the span length in the 3PB specimen.

This external moment must be resisted by the internal moment set up by the fully plastic tensile and compressive stresses as shown in Fig. 30. The tensile and compressive loads must be equal but since the tensile and compressive limit stresses are not equal, the areas of tensile load and compressive load can not be equal. Hence, as shown in Fig. 30, the tensile load $P_T$ is

$$P_T = \sigma_{oc} \, (c) \, t \tag{48}$$

and the compressive load, $P_C$ is

$$P_C = \sigma_c \, (B - C) \, t \tag{49}$$

where C is depth of beam subject to tensile stress, B is the total depth of the beam at the notch and t is the thickness of the beam. Setting $P_T = P_C$ and letting R = $\sigma_{oc}/\sigma_{Comp}$ gives

$$C = \frac{B}{(1 + R)} \tag{50}$$

The internal moment is

$$M = \frac{\sigma_{oc} \, B^2}{2} \left\{ \frac{1}{1 + R} \right\} t \tag{51}$$

Setting the internal moment equal to the external moment, gives the lower bound limit load

$$P_{LB} = \frac{2\sigma_{oc} \, B^2}{S} \left\{ \frac{1}{1 + R} \right\} t \tag{52}$$

An upper bound is somewhat more difficult to obtain when the material has different tensile and compressive limit loads. For the upper bound, a collapse mode must be developed. The assumed collapse mode is shown in Fig. 30. The energy dissipated in the deforming triangular region in the center of the bar can be easily calculated from

$$\int \sigma_{ij} \, \dot{\epsilon}_{ij} \, dV \tag{53}$$

The strain in the deforming region is uniaxial tension. Hence,

$$\sigma_{ij} \, \dot{\epsilon}_{ij} = \sigma_{oc} \, \dot{\epsilon}_1 \tag{1.15}$$
$$(54)$$

but,

$$\dot{\epsilon}_1 = \left(\frac{2\Delta B}{S}\right) \tag{55}$$

for a unit base of the triangular deforming region. $\Delta$ is the maximum beam velocity. The volume integral (53) in this case reduces to

$$\frac{\Delta B^2 \, t \, \sigma_{oc}}{S} \tag{2.30}$$
$$(56)$$

The external work done is $P \cdot \Delta$ so that the upper bound load $P_{UB}$ is

$$P_{UB} = \frac{B^2 \, t \, \sigma_{oc}}{S} \tag{2.30}$$
$$(57)$$

The ratio of the lower to upper bounds is

$$\frac{P_{LB}}{P_{UB}} = \left\{\frac{1}{1+R}\right\} \tag{0.87}$$
$$(58)$$

The next step is to compare the limit load prediction with experimental data from this study. For the gray cast iron under study, $R = 1/3$ and $\sigma_{oc}$ is 42.5 ksi. B is the depth of the beam at the notch. Using $S = 12.89$ from Table 5, and calculating the limit load for various B values, a trend is evident. Figure 31 is a plot of crack length a, which is simply $(3.22 - B)$ versus the limit load stress. The solid lines are the lower bound using $\sigma_{oc}$ of 42.5 ksi and the upper bound using 1.53 times the lower bound. The actual data points from all tests listed in Table 5 are indicated as well as the predictions of LEFM based on a fracture toughness of $18.8$ ksi $\sqrt{in}$. Again, the LEFM predictions fall below the data while the limit analysis approach provides an upper bound.

## 4.5  Conclusions of Macroscale Analysis

From the comparison of experimental data with the LEFM techniques and limit analysis predictions, it can be concluded the LEFM method should provide lower bound predictions of failure in notched gray iron parts while limit analysis should always provide an upper bound. The implication of this conclusion is that gray cast iron, in a macroscale notched situation, is too ductile to validate strict use of LEFM but not ductile enough to permit the strict application of limit analysis.

McLaughlin (22), has shown that limit analysis will always provide an upper bound to the failure load of a material which lacks sufficient ductility for strict application of limit theory. Indeed, this view is supported by the results of the current study.

In order to obtain a better estimate of the actual failure load in cast iron parts, two alternatives appear. The first is to modify LEFM methods while the second is to modify limit analysis techniques to account for limited ductility. The first method is under study by others and is subject to the objections raised in Chapter 2. The second alternative may prove useful and a simple technique can be used to enable better prediction of the 3PB test data.

Although it must be conceded that limit analysis is not strictly applicable to gray cast iron in bending, the remaining beam depth, B can be artificially reduced by some amount, $\delta$ to account for the lack of tensile ductility and subsequent pre-catastrophic crack extension. This $\delta$ value will be material dependent but should be geometry independent. In order to determine a $\delta$ for the case at hand, a crack length of 0.5 inches (B = 2.72) will be used. Further, assume that the desired lower bound limit load is 16.5 kips for the case of a = 0.5. Using Eq. 52 and solving for (B - $\delta$) where (B - $\delta$) takes the place of B, gives

$$(B - \delta) = 1.824 \tag{59}$$

but B is originally 2.72; therefore,

$$\delta = 0.8957 \tag{60}$$

This is the amount of crack extension which should be added to the original crack length, a, in order to have the limit analysis solution match the actual data. If this δ is a material property, one should be able to take all of the 3PB tests, add δ to the actual crack lengths and predict failure using (B - δ) in Eq. 52. This exercise has been carried out and Fig. 31 shows the results. Note that the actual data fall either within the limits or reasonably so.

The above modification of limit analysis remains to be proven more extensively. There are a number of important questions which must be answered. For example, is the δ factor geometry independent or will it change with beam depth or thickness? An important theoretical question is, "Is the modified remaining ligament fully plastic at failure?" If not, use of limit analysis is on poor footing. The conclusion and use of the above operational procedure must be viewed as preliminary in nature at this time. Nevertheless, the procedure is interesting and certainly can be used to predict the results in the current case.

# 5. SUMMARY, CONCLUSIONS AND RECOMMENDATIONS FOR FUTURE STUDY

## 5.1 Summary and Conclusions

It has been shown, using experimental data gathered from various specimen geometries, that linear elastic fracture mechanics cannot be used to predict failure in gray cast iron independent of geometry. It may be possible to predict precatastrophic crack extension or provide a lower bound estimate of failure by using plane strain fracture toughness, but prediction of accurate failure loads is not possible. It has also been shown that specimen and test criteria currently used in plane strain fracture toughness testing lead to discrepancies in the case of cast iron.

In an effort to provide a failure prediction technique for cast iron, a study of limit analysis techniques applied to general microflawed materials with ductile matrices was undertaken. The method employed was to develop general limit surfaces for microscale representative elements of the material. These limit criteria were then used in macroscale analysis. The proposed theory was compared with currently available theories for microflawed material as well as experimental data on smooth specimen tests of gray and nodular cast irons. Most theories and experimental data for smooth specimen cases fell within the bounds of the proposed theory. Generally, those experimental results falling outside the proposed theory are attributable to experimental difficulty in combined stress testing of smooth specimens. The proposed theory differs from others in two major respects. First, the proposed theory includes measures of microflaw size, shape, spacing, and matrix strength properties explicitly, whereas other theories include these factors implicitly through macroscale measures such as tensile and compressive strength. Also, the proposed theory has been developed for general three-dimensional stress states where most other theories have been applied to plane stress only.

The limit surfaces obtained from the microscale RVE model of gray cast iron has been extended to the macroscale, and three macroscale fracture toughness speci-mens have been analyzed using limit analysis. The results of this analysis and com-parison with data indicate that limit analysis techniques provide an upper bound to the failure load of gray cast iron parts with notches. In the case of three point bend bars, the limit analysis solution may be modified by a material dependent constant to permit prediction of failure loads for this geometry.

The overall conclusions of this study are as follows:

(1) Linear elastic fracture mechanics methods will give lower bound predictions for gray cast iron failure loads in cases where macro-scale notches are present. However, gray cast iron is too ductile on the microscale to permit accurate failure load prediction using fracture mechanics.

(2) Limit analysis methods applied to microscale representative ele-ments of microflawed materials permits the development of limit surfaces, in general, three-dimensional stress states. These limit surfaces are functions of the flaw size, shape and spacing as well as the strength of the ductile matrix material. Further, these limit surfaces agree well with experimental data from smooth specimen tests.

(3) Microscale limit surfaces for gray cast iron, when extended to the macroscale and used in limit analysis of notched parts, provides an upper bound to the actual failure loads. It has been shown that gray cast iron, especially in bending situations, is not ductile enough to permit the strict application of limit analysis tools.

## 5.2   Recommendations for Future Study

(1) In the case of the RVE of the hole model, better velocity fields for the upper bound are needed. The object of a study in this area should be to cut off the upper bound von Mises cylinder in triaxial tension and compression in order to get the lower and upper bounds closer in these octants.

(2) For real materials with a distribution of flaw sizes, an experimental study is necessary to determine which measure of flaw size distribution will provide the best correlation with the proposed theory and real materials.

(3) For the case of the slit model, better bounds are needed. The object of study here would be to obtain closer bounds in combined stress situations involving tension and compression stresses.

(4) An upper bound analysis is necessary for the slit model when the slits form a spherical surface in the RVE.

(5) Limit analysis techniques should be extended to cases involving adjacent RVE's with different properties. The object here is to model materials which are nonhomogeneous. This would enable the theory to be extended to quickly cooled cast irons which have dendritic structure.

(6) The modifications to the limit analysis of bending situations should be investigated more thoroughly. A study should be made of the artificial extension of the crack in bending cases to determine if the amount of the extension is a material dependent property and if it is affected by specimen geometry.

LIST OF REFERENCES

1.   Gilbert, J. N. J., "Factors Relating to the Stress-Strain Properties of Cast Iron," BCIRA Journal, Vol. 6, No. 11, April 1957, pp. 546-585.

2.   Glover, A. G., "The Fracture Mechanics of Grey Cast Iron," Pn. D. thesis, University of Leeds, Dept. of Metallurgy, August 1968.

3.   Glover, A. G. and Pollard, G., "The Brittle Fracture of Grey Cast Iron," Paper No. 29 in Fracture 1969, Proceedings of 2nd Int'l. Conf. on Fracture, Brighton, U. K., April 1969, P. L. Pratt, editor, Chapman and Hall, Ltd., pp. 350-359.

4.   Brandt, D. E., "Crack Growth and Fracture Characterization of Ductile Iron, Gray Iron and 0.25% Carbon Cast Steel," General Electric Company report, Gas Turbine Dept., Data Folder No. 71-GTD-17, July 1971.

5.   Lazaridis, A., Worzala, F. J., Loper, C. R. and Heine, R. W., "Fracture Toughness of Ductile Cast Irons," American Foundrymen's Society Transactions, Vol. 79, 1971, pp. 351-360.

6.   Lazaridis, A. S., Loper, C. R. and Worzala, F. J., "The Influence of Microstructural Constituents on the Fracture Toughness of Nodular Cast Iron," Mechanical Behavior of Materials, Vol. 1, August 1971, pp. 525-542.

7.   Drucker, D. C., Prager, W. and Greenberg, H. J., "Extended Limit Design Theorems for Continuous Media," Quarterly of Appl. Math., Vol. 9, No. 4, 1952, pp. 381-389.

8.   Gaydon, F. A., "On the Yield-Point Loading of a Square Plate with Concentric Circular Hole," Journal of Mech. and Physics of Solids, Vol. 2, 1954, pp. 170-176.

9.   Gaydon, F. A. and McCrum, A. W., "A Theoretical Investigation of the Yield Point Loading of a Square Plate with a Central Circular Hole," Journal of Mech. and Physics of Solids, Vol. 2, 1954, pp. 156-169.

10.  O'Donnell, W. J. and Porowski, J., "Yield Surfaces for Perforated Materials," Journal of Appl. Mech., Vol. 40, No. 1, March 1973, pp. 263-270.

11.  Drucker, D. C. and Prager, W., "Soil Mechanics and Plastic Analysis or Limit Design," Quarterly of Appl. Math., Vol. 10, No. 2, July 1952, pp. 157-165.

12.  Drucker, D. C., "Limit Analysis of Two and Three Dimensional Soil Mechanics Problems," Journal of Mech. and Physics of Solids, 1953, Vol. 1, pp. 217-226.

13.  Drucker, D. C., "On Structural Concrete and the Theorems of Limit Analysis," Publications of the Int. Assoc. for Bridge and Structural Engineering, Vol. 21, 1961, pp. 49-59.

14. McLaughlin, P. V., Jr. and Batterman, S. C., "Limit Behavior of Fibrous Materials," Int. Journal of Solid Structures, 1970, Vol. 6, pp. 1357-1376.

15. McLaughlin, P. V., Jr., "Plastic Limit Behavior and Failure of Filament Reinforced Materials," Int. Journal of Solid Structures, 1972, Vol. 8, pp. 1294-1318.

16. Majumdar, S. and McLaughlin, P. V., Jr., "Application of Limit Analysis to Composite Materials and Structures," under review.

17. Frishmuth, R. E. and Sinclair, G. M., "Fracture Mechanics Testing of Class 60 Cast Iron," Research report to Scott Paper Company, 1970.

18. Brown, W. F. and Srawley, J. E., Plane Strain Crack Toughness Testing of High Strength Metallic Materials, ASTM STP-410, American Society for Testing and Materials, Philadelphia, Pennsylvania, 1966, pp. 8-16.

19. Ostensson, B., "Ultrasonic Cracklength Determination During Fracture Toughness Testing of Gray Cast Iron," Eng. Frac. Mech., 1972, Vol. 4, pp. 443-448.

20. Draffin, J. O. and Collins, W. L., "Mechanical Properties of High-Strength Cast Iron," Proceedings of ASTM, Vol. 39, 1939, pp. 589-603.

21. Drucker, D. C., "Macroscopic Fundamentals in Brittle Fracture," Chapter 8, Vol. 1, in Fracture, edited by Liebowitz, Academic Press, New York, 1968, pp. 474-529.

22. McLaughlin, P. V., Jr., "Properties of Work-Hardening Materials with a Limit Surface," Journal of Appl. Mech., September 1973, pp. 803-807. See also: McLaughlin, P. V., Jr., "An Upper Bound to First Failure Loads," to be published.

23. Underwood, E. E., Quantitative Sterology, Addison-Wesley, Reading, Mass., 1970, pp. 80-113.

24. Morrogh, H., "Graphite Formation in Gray Cast Irons and Related Alloys," BCIRA Journal of Research and Development, Vol. 5, June 1955, pp. 655-673.

25. Drucker, D. C., "A More Fundamental Approach to Plastic Stress-Strain Relations," Proceedings of the First U. S. National Congress of Applied Mechanics, ASME, 1951, pp. 487-491.

26. Fisher, J. C., "A Criterion for the Failure of Cast Iron," ASTM Bulletin, April 1952, pp. 74-75.

27. Coffin, L. F., "The Flow and Fracture of a Brittle Material," Journal of Appl. Mech., September 1950, pp. 233-248.

28. Clough, W. R. and Shank, M. W., "The Deformation and Rupture of Gray Cast Iron," Trans. of ASM, Vol. 49, 1952, pp. 241-262.

29. Coulomb, C. A., "On the Application of the Rules of Maxima and Minima to Some Problems of Statics Relating to Architecture," Memoires de Mathematique et de Physique (Academie Royal des Sciences, par divers Savans, 1773, Paris 1776).

30. Paul, B., "A Modification of the Coulomb-Mohr Theory of Fracture," Journal of Appl. Mech., June 1961, pp. 259-268.

31. Marin, J., Mechanical Behavior of Engineering Materials, 1962, Prentice-Hall International, London, p. 126.

32. Babel, H. W. and Sines, G., "A Biaxial Fracture Criteria for Porous Brittle Materials," ASME Preprint, Paper No. 68-WA/Met-12.

33. Inglis, C. E., "Stresses in a Plate Due to the Presence of Cracks and Sharp Corners," Proceedings of Institute for Naval Architects, Vol. 55, 1913, pp. 219-230.

34. Mair, W. M., "Fracture Criteria for Cast Iron under Biaxial Stresses," Journal of Strain Analysis, Vol. 3, No. 4, October 1968, pp. 254-263.

35. Cornet, I. and Grassi, R. C., "Fracture of Gray-Cast-Iron Tubes under Biaxial Stresses," Journal of Appl. Mech., June 1949, pp. 178-182.

36. Cornet, I. and Grassi, R. C. "A Study of Theories of Fracture under Combined Stresses," Journal of Basic Engineering, March 1961, pp. 39-44.

37. Clough, W. R. and Shank, M. E., "The Flow and Fracture of Nodular Cast Iron," Trans. of ASME, Vol. 79, 1956, pp. 1911-1920.

38. Testin, R. A., "Characterization of the Cyclic Deformation and Fracture Behavior of Nodular Cast Iron," Dept. of Theoretical and Appl. Mech., University of Illinois, T. & A.M. Report No. 371, June 1973.

39. Adams, R. R., "Cast Iron Strength vs. Structure," Trans. of American Foundrymen's Association, Vol. 50, 1943, pp. 1063-1097.

40. Brandes, M. "Studies in Large Plastic Flow of Cast Iron Specimens Stretched under Hydrostatic Pressures of Up to 17500 kg/cm$^2$," Int. Journal of Fracture Mechanics, Vol. 3, September 1967, pp. 175-183.

41. Paris, P. C. and Sih, E. C., "Stress Analysis of Cracks," Fracture Toughness Testing and Its Applications, ASTM STP-381, American Society for Testing and Materials, 1965, pp. 30-81.

42. "Standard Method of Test for Plane Strain Fracture Toughness of Metallic Materials," ASTM Spec. E399-72, ASTM Book of Standards, Part 31, 1972, pp. 955-974.

TABLE 1

FRACTURE TOUGHNESS DATA FOR DUCTILE AND
GRAY CAST IRON FROM BRANDT (4)

| | Specimen | Temp. °F | $K_{max}$ (ksi$\sqrt{in.}$) | $K_Q$ (ksi$\sqrt{in.}$) |
|---|---|---|---|---|
| Ductile Iron | 1 | - 50 | --- | 14.5** |
| (ASTM Grade | 2 | -320 | 42.4 | 27.0 |
| 60-40-18 from | 3 | -320 | 42.5 | 16.2 |
| Specimen A536)* | | | | |
| Gray Iron | 1 | - 50 | 37.62 | 10.0** |
| | 2 | -320 | 23.9 | 23.9 |
| (ASTM Class 40)* | 3 | -320 | 24.8 | 24.4 |

*Classification is approximate
**Based on 5% offset on P-v record

## TABLE 2

### FRACTURE TOUGHNESS DATA FOR DUCTILE CAST IRON AT -40°F FROM LAZARIDIS ET AL. (5)

| Specimen No. * | $\dfrac{K_{Ic} = K_Q}{\text{(ksi}\sqrt{\text{in.}})}$ | Average $K_{Ic}$ (ksi$\sqrt{\text{in.}}$) |
|---|---|---|
| 55-1 | 17.71 | |
| 55-2 | 17.47 | |
| 55-3 | 17.62 | 17.60 |

*Specimen numbers from Ref. 5

TABLE 3

METALLURGICAL COMPOSITION OF CLASS 60
PEARLITIC GRAY CAST IRON TESTED IN THE CURRENT PROGRAM

| C | Mg | Si | P | S | Ni | Cr | Mo | Cu |
|------|------|------|------|------|------|------|------|------|
| 2.95 | 0.85 | 1.32 | 0.09 | 0.05 | 2.28 | 0.06 | 0.73 | 0.13 |

## TABLE 4

### TENSILE TEST DATA - PEARLITIC CAST IRON

| Specimen | Shank | Fracture Location | Location Through Shell | Maximum Load (kips) | Maximum Elongation (in.) | $\sigma$ Proport. Limit (ksi) | $\sigma_y$ 0.2% Offset (ksi) | $\sigma$ Ultimate (ksi) |
|---|---|---|---|---|---|---|---|---|
| P-1 | Reduced | Center | Unknown | 6.39 | 0.01025 | 31.0 | 47.2 | 50.6 |
| P-2 | Straight | Grip | Unknown | 9.25 | 0.0106 | 21.6 | 41.2 | 47.1 |
| P-3 | Reduced | Center | Unknown | 6.45 | 0.0087 | 28.1 | 49.6 | 51.8 |
| P-0-1 | Reduced | Center | Outer 1/3 | 6.65 | 0.014 | 23.8 | 45.6 | 52.7 |
| P-0-2 | Reduced | Center | Outer 1/3 | 6.70 | 0.0138 | 22.8 | 45.6 | 53.1 |
| P-M-1 | Reduced | Fillet | Middle 1/3 | 4.30 | 0.0048 | 16.7 | --- | 34.1 |
| P-M-2 | Reduced | Center | Middle 1/3 | 5.35 | 0.0074 | 22.2 | 42.5 | 42.5 |
| P-I-1 | Reduced | Center | Inner 1/3 | 6.80 | 0.0138 | 22.8 | 46.8 | 54.0 |
| P-1-2 | Reduced | Center | Inner 1/3 | 6.85 | 0.0142 | 23.8 | 47.6 | 54.4 |

## TABLE 5

### THREE POINT BEND TEST RESULTS

| | | | | | |
|---|---|---|---|---|---|
| S = 12.89 | | FC | Fatigue Precracked | | |
| B = 1.00 | | T | Elevated Temp. | | |

| Specimen No. | Crack Length (a) (inch) | Fracture Load, kips (P) | Depth (w) (inch) | $K_{max}$ (ksi $\sqrt{in.}$) | Comments |
|---|---|---|---|---|---|
| 3PB-1 | 0.60 | 18.8 | 3.22 | 44.0 | |
| 3PB-2 | 0.60 | 18.7 | 3.22 | 43.7 | |
| 3PB-3 | 1.29 | 8.5 | 3.22 | 37.8 | |
| 3PB-4 | 1.29 | 8.3 | 3.22 | 36.9 | |
| 3PB-FC-1 | 0.65 | 15.4 | 3.22 | 40.0 | |
| 3PB-FC-2 | 0.65 | 16.6 | 3.22 | 43.1 | |
| 3PB-FC-3 | 0.65 | 16.9 | 3.22 | 44.1 | |
| 3PB-FC-4 | 0.65 | 16.3 | 3.22 | 42.4 | |
| 3PB-T-1 | 0.50 | 19.4 | 3.20 | 44.0 | 200°F |
| 3PB-T-2 | 0.50 | 19.1 | 3.20 | 43.3 | 200°F |
| 3PB-T-3 | 0.50 | 18.9 | 3.20 | 42.9 | 300°F |
| 3PB-T-4 | 0.50 | 17.1 | 3.20 | 38.8 | 300°F |
| 3PB-T-5 | 0.50 | 17.4 | 3.20 | 39.5 | 400°F |
| 3PB-T-6 | 0.50 | 17.8 | 3.20 | 40.4 | 400°F |

## TABLE 6

### COMPACT SPECIMEN TEST DATA

$W = 2.0$ $\quad$ $B = 1.0$

| Specimen No. | Crack Length (a) (inch) | Fracture Load, kips (P) | $K_{max}$ (ksi$\sqrt{in.}$) |
|---|---|---|---|
| CT-2 | 0.90 | 6.0 | 35.3 |
| CT-3 | 0.90 | 5.15 | 30.3 |
| CT-4 | 0.90 | 4.75 | 28.0 |
| CT-5 | 0.90 | 6.36 | 37.4 |
| CT-6 | 0.90 | 6.18 | 36.4 |
| CT-7 | 0.90 | 6.02 | 35.4 |
| CT-8 | 0.90 | 4.30 | 25.3 |

TABLE 7

CIRCUMFERENTIAL NOTCH TENSION DATA

| Specimen No. | Nominal Diameter D (in.) | Diameter at Notch d (in.) | Fracture Load, kips (P) | $K_{max}$ (ksi $\sqrt{in.}$) |
|---|---|---|---|---|
| CNT-1 | 0.50 | 0.354 | 4.00 | 13.6 |
| CNT-2 | 0.50 | 0.354 | 4.70 | 16.0 |
| CNT-3 | 0.50 | 0.354 | 4.74 | 16.1 |
| CNT-4 | 0.50 | 0.354 | 5.60 | 19.1 |
| CNT-7 | 2.25 | 1.59 | 56.0 | 19.9 |
| CNT-8 | 2.25 | 1.59 | 64.0 | 22.7 |
| CNT-9* | 1.00 | 0.707 | 17.0 | 20.4 |
| CNT-10* | 1.00 | 0.707 | 18.1 | 21.7 |
| CNT-11* | 1.00 | 0.707 | 18.9 | 22.7 |
| CNT-12* | 0.500 | 0.354 | 4.96 | 16.8 |
| CNT-13* | 0.500 | 0.354 | 5.01 | 17.0 |
| CNT-14* | 0.500 | 0.354 | 5.84 | 19.8 |

*Recalculated data from Drexel Institute of Technology

## TABLE 8

### DOUBLE EDGE CRACK PLATE DATA

B = 1.00

| Specimen No. | Crack Length (a) (inch) | Fracture Load, kips (P) | Depth (w) (inch) | $K_{max}$ (ksi $\sqrt{in.}$) |
|---|---|---|---|---|
| DEC-2 | 0.75 | 36.0 | 2.688 | 24.6 |
| DEC-3 | 0.75 | 47.0 | 2.62 | 33.1 |
| DEC-4 | 0.75 | 43.9 | 2.62 | 30.9 |
| DEC-5 | 0.95 | 48.5 | 3.01 | 35.4 |

## TABLE 9

### PEARLITIC GRAY CAST IRON DATA SUMMARY

| Specimen No. | $K_{max}$ ksi√in. | $K_Q$ ksi√in. |
|---|---|---|
| 3PB-1 | 44.0 | |
| 3PB-2 | 43.7 | |
| 3PB-3 | 37.8 | |
| 3PB-4 | 36.9 | |
| 3PB-FC-1 | 40.0 | |
| 3PB-FC-2 | 43.1 | |
| 3PB-FC-3 | 44.1 | |
| 3PB-FC-4 | 42.4 | |
| 3PB-T-1 | 44.0 | |
| 3PB-T-2 | 43.3 | |
| 3PB-T-3 | 42.9 | |
| 3PB-T-4 | 38.8 | |
| 3PB-T-5 | 39.5 | |
| 3PB-T-6 | 40.4 | |
| CT-2 | 35.3 | |
| CT-3 | 30.3 | |
| CT-4 | 28.0 | |
| CT-5 | 37.4 | |
| CT-6 | 36.4 | |
| CT-7 | 35.4 | |
| CT-8 | 25.3 | |
| P-Pδ-1 | | 21.0 |
| P-Pδ-2 | | 18.8 |
| P-Pδ-3 | | 32.0 |
| P-CNT-1 | 13.6 | |
| P-CNT-2 | 16.0 | |
| P-CNT-3 | 16.1 | |
| P-CNT-4 | 19.1 | |
| P-CNT-7 | 19.9 | |
| P-CNT-8 | 22.7 | |
| P-CNT-9* | 20.4 | |
| P-CNT-10* | 21.7 | |
| P-CNT-11* | 22.7 | |
| P-CNT-12* | 16.8 | |
| P-CNT-13* | 17.0 | |
| P-CNT-14* | 19.8 | |
| P-DEC-2 | 24.6 | |
| P-DEC-3 | 33.1 | |
| P-DEC-4 | 30.9 | |
| P-DEC-5 | 35.4 | |

*Recalculated data from Drexel Institute of Technology

TABLE 10

SUMMARY OF MICROFLAW PARAMETERS OF NODULAR IRONS STUDIED BY TESTIN (38)

| Largest Nodule Diameter | Center to Center Spacing | Nodule Diameter on Unit Cell Basis | Load Carrying Area | Lower Bound Stress | Actual Failure Stress |
|---|---|---|---|---|---|
| .00125 | 0.0037 | 0.585 | 0.731 | 125.0 | 134 |
| .0025 | 0.0070 | 0.618 | 0.700 | 119.7 | 135 |
| .0045 | 0.010 | 0.779 | 0.523 | 89.4 | 125 |
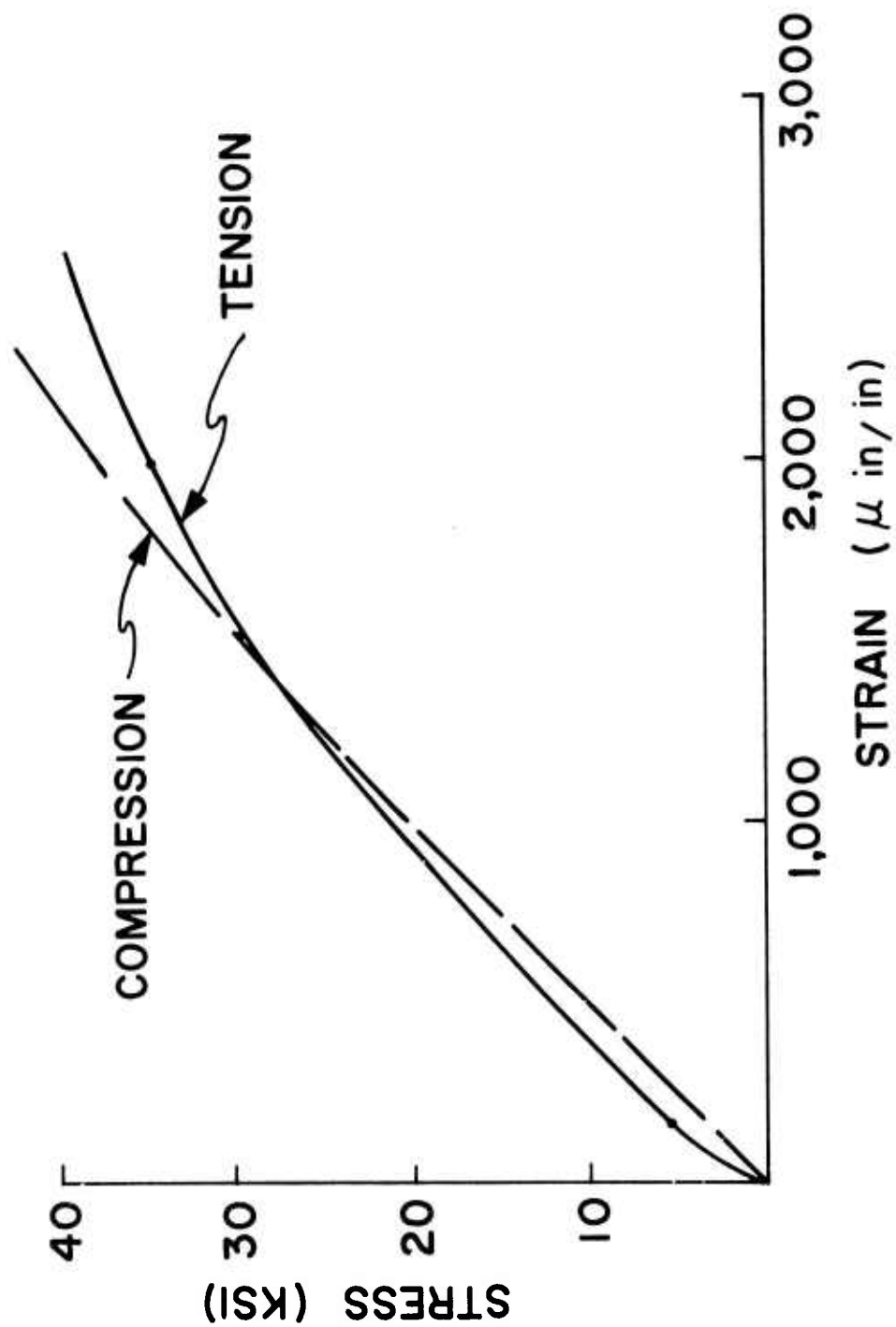
Fig. 1  Tensile and Compressive Stress-Strain Curves
for Class 60 Gray Cast Iron
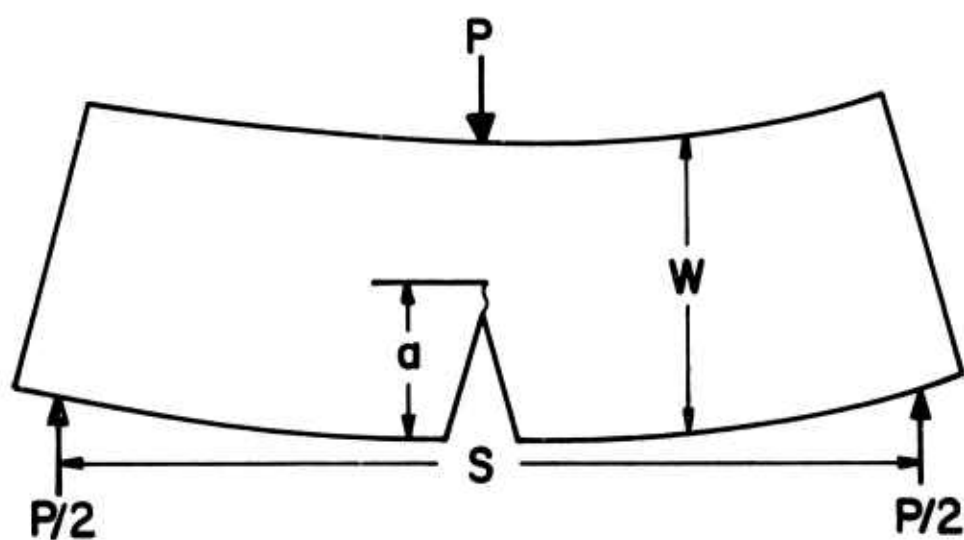
Fig. 2    Three Point Bend Specimen Dimensions
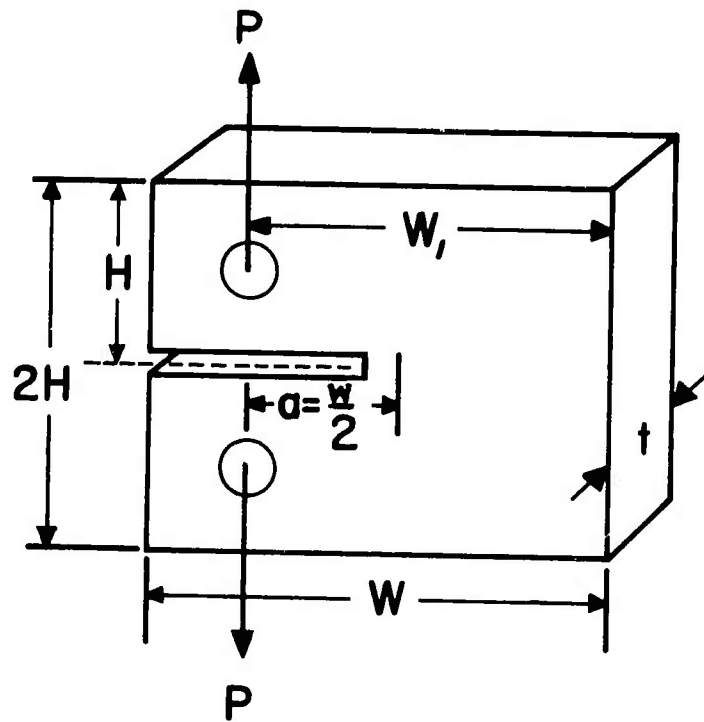
(A) COMPACT SPECIMEN
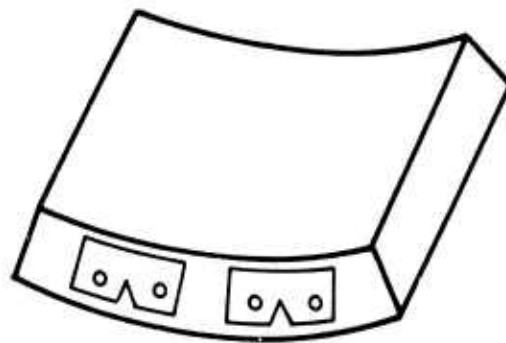


(B) BULK MATERIAL SHOWING
SPECIMEN LOCATION

Fig. 3   Compact Specimen Dimensions

| SPECIMEN | $P_Q$ (KIPS) | $K_Q$ (KSI $\sqrt{IN}$) | PLANE STRAIN VALIDITY |
|---|---|---|---|
| P-P $\delta$-1 | 5.7 | 21 | MARGINAL |
| P-P $\delta$-2 | 5.12 | 18.8 | VALID |
| P-P $\delta$-3 | 8.7 | 32.0 | INVALID |

CRACK MOUTH OPENING DISPLACEMENT, $\delta$ ($\times 10^{-3}$ IN)

LOAD (KIPS)
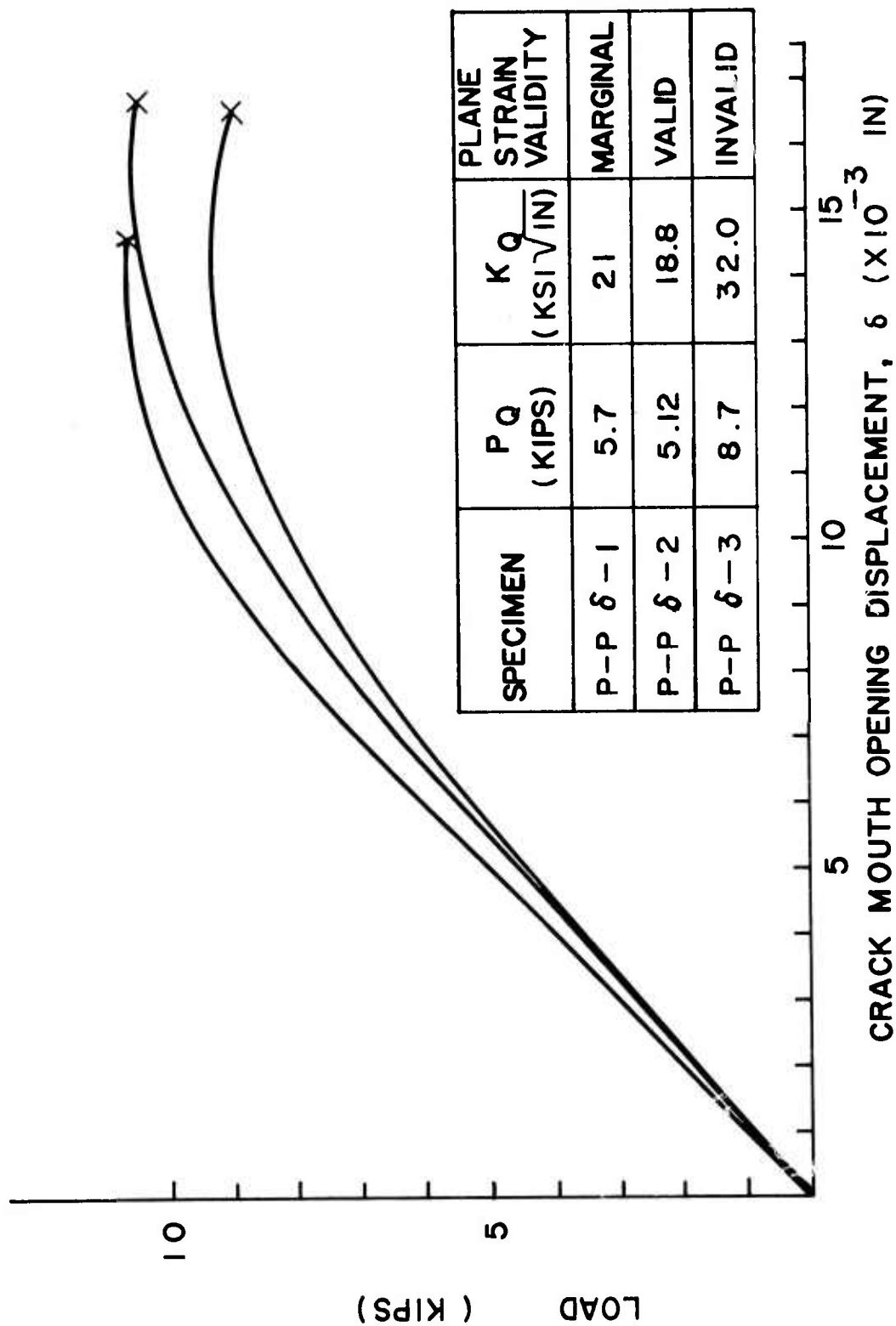
Fig. 4  Load versus Crack Mouth Opening Displacement for Three Compact Specimens
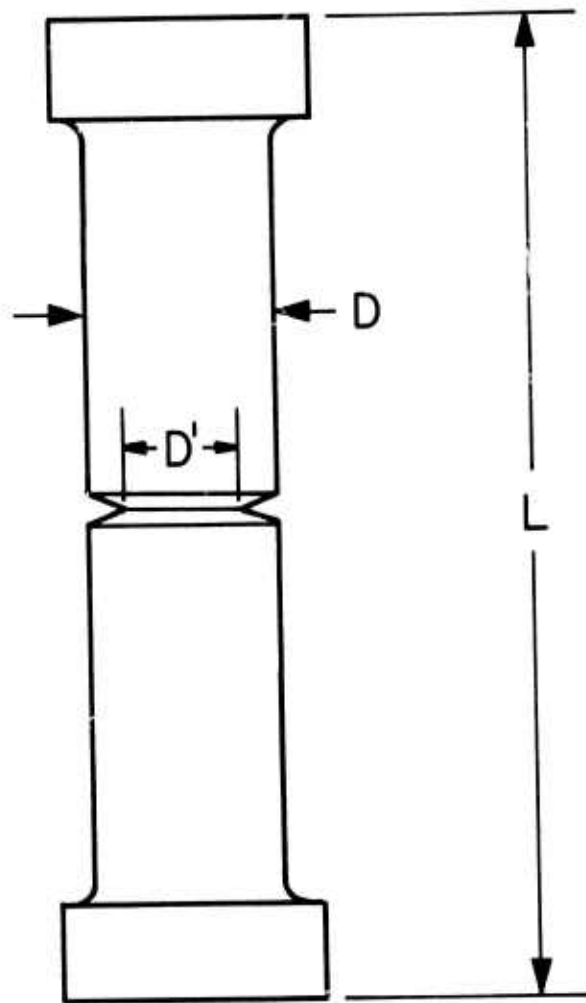
Fig. 5  Circumferential Notch Tension Specimen
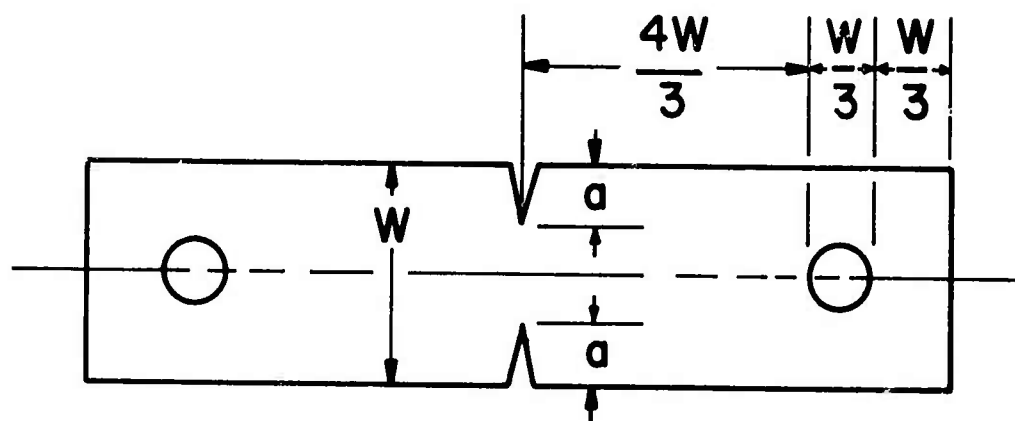
Fig. 6   Double Edge Crack Plate Specimen
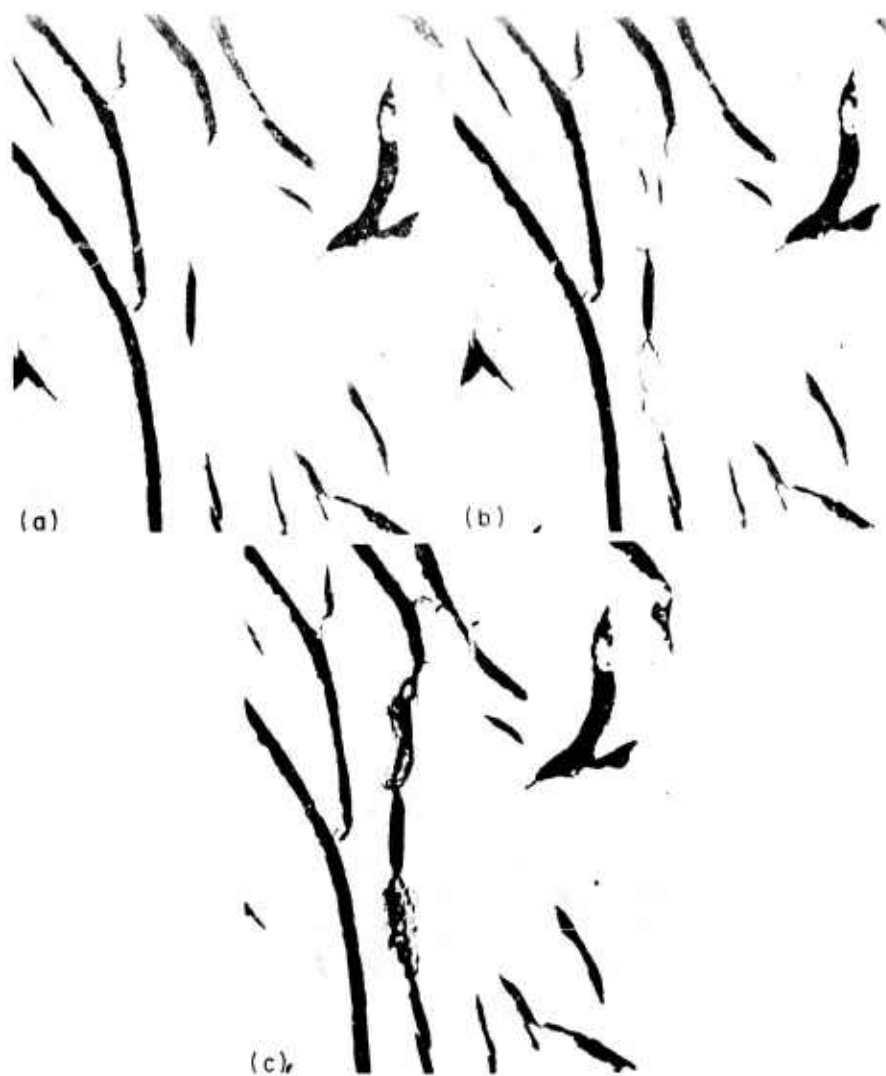
Fig. 7   Apparent Microscale Plastic Action at Graphite Flake Tips
in Gray Cast Iron

        (a) 56% of Fracture Load
        (b) 69% of Fracture Load
        (c) 81% of Fracture Load

(A) REAL MATERIAL

(B) REPRESENTATIVE VOLUME ELEMENT (RVE)

(C) LIMIT CRITERION FOR RVE

(D) LIMIT ANALYSIS FOR MACROSCALE STRUCTURE
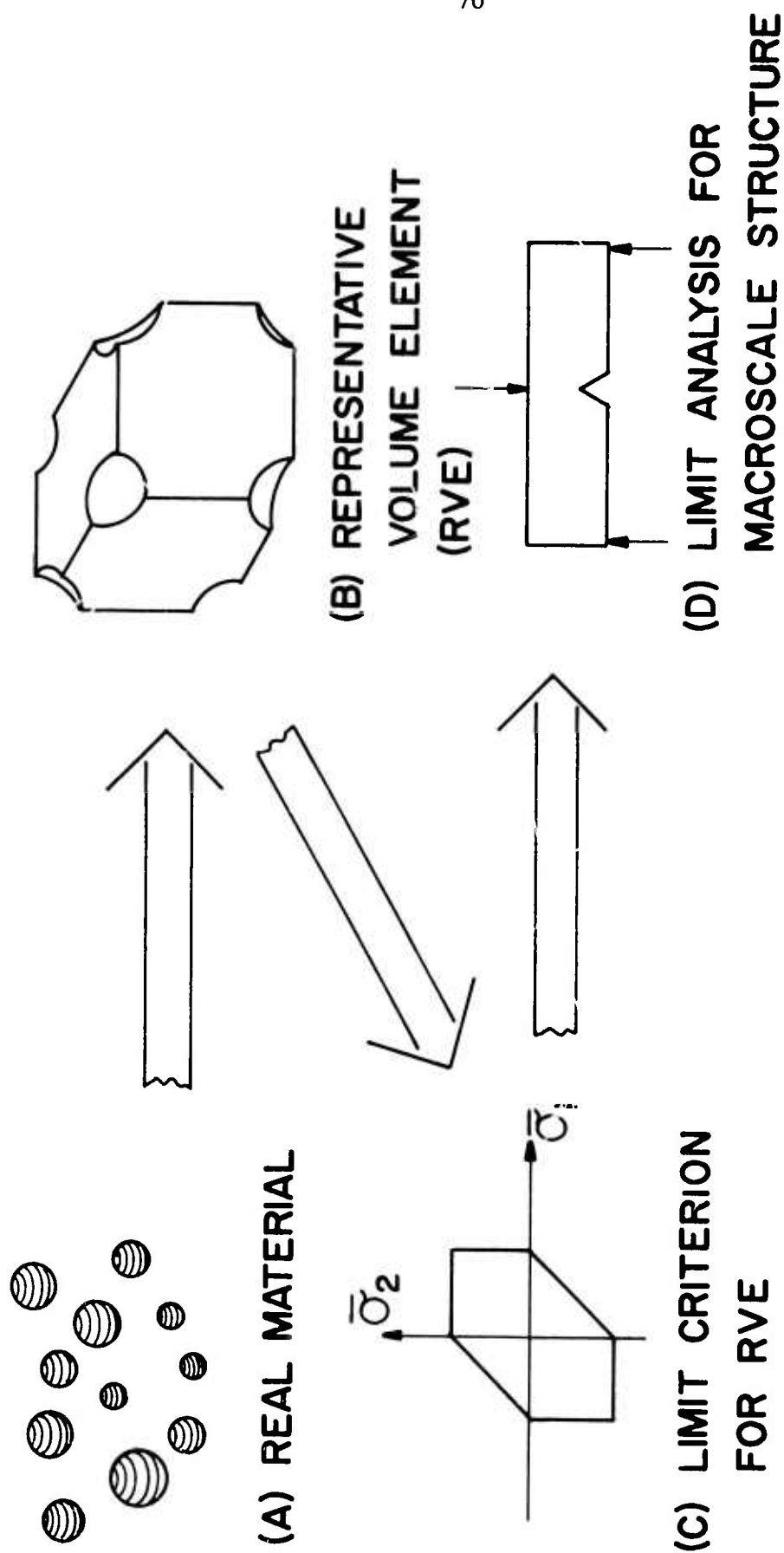
Fig. 8   Schematic of Steps in Proposed Analysis of Microflawed Material Failure
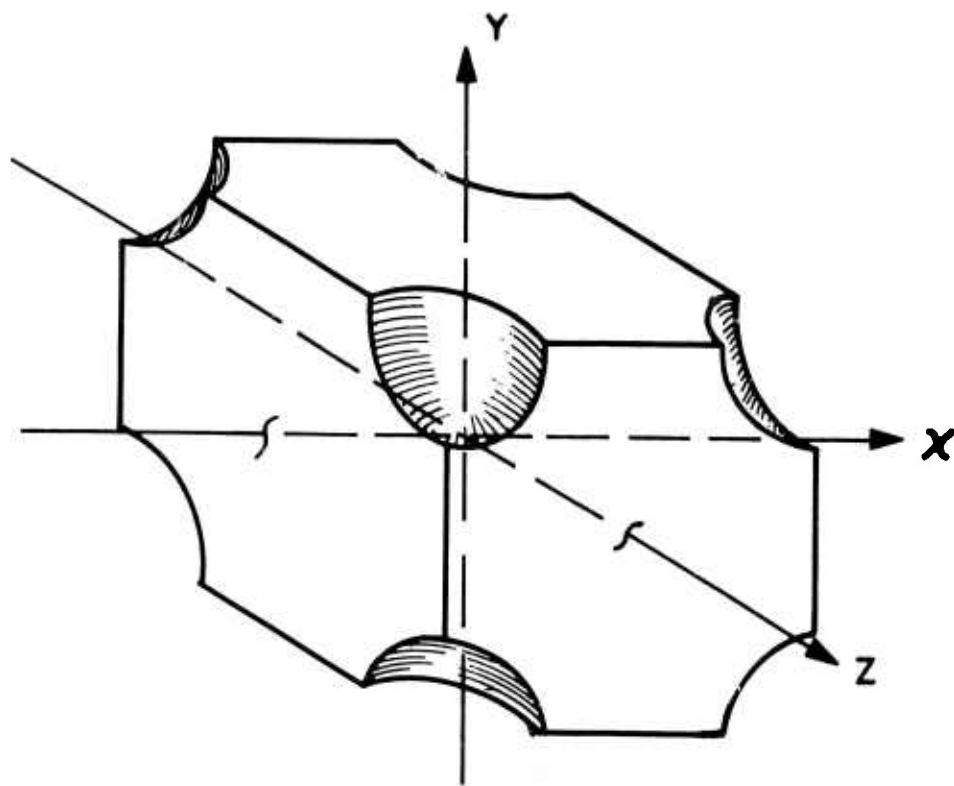
Fig. 9   RVE for Hole Model
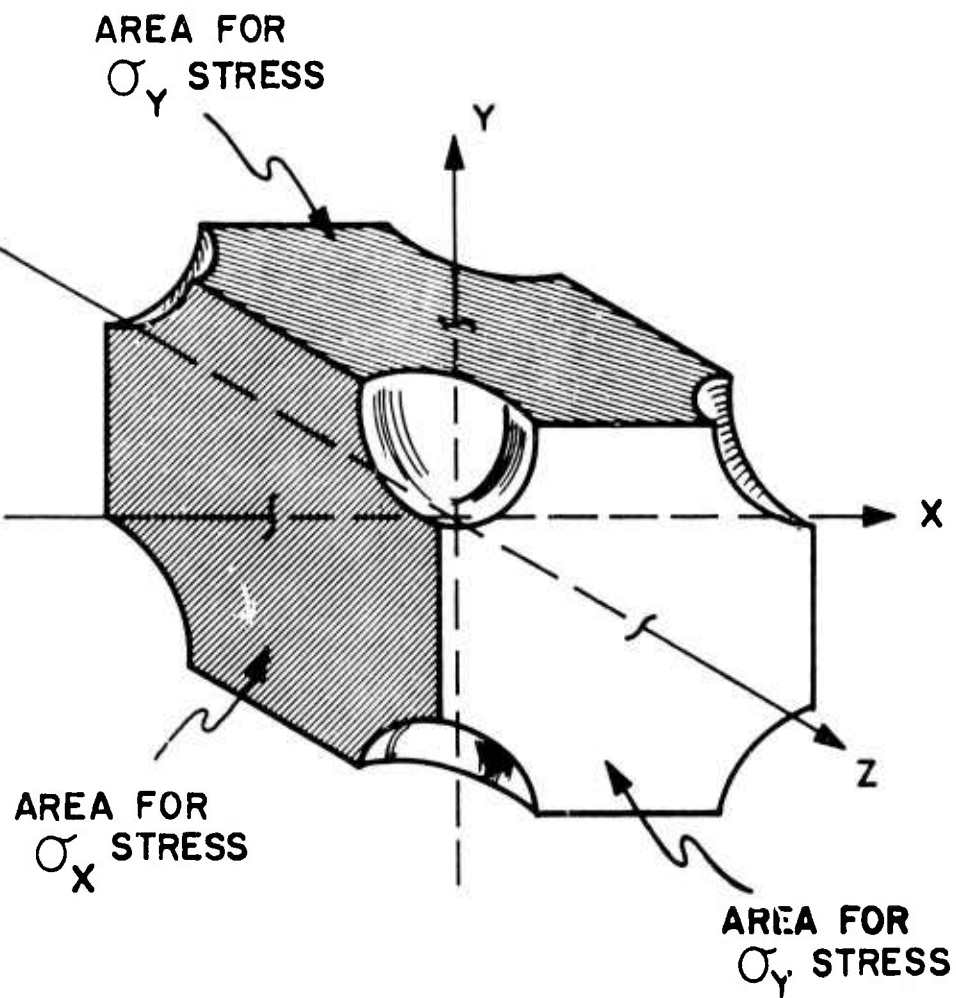
Fig. 10   Assumed Stress Field for Lower Bound of Hole Model
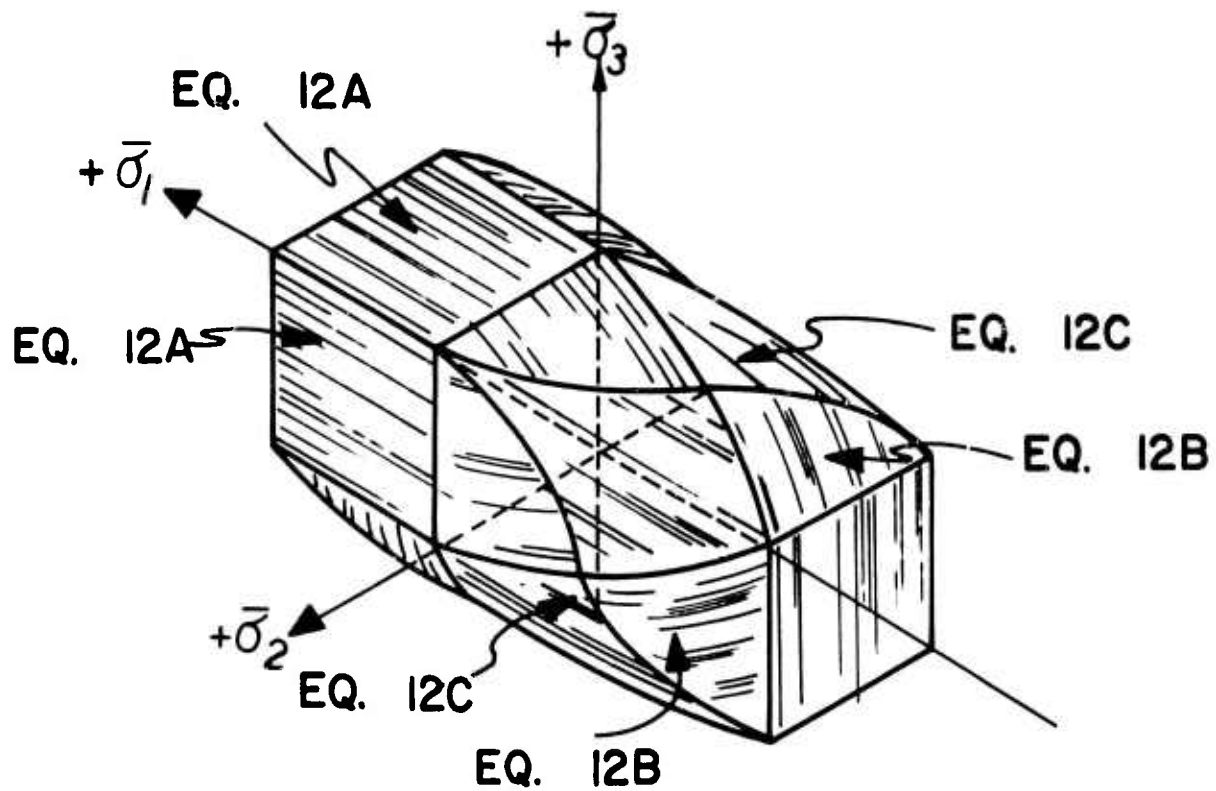
(A) LOWER BOUND FOR HOLE MODEL
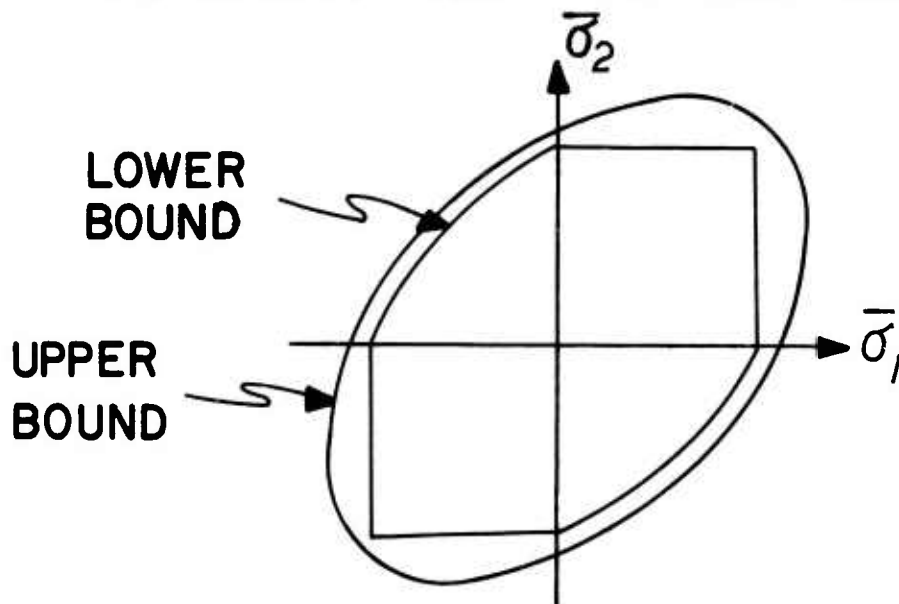
(B) PLANE STRESS LOWER AND UPPER
BOUND SURFACE FOR HOLE MODEL

Fig. 11   Limit Surfaces for RVE of Hole Model
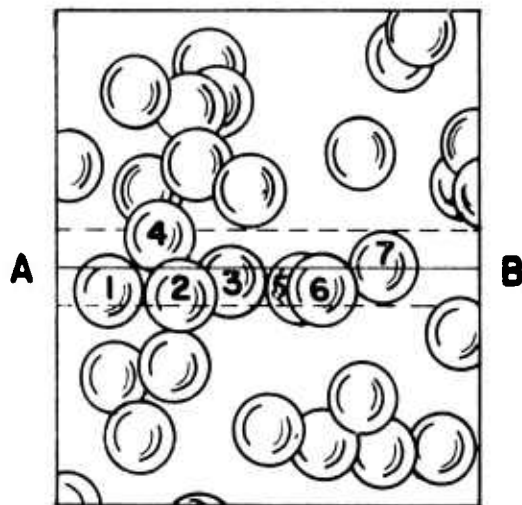
**(A) DISTRIBUTION OF UNIFORM SIZE SPHERES**
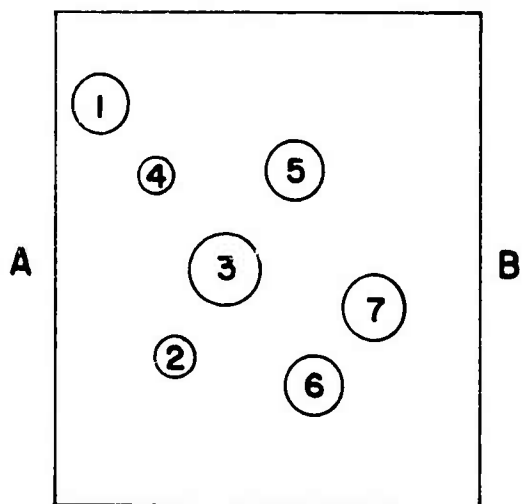
**(B) CROSS SECTIONAL VIEW OF A THREE DIMENSIONAL DISTRIBUTION OF UNIFORM SIZE SPHERES**

Fig. 12    Features of a Distribution of Constant Radius Spheres in a Material

START OF SOLIDIFICATION
AUSTENITE DENDRITES AND
GRAPHITE NUCLEI IN LIQUID
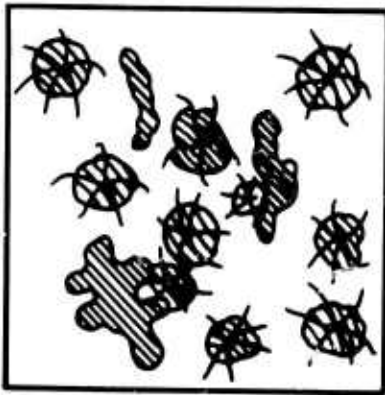
AUSTENITE DENDRITES AND
GROWING EUTECTIC CELLS
OF AUSTENITE AND GRAPHITE
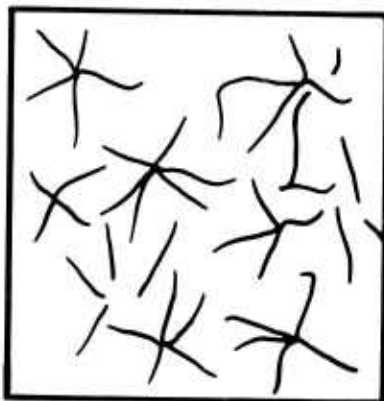
GRAPHITE FLAKES IN MATRIX
OF AUSTENITE

Fig. 13    Schematic of Steps in the Solidification of Gray Cast Iron
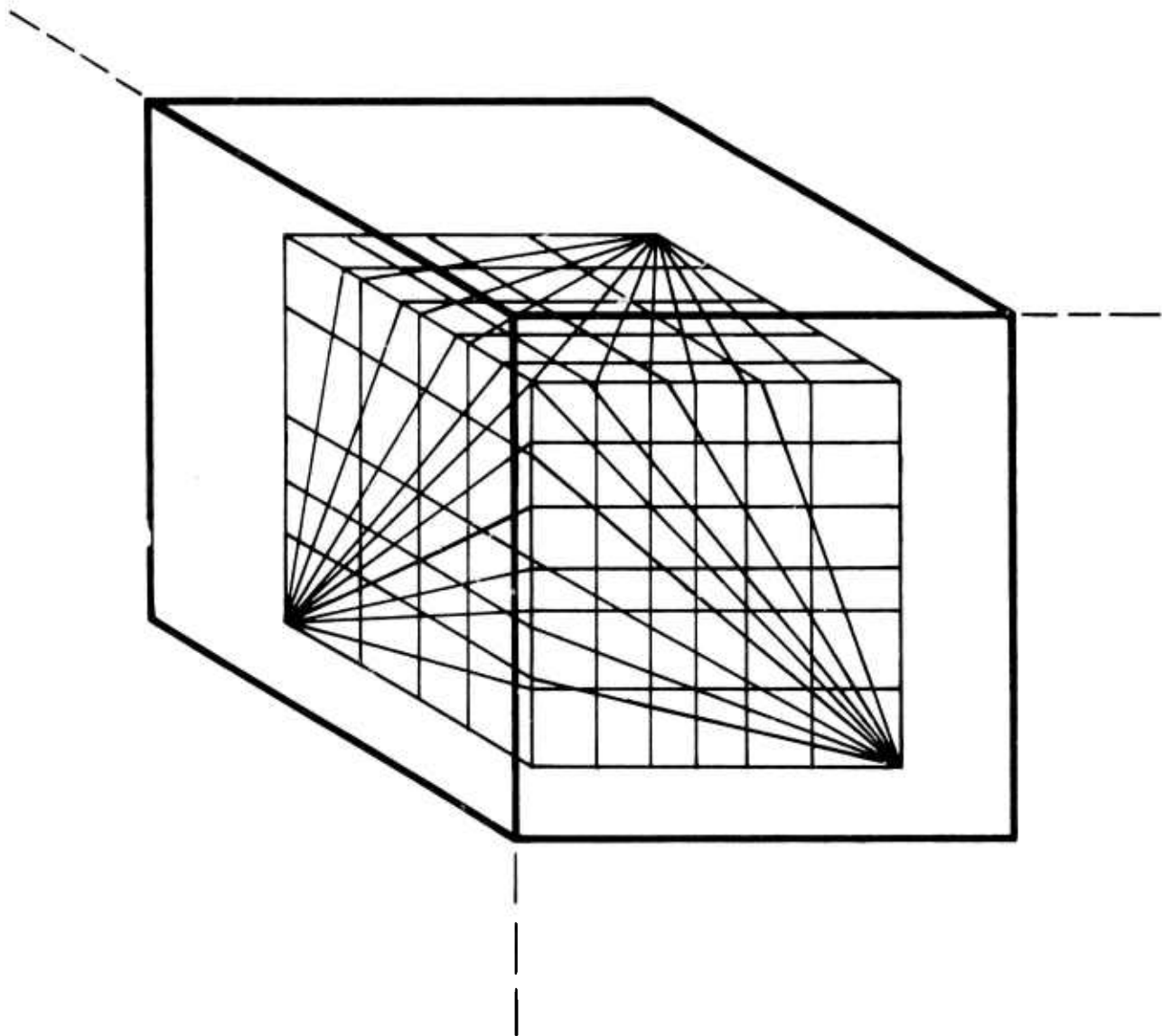
Fig. 14    Sketch of RVE Chosen to Represent Cast Iron
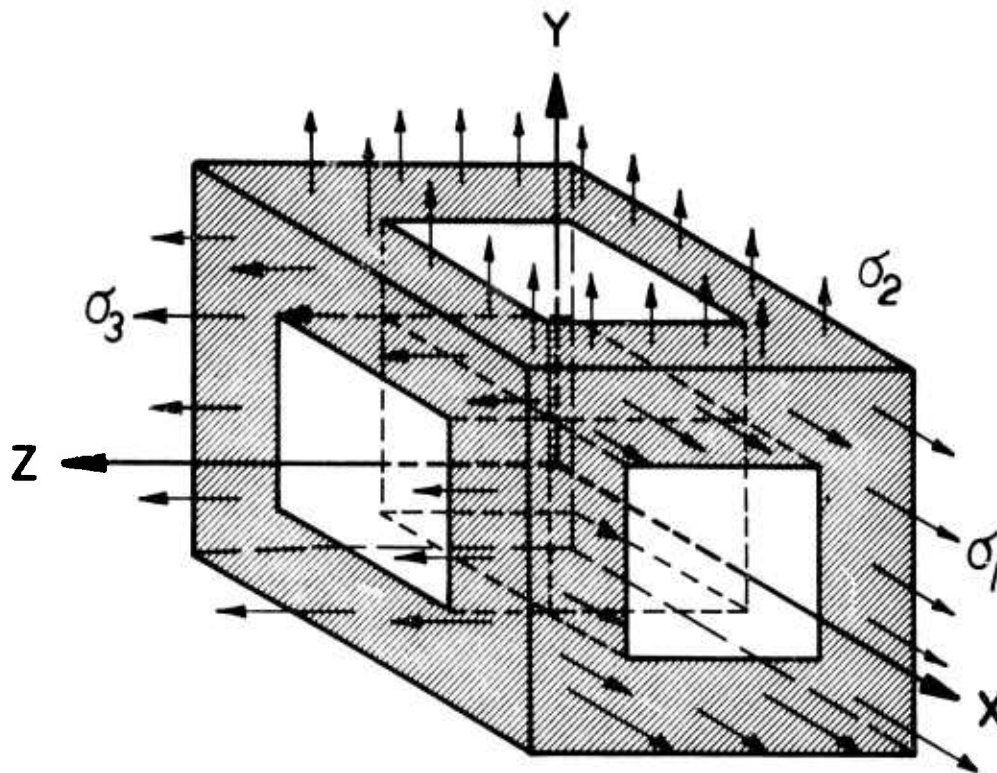
**(A) STRESS FIELD IN THREE DIMENSIONS FOR LOWER BOUND OF SLIT MODEL**
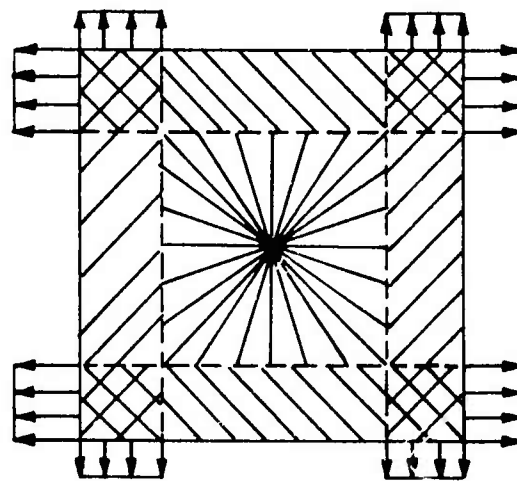


**(B) STRESS FIELD IN TWO DIMENSIONS THRU THE CENTER OF 3-D RVE**

Fig. 15   Assumed Stress Field for Lower Bound of Slit Model
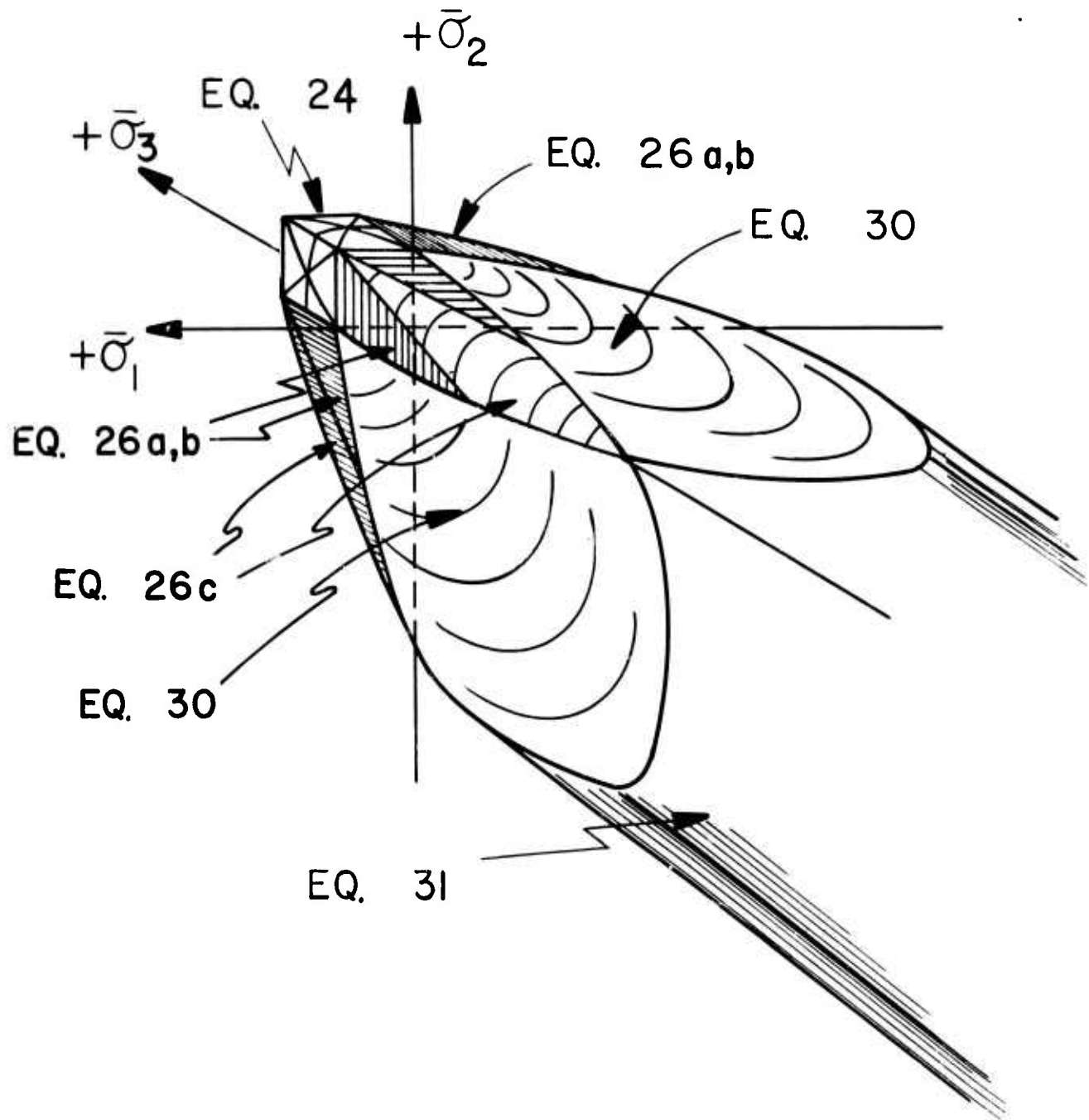
Fig. 16   Lower Bound Limit Surface of RVE of Gray Cast Iron
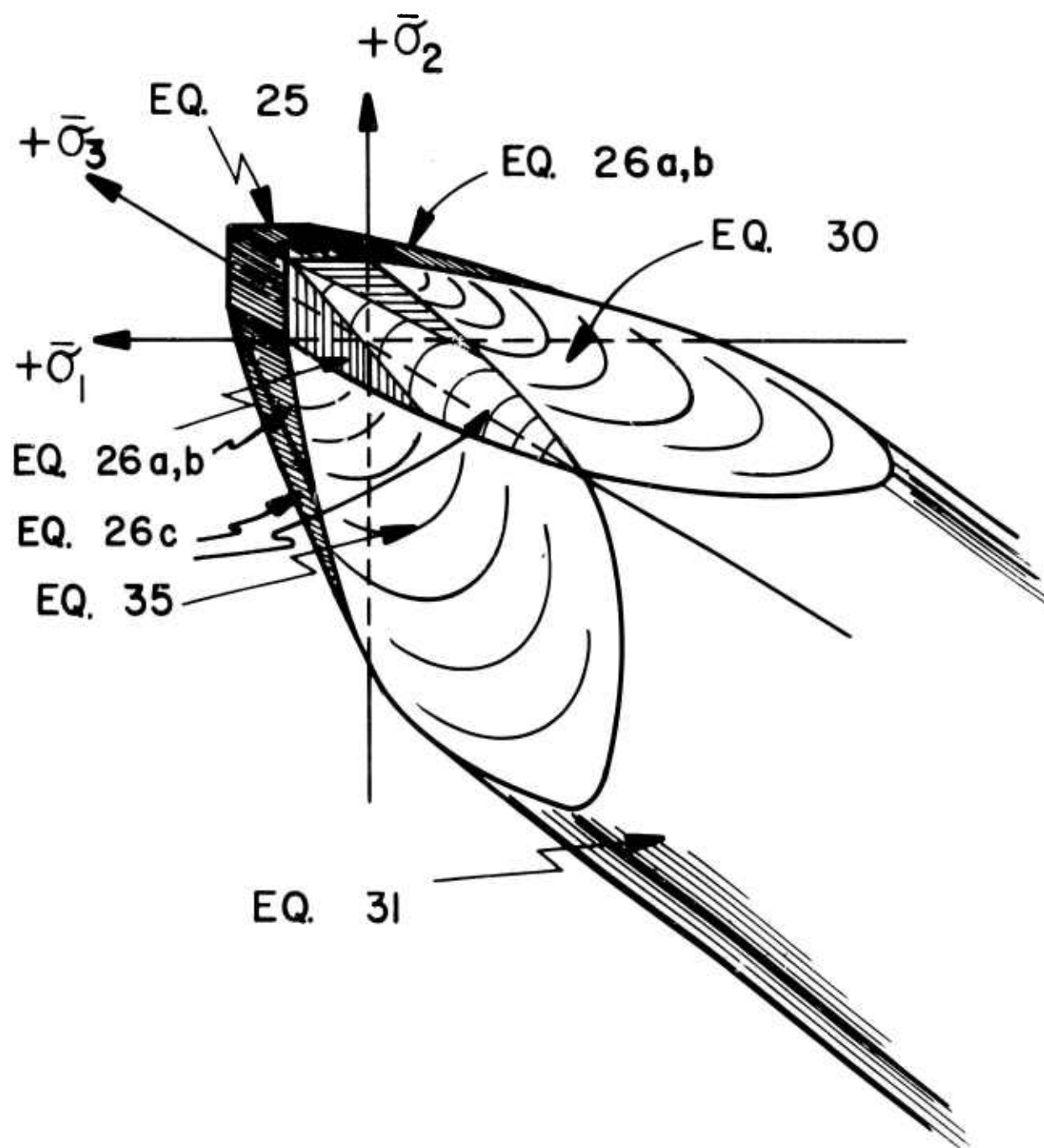
Fig. 17   Lower Bound Limit Surface of RVE  of Nodular Cast Iron

**NORMAL DISPLACEMENT**

**(A) VELOCITY FIELD FOR ROW OF RVE's**

$\overset{o}{\mu}$

1

2

$\overset{o}{\mu}$

**(B) VELOCITY FIELD AT ONE RVE LIGAMENT**

$\frac{1}{2}\left(1+\frac{\ell}{\sqrt{2}}\right)$

**(C) LENGTH FOR USE IN DISSIPATION (MULTIPLY BY 4)**
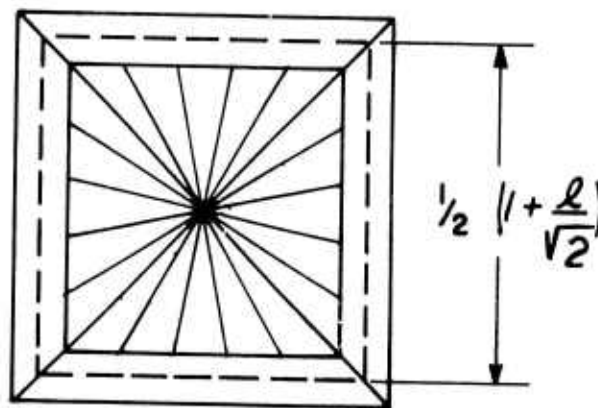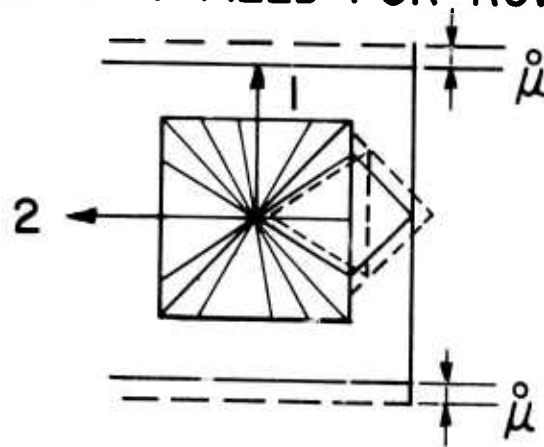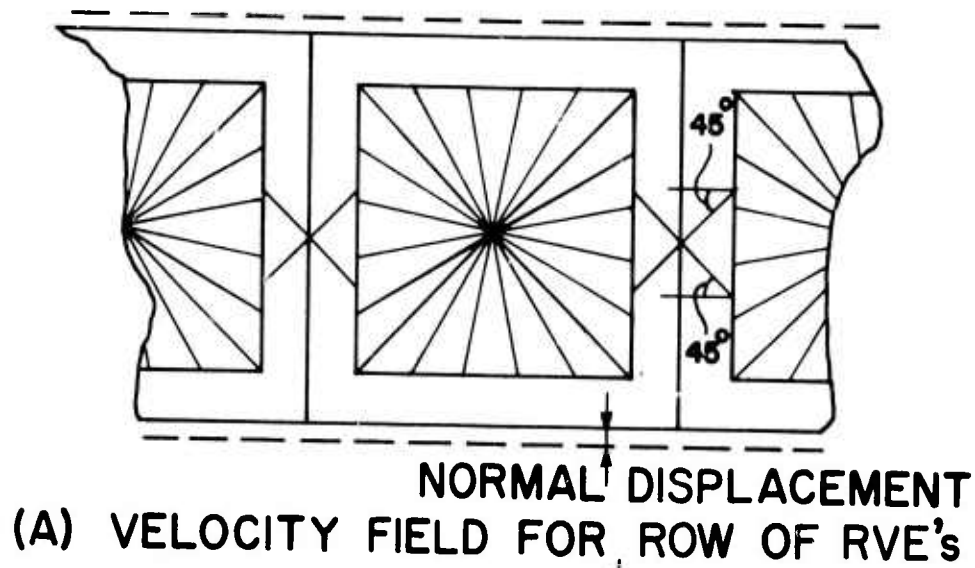
Fig. 18   Upper Bound Displacement Field for Slit Model
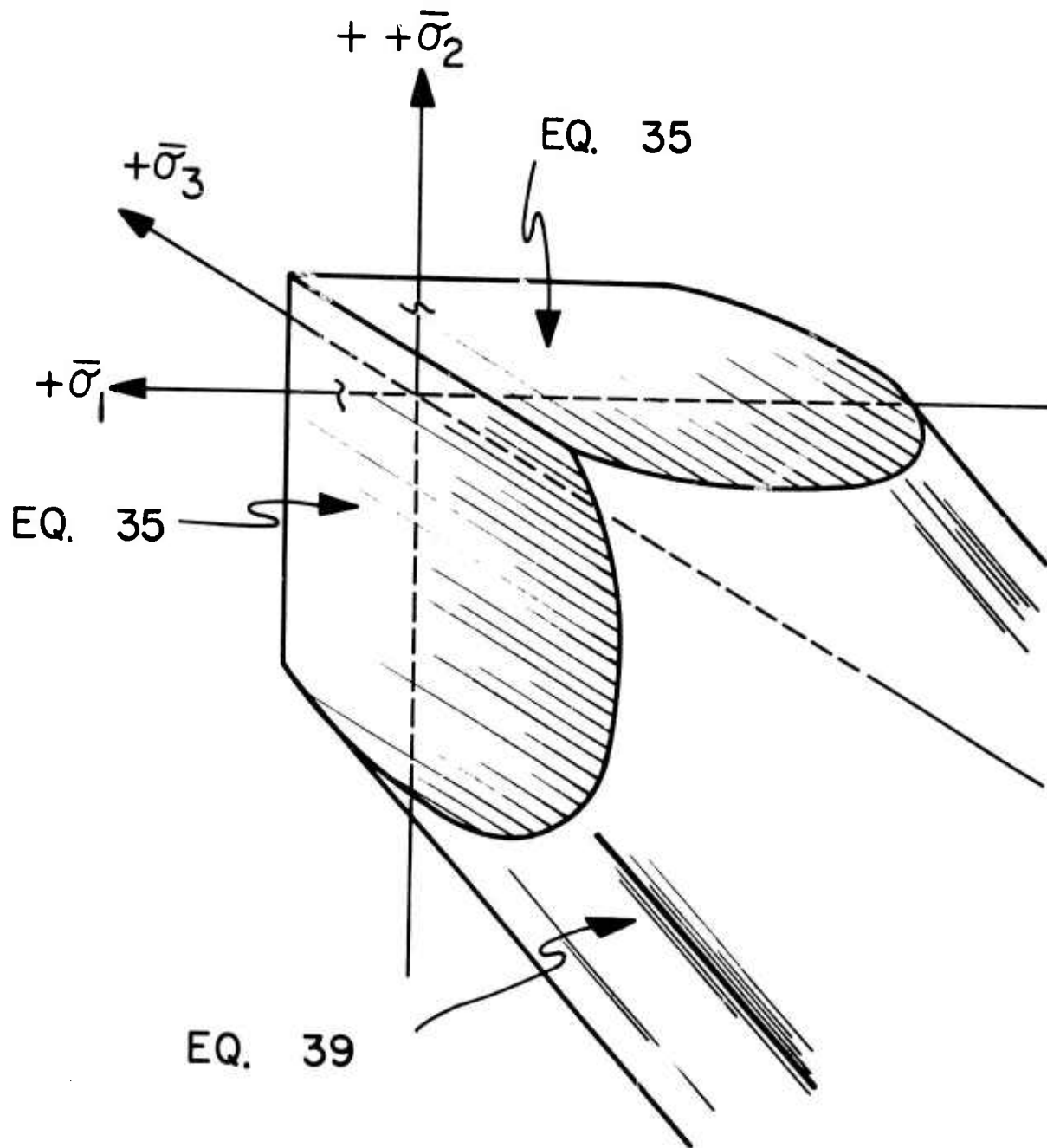
Fig. 19 Upper Bound Limit Surface for RVE of Gray Cast Iron
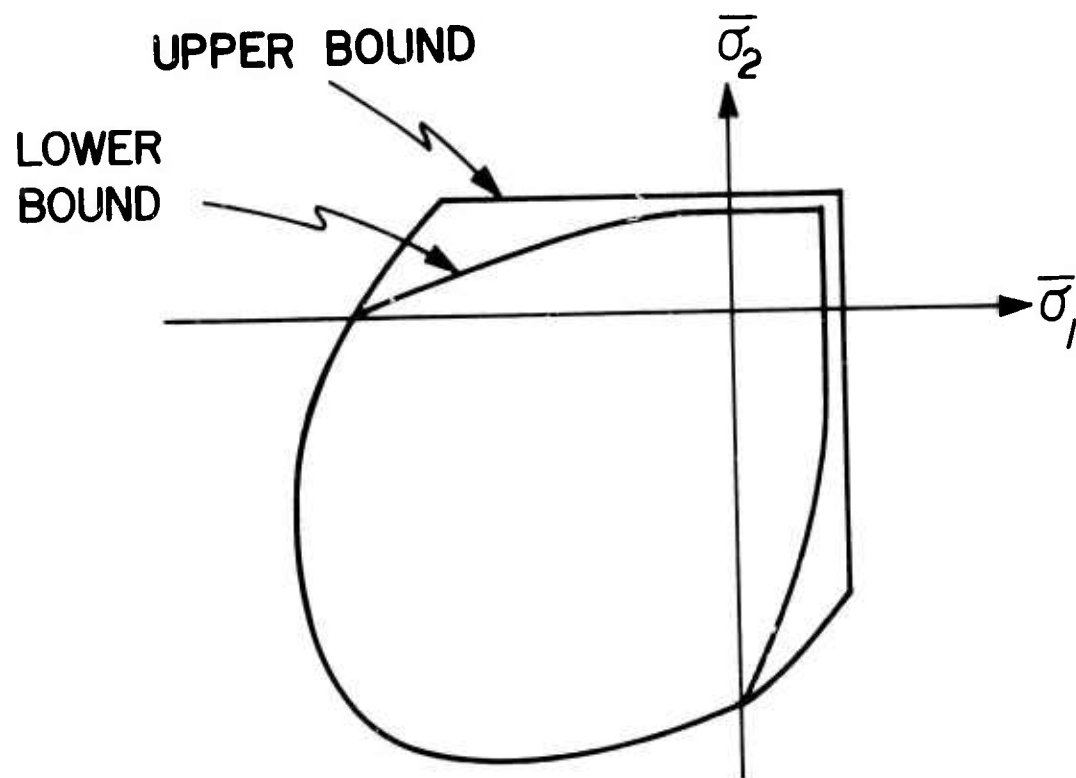
Fig. 20   Upper and Lower Bounds of Gray Cast Iron RVE in Plane Stress

83
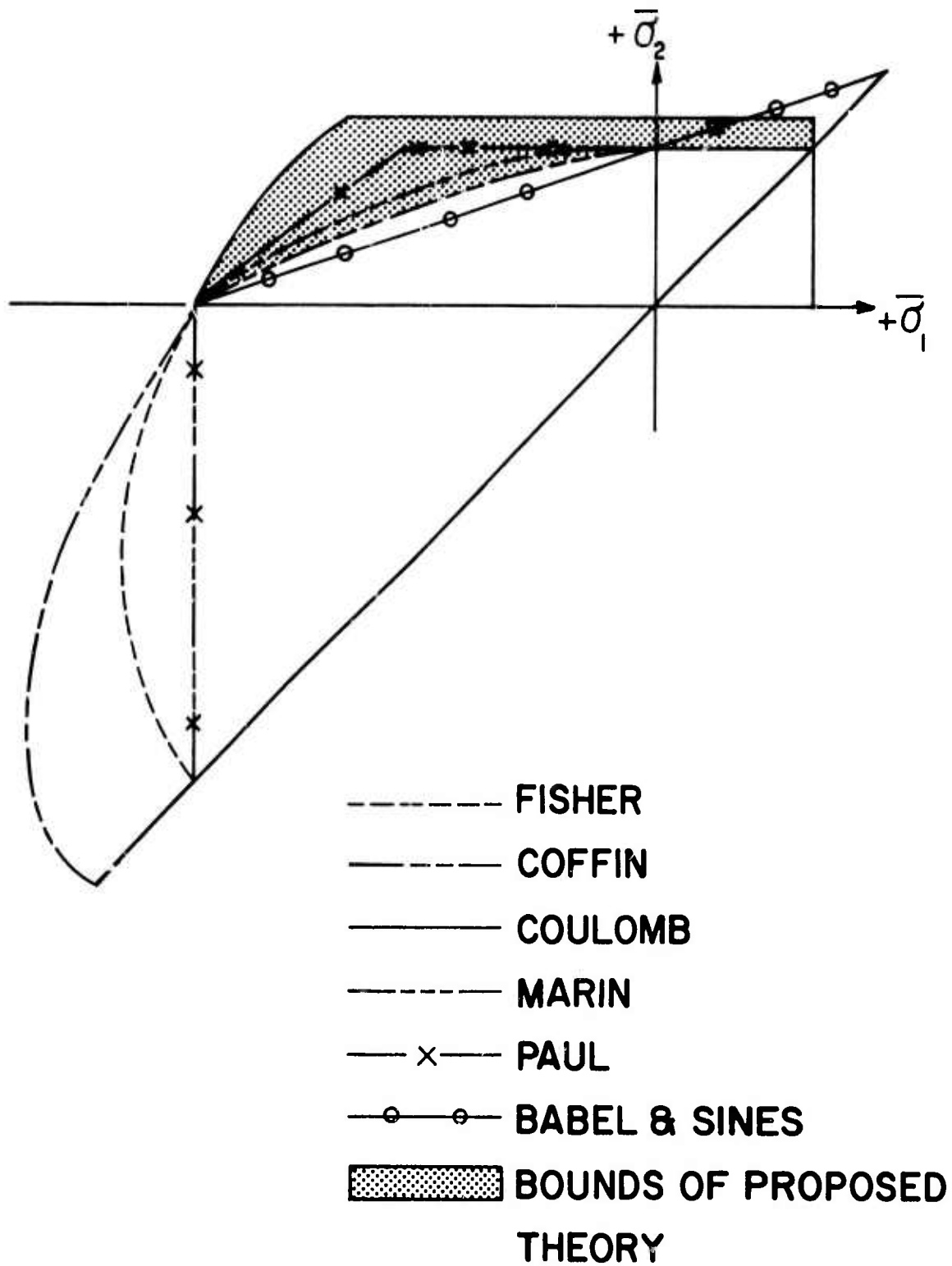


Fig. 21   Plane Stress Failure Surfaces of Currently Available
Failure Theories for Microflawed Materials
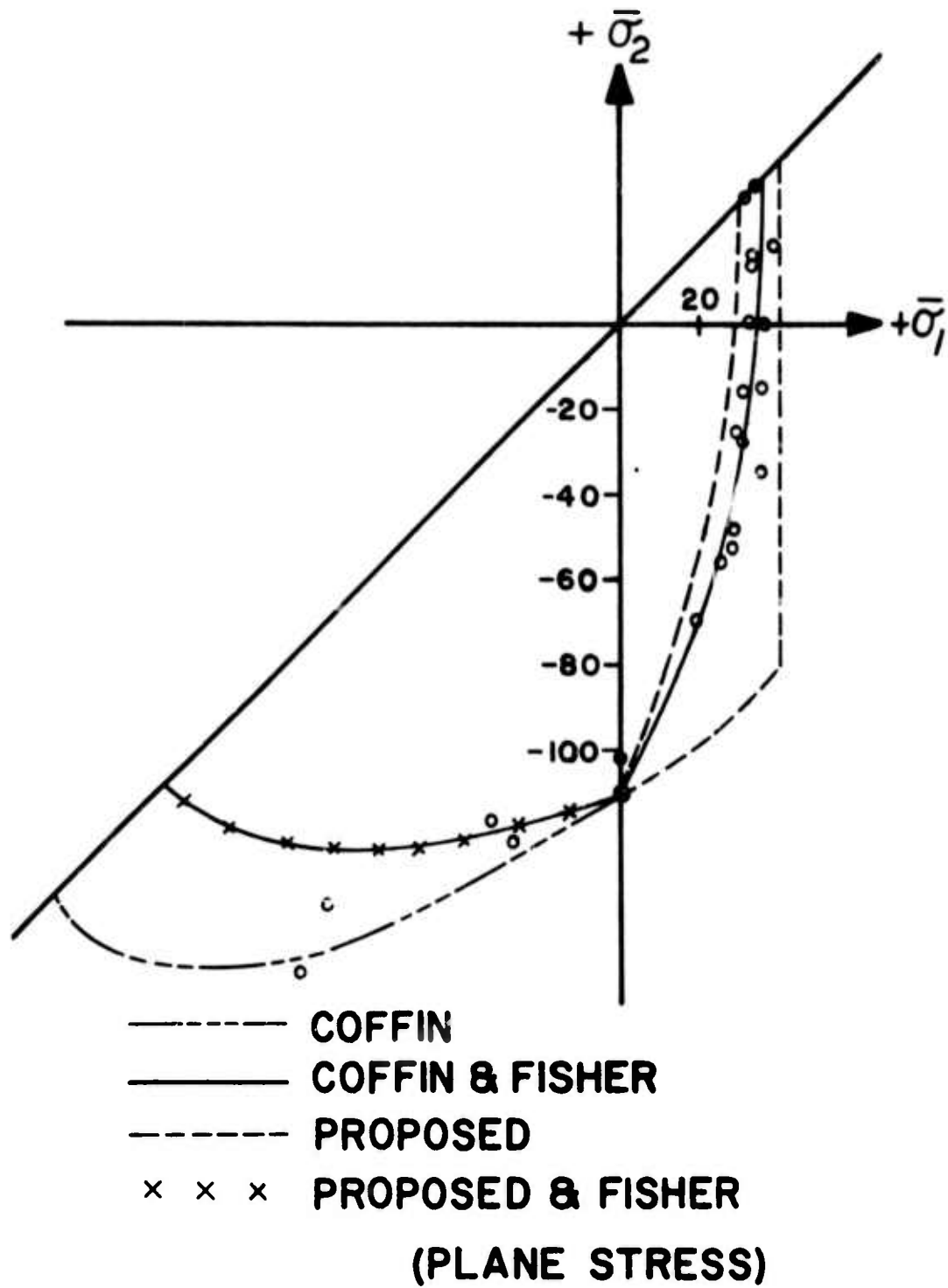
Fig. 23  Experimental Fracture Data from Gray Cast
Iron Study of Coffin
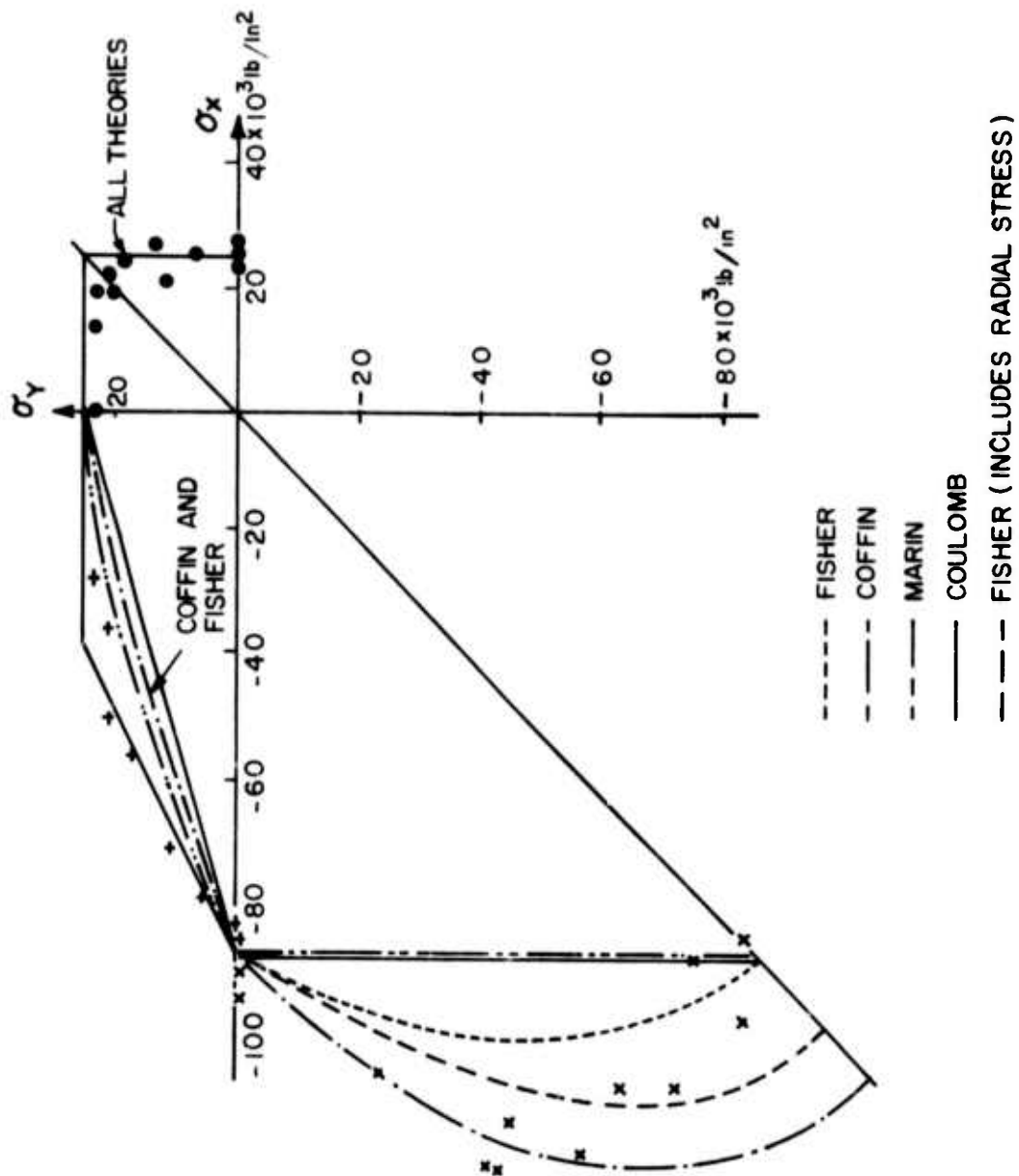
Fig. 24  Experimental Fracture Data on Gray Cast Iron from Mair
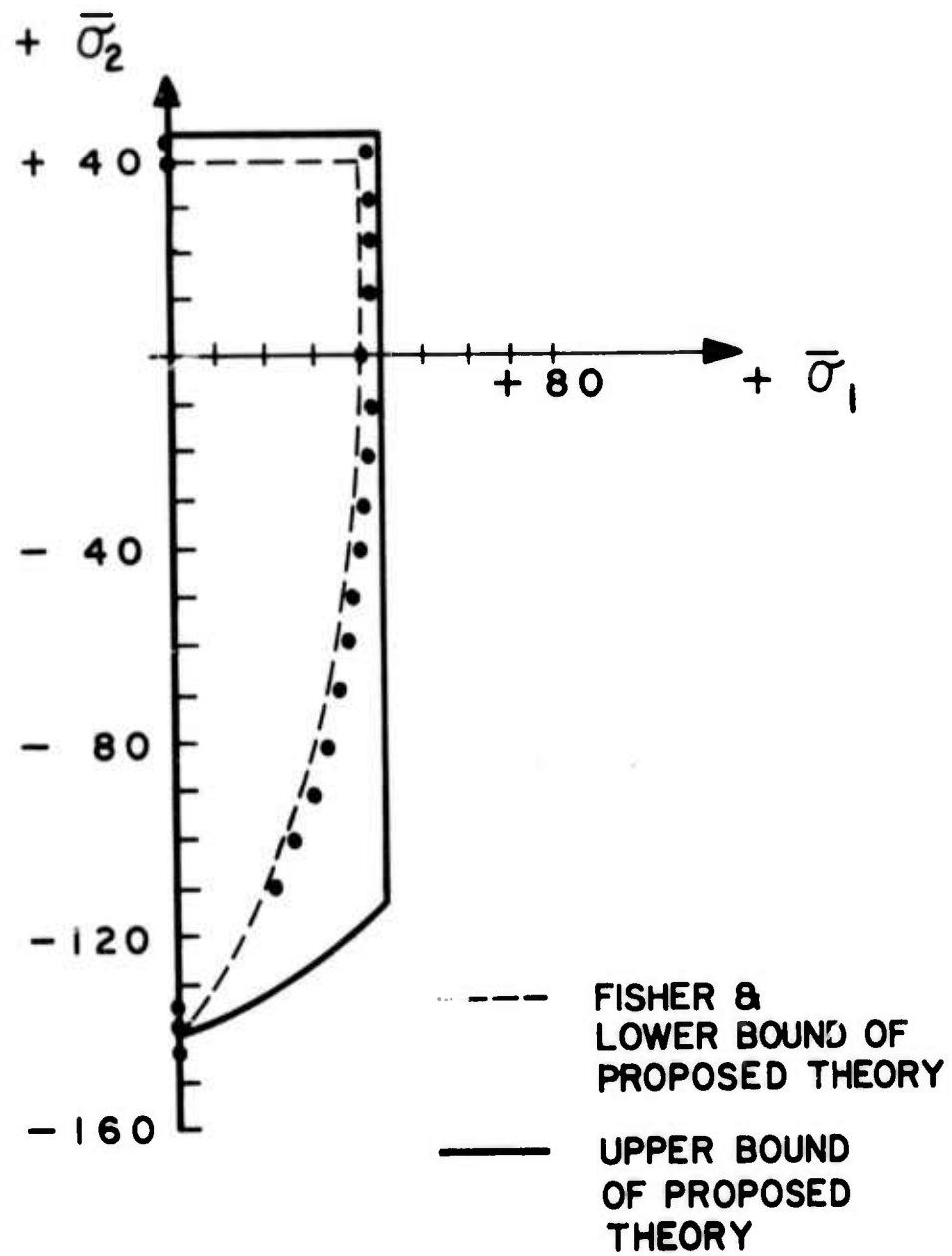
Fig. 25   Experimental Fracture Data on Gray Iron from
Clough and Shank
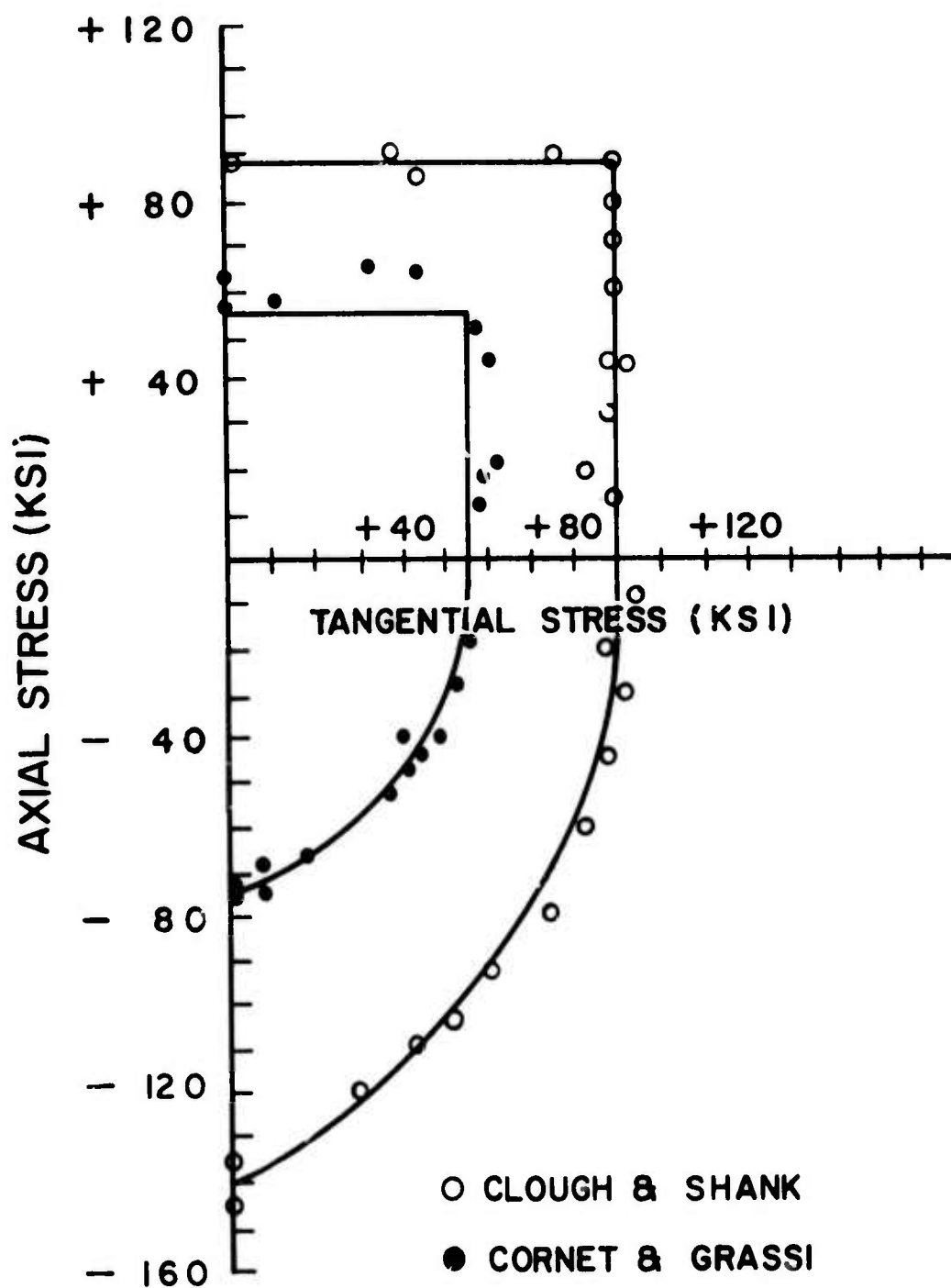
Fig. 26 Experimental Fracture Data on Nodular Iron from Cornet and Grassi, and Clough and Shank
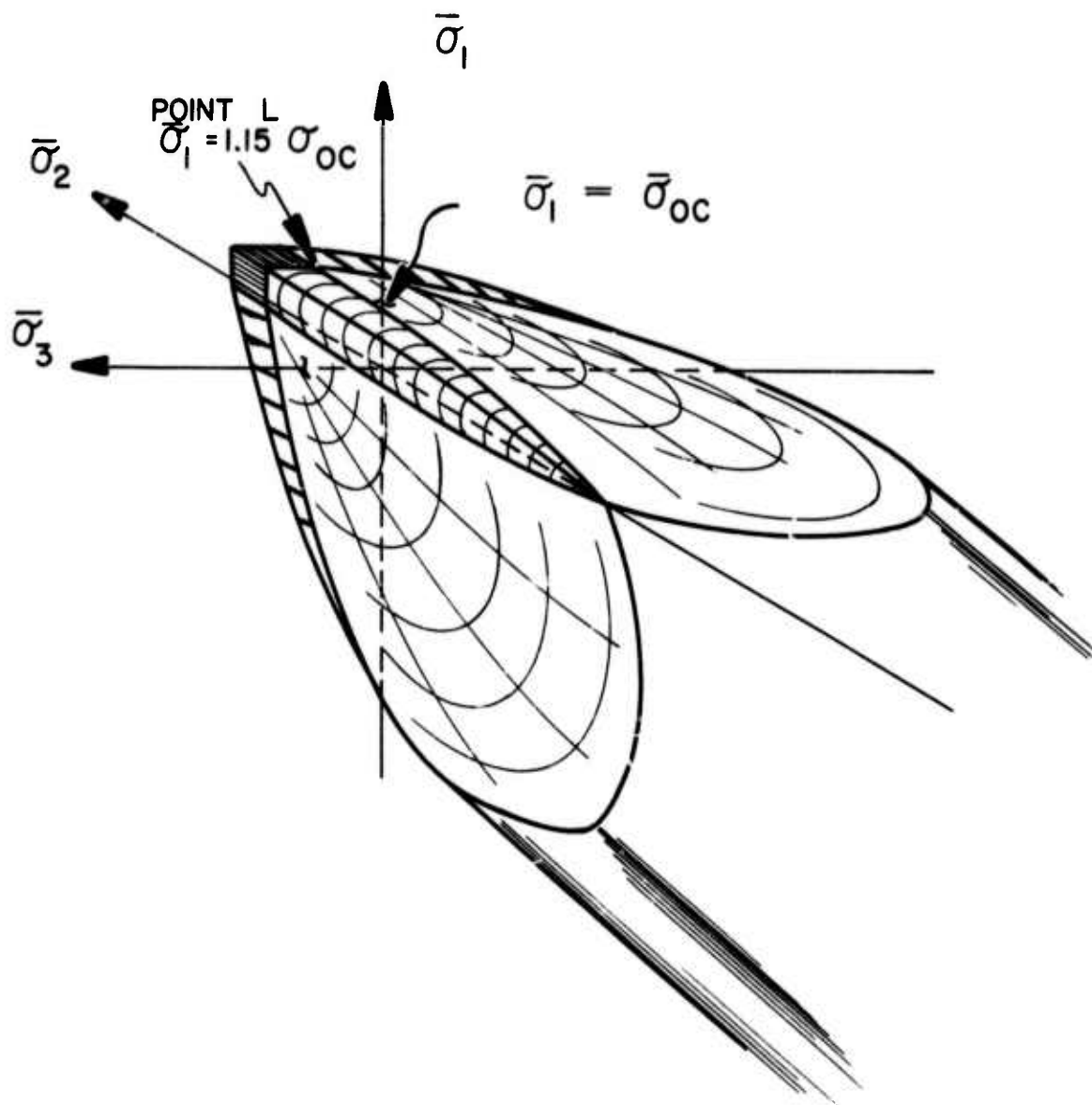
Fig. 27   Estimated Single Limit Surface for Gray Cast Iron
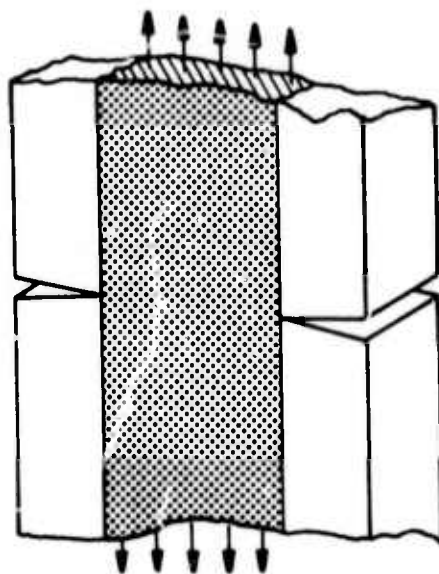
**(A) STRESS FIELD FOR LOWER BOUND OF DEC SPECIMEN**
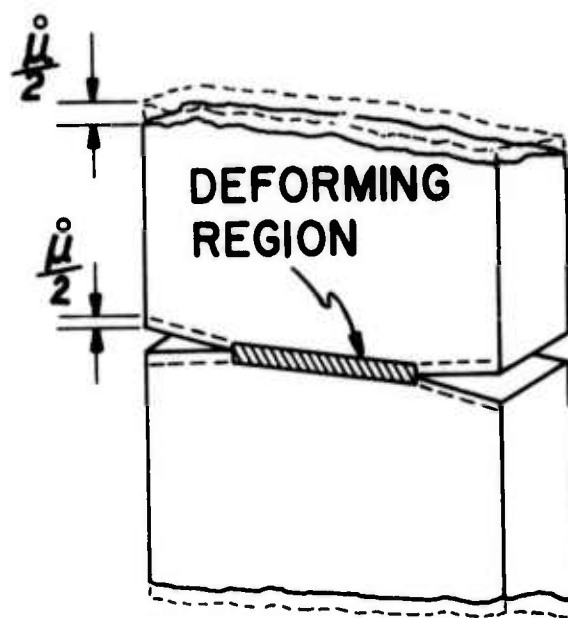


**(B) VELOCITY FIELD OF UPPER BOUND**

Fig. 28    Assumed Stress and Velocity Fields for
Limit Analysis of Double Edge Crack Plate
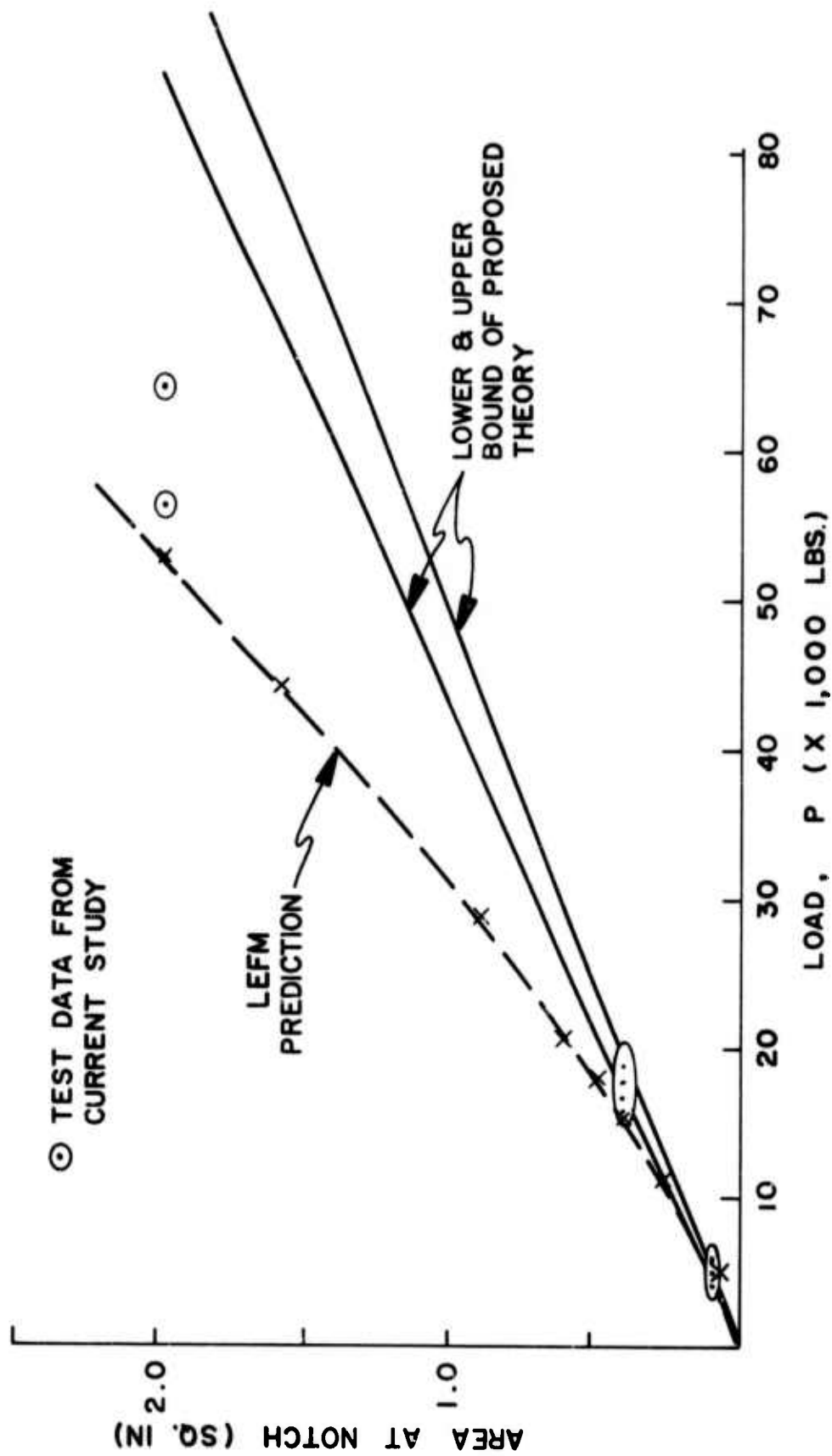
Fig. 29   Notch Area versus Failure Load for Circumferential Notch Tensile Bars
Showing LEFM and Proposed Theory Predictions

92
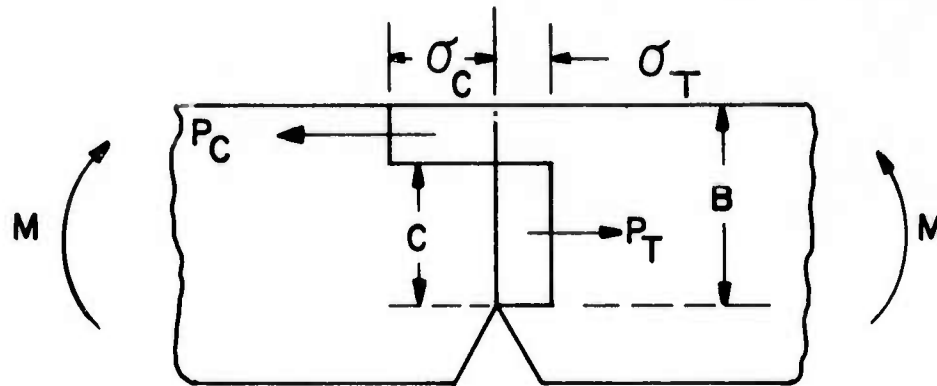


(A) ASSUMED STRESS FIELD FOR LOWER
    BOUND OF 3PB SPECIMEN
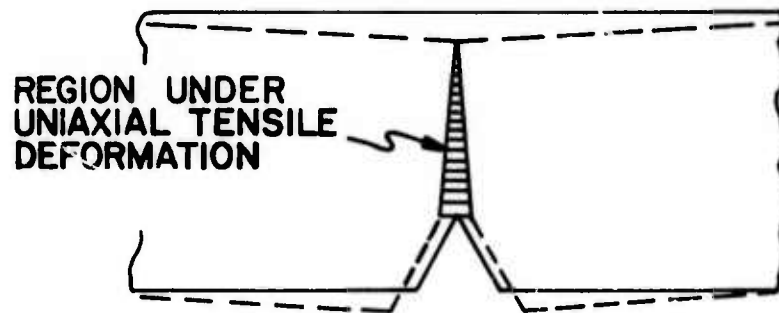


(B) ASSUMED VELOCITY FIELD FOR UPPER
    BOUND OF 3PB SPECIMEN

Fig. 30   Stress Field and Velocity Field Assumed for Limit
         Analysis of a Notched Three Point Bend Beam

93
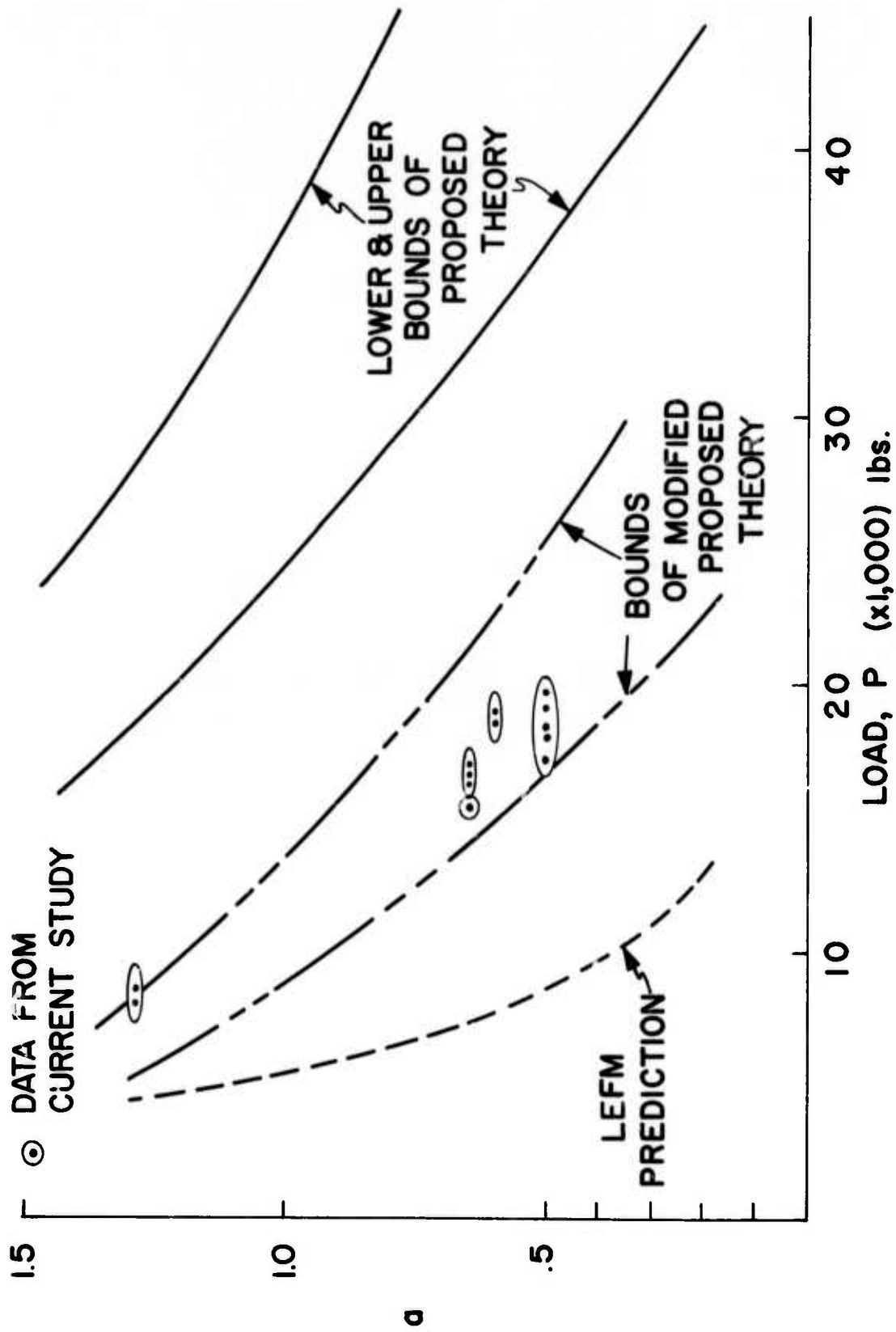


Fig. 31  Crack Length versus Failure Load for Three Point Bend Tests
Showing LEFM and Proposed Theory Predictions

## APPENDIX A

## FUNDAMENTALS OF LINEAR ELASTIC FRACTURE MECHANICS

The fundamental concept in linear elastic fracture mechanics is to focus attention on the material in the vicinity of a crack tip because the material behavior here determines the material's resistance to fracture. It can be shown that the elastic stress distribution at the tip of a crack can be written as (42)

$$\sigma_x = \left( \frac{K}{2 \pi r'} \right)^{1/2} f(\theta) \tag{A1}$$

$$\sigma_y = \left( \frac{K}{2 \pi r'} \right)^{1/2} f(\theta) \tag{A2}$$

$$\sigma_z = \nu(\sigma_x + \sigma_y) \tag{A3}$$

for the plane strain case. For plane stress,

$$\sigma_z = 0 \tag{A4}$$

In the above equation, $r'$ is the radial distance from the crack tip to the point of interest, $\theta$ is the angle from the crack plane as shown in Fig. A1. The directions x, y, and z are also shown in Fig. A1. $\nu$ is Poisson's ratio, and K is called the stress intensity factor. The K and $f(\theta)$ values depend on the direction of relative motion of the crack surfaces. If the crack surfaces open normal to each other as shown in Fig. A2, mode 1 crack displacement has occurred. In this case, K is given a subscript 1. $K_I$ is called the mode I stress intensity factor. Also for mode I, $f(\theta)$ becomes

$$f(\theta) = \cos \frac{\theta}{2} \left[ 1 \pm \sin \frac{\theta}{2} \sin \frac{3\theta}{2} \right] \tag{A5}$$

Restricting attention to the plane crack, $\theta = 0°$ gives

$$f(\theta) = 1 \tag{A6}$$

Equations A1 and A2 now become

$$\sigma_x = \frac{K_I}{(2 \pi r')^{1/2}} \tag{A7}$$

and

$$\sigma_y = \frac{K_I}{(2 \pi r')^{1/2}} \tag{A8}$$

for mode I crack surface displacement.

From dimensional considerations of Eqs. A1 and A2 or A7 and A8, the units of the stress intensity factor must be pounds per square inch multiplied by square root of inches assuming that $\sigma_x$ and $\sigma_y$ are in pounds per square inch and r' is in inches. In a given piece of material containing a crack, the most readily measured parameters are the gross stress, $\sigma_g$, that is, stress determined as if the crack were not present, and the crack length, a. Thus, the easiest representation for the stress intensity factor is

$$K = \alpha \, \sigma_g \sqrt{a} \tag{A9}$$

where $\alpha$ is a geometry factor depending on mode of crack opening and the loading geometry for the specimen or part. It can also be shown from elasticity theory that the form of the stress intensity factor in the general case is as written in Eq. A9.

If a fixed geometry and crack size is chosen, $\alpha$ and a become fixed in Eq. A9. The maximum gross stress that this material can carry is called the critical stress, $\sigma_c$. The corresponding stress intensity is called the critical stress intensity, $K_c$. $K_c$ is a function of material thickness as indicated in Fig. A3. Above some thickness, $K_c$ is relatively constant. This constant is called the plane strain fracture toughness, $K_{1c}$. Fracture toughness is a measure of the material's resistance to fracture or rapid crack propagation.

It is generally accepted that $K_{Ic}$ is a material property and is independent of the geometry of loading or the geometry of the crack. Therefore, with the appropriate $\alpha$ and a value in Eq. A9 and using $K_{Ic}$, the failure stress for any loading geometry can be obtained. Again, this can be done only if the part being evaluated is of sufficient thickness.

Strictly speaking, linear elastic fracture mechanics is not applicable in cases where plastic zones appear at the tip of a crack prior to rapid crack advance. However, it has been found that small amounts of plastic action can be accounted for by artificially extending the actual crack by some amount. This amount is called the plastic zone correction, $r_y$, where, for plane strain

$$r_y = \frac{1}{6\pi} \left( \frac{K}{\sigma_{ys}} \right)^2 \tag{A10}$$

In this equation $\sigma_{ys}$ is the material's uniaxial yield stress. The $r_y$ value is utilized in K calculations by replacing the crack length a by $a + r_y$. This leads to an equation involving K on the left side and K on the right side as indicated below with $K_{Ic}$ substituted for K.

$$K_{Ic} = \alpha \, \sigma_c \left[ a + \frac{1}{6\pi} \left( \frac{K}{\sigma_{ys}} \right)^2 \right]^{1/2} \tag{A11}$$

Utilization of this equation requires that one guess at a $K_{Ic}$ value to use on the right side, calculate the $K_{Ic}$ on the left side, then readjust the $K_{Ic}$ on the right until both $K_{Ic}$ values are equal.
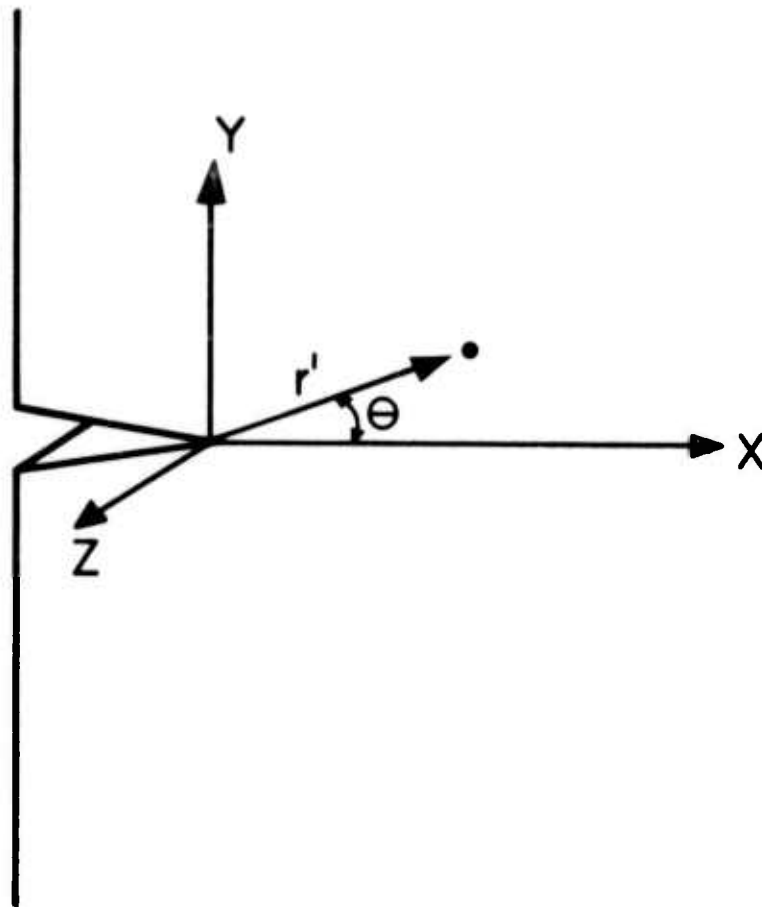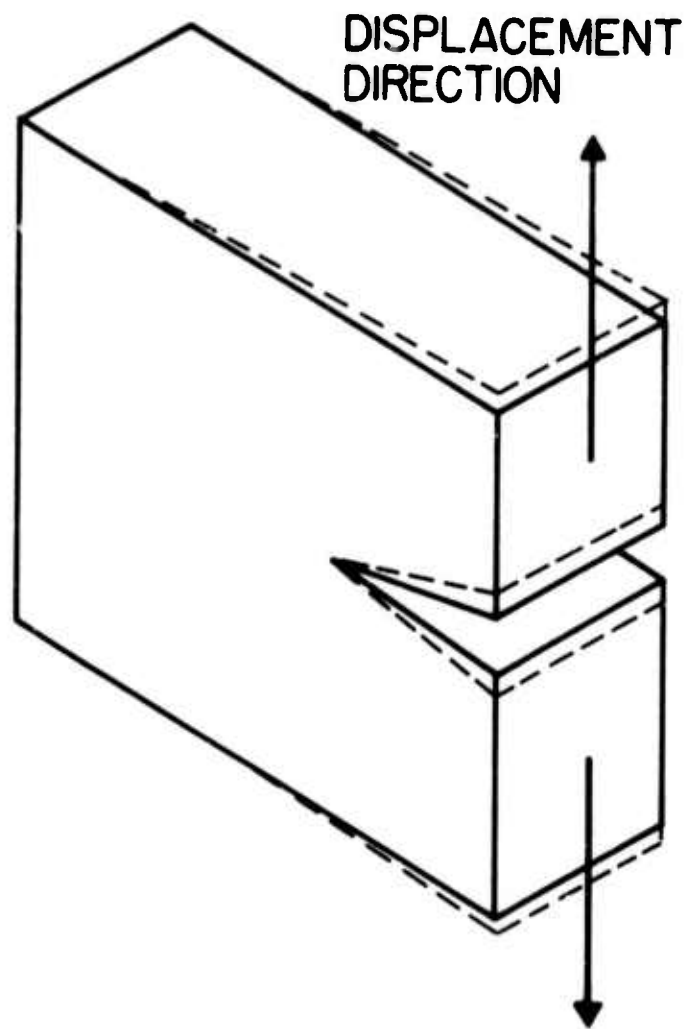
Fig. A1   Coordinate System at the Tip of a Crack
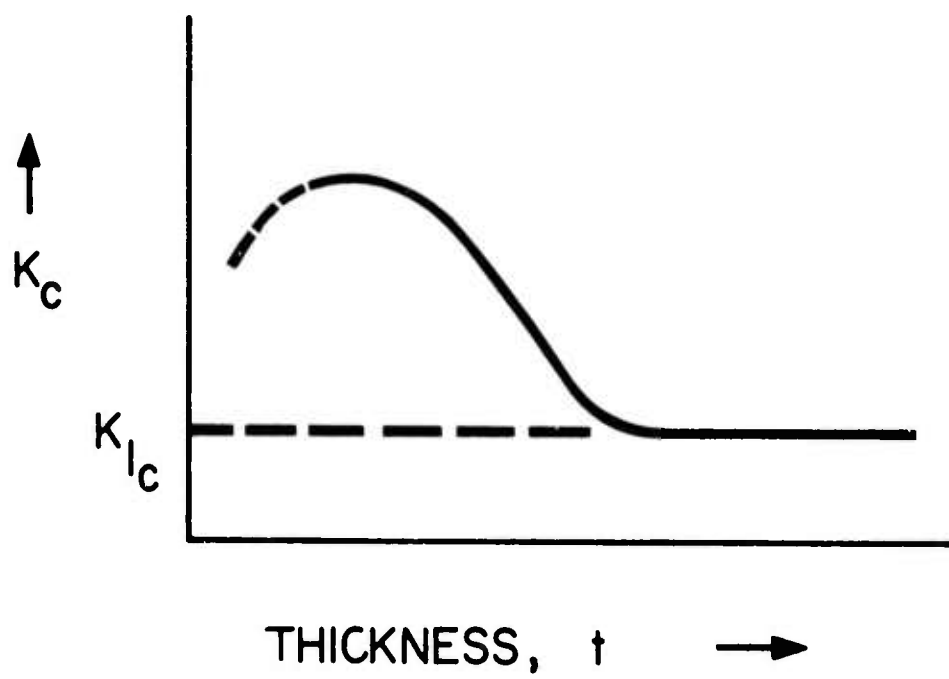
Fig. A2   Mode I Crack Opening Displacement

Fig. A3  Critical Stress Intensity versus Thickness

## APPENDIX B

## FRACTURE TOUGHNESS TESTING

The objective of fracture toughness testing is to determine the plane strain fracture toughness, $K_{1c}$. This objective is attained by testing specimens of specific geometry to failure. Typical fracture toughness specimens are shown in Fig. B1. These specimens are usually cyclically loaded at low load prior to testing to insure a sharp crack. If a sharp crack is not present, the fracture toughness test measures initiation as well as crack propagation. This is an undesirable situation when resistance to fracture (fracture toughness) is to be measured.

In fracture toughness testing, it is necessary to measure the load applied to the specimen and the opening of the crack surfaces as illustrated for a typical geometry in the sketch in Fig. B2 (43). The plot of load versus crack surface displacement is called the load-displacement or P-v record. Typical P-v plots are illustrated in Fig. B3 (43). The idea behind this record is to enable the investigator to determine the load at which the crack has extended 2% of its original length and to operationally distinguish crack advance from plastic action (43).

In order to determine the crack advance load, a secant line is drawn on the record as shown in Fig. B3. This secant has a slope which is 5% less than the slope of the original linear portion of the record. The load at which the secant line crosses the P-v plot is called $P_5$. If higher load appears on the record prior to the $P_5$ load, this higher load is called $P_Q$. If a higher load is not reached prior to the $P_5$ load, then $P_5 = P_Q$. The maximum load appearing on the P-v record is $P_{max}$. If $P_{max}$ occurs prior to $P_5$ then $P_Q = P_{max}$. $P_Q$ is the load used to calculate a stress intensity labeled $K_Q$. $K_Q$ is called the "conditional $K_{1c}$." Whether or not $K_Q$ is a "valid $K_{1c}$" depends upon two criteria. First, $P_{max}/P_Q$ must be less than 1.10. Secondly, both the thickness and crack length of the specimen must be greater than $2.5\,(K_Q/\sigma_y)^2$.

If these criteria are met, then $K_Q = K_{Ic}$ (43). The purpose of this operational exercise with the P-v record is to insure that the specimen tested was of sufficient size to give a plane strain fracture toughness and not some other artificially higher toughness. The terminology "valid $K_{Ic}$" is used to indicate that plane strain conditions have indeed been met.

The preceding discussion of P-v record is according to an ASTM criteria published in 1972 (43). The previous (1969) criteria differs slightly from the later standard. The criteria for valid $K_{Ic}$ in 1969 was that the horizontal distance between the actual record and the secant corrected line at 80% of $P_5$ must be less than 25% of the corresponding distance at the $P_5$ load. This procedure is illustrated in Fig. B4. This procedure was replaced in 1972 by the $P_{max}/P_Q$ criteria. In this study the earlier 1969 criteria will be used throughout.
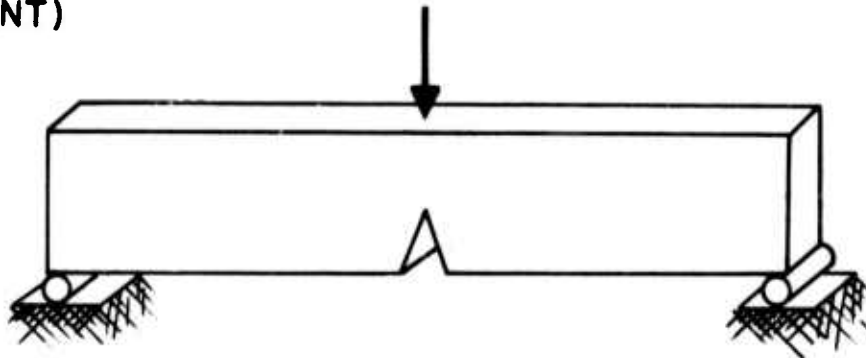
In general, if the requirements of the above secant correction procedure are not met and $K_Q$ is not equal to $K_{Ic}$, then the plastic action occurring at the tip of the crack involves a considerable volume and the equation and assumptions of linear elastic fracture mechanics are not applicable.
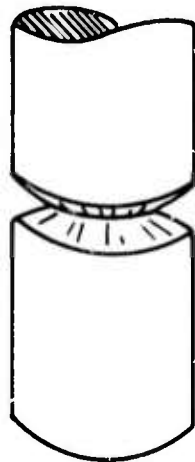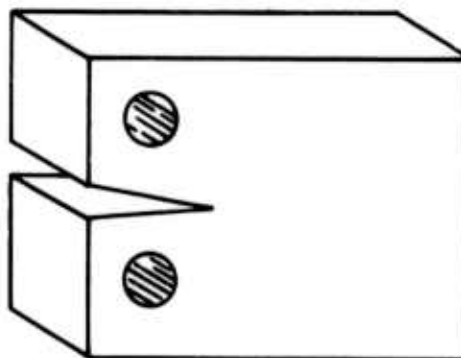
(A) CIRCUMFERENTIAL
NOTCH TENSION
(CNT)
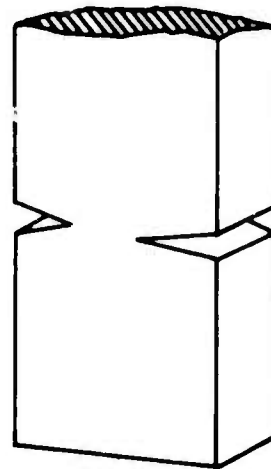
(B) DOUBLE EDGE CRACK
PLATE (DEC)

(C) THREE POINT BEND (3PB)

(D) COMPACT SPECIMEN (CT)

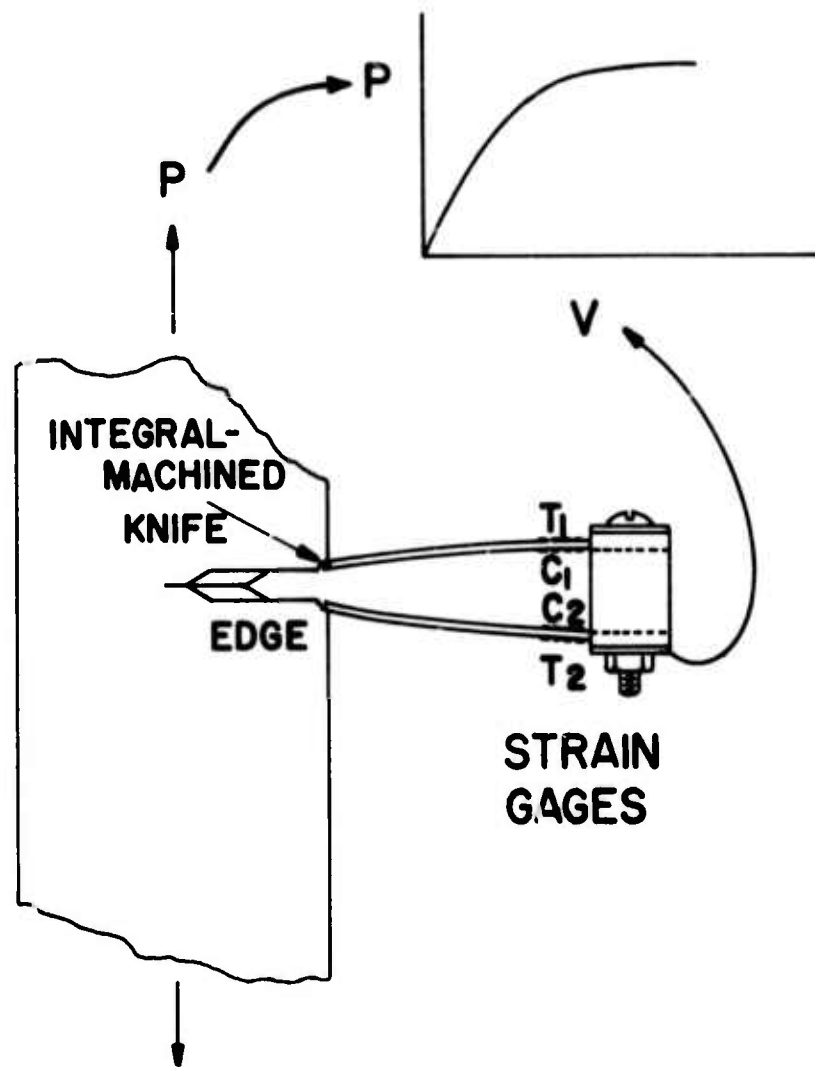Fig. B1    Typical Fracture Toughness Test Specimens

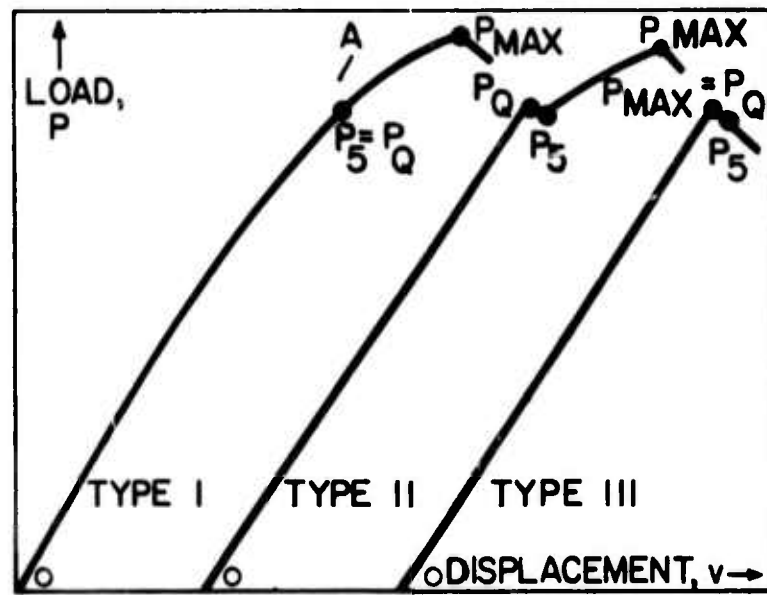Fig. B2   Typical Edge Crack Plate Specimen and Load-Displacement Record

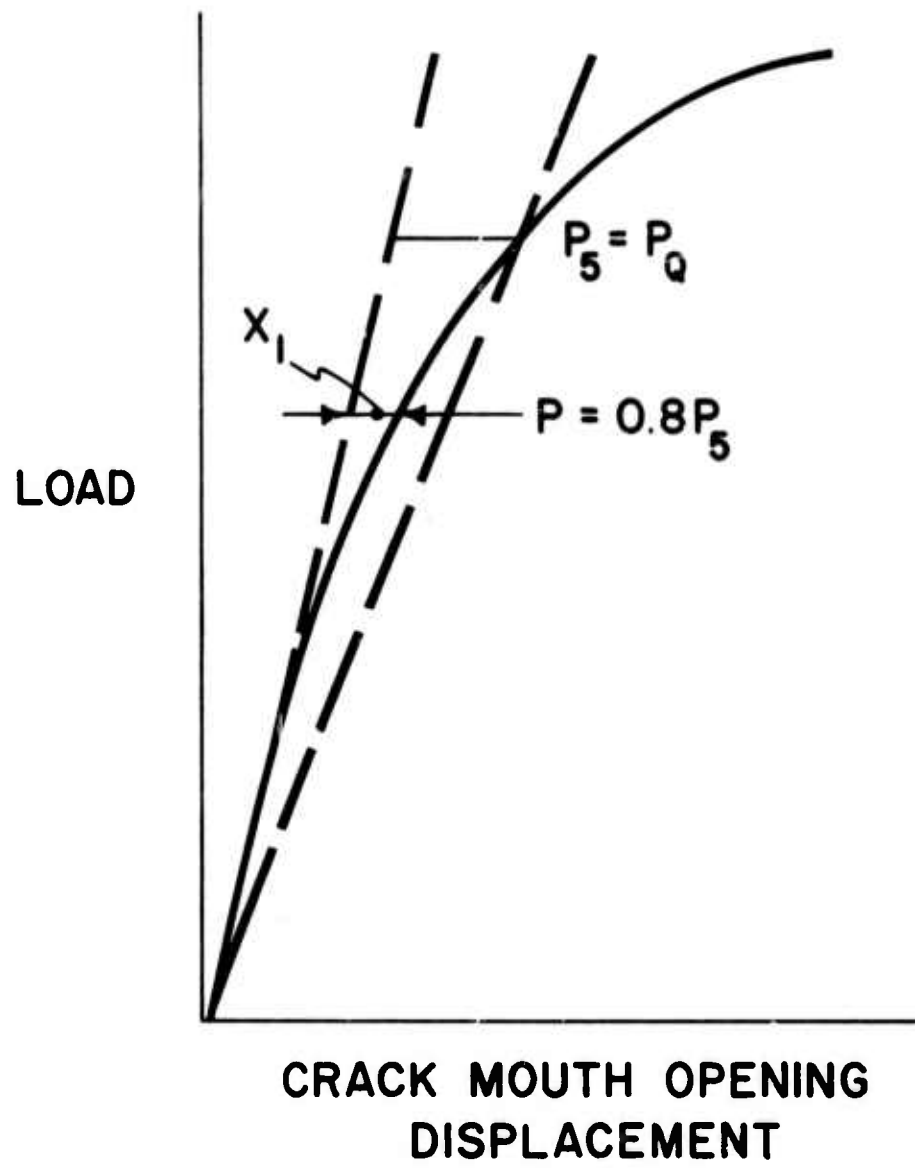Fig. B3    Typical P-v Records

**LOAD**

**CRACK MOUTH OPENING DISPLACEMENT**

Fig. B4   Validity Criteria for P-v Records Prior to 1972